Development of Seismic Isolation Systems Using Periodic Materials

Nuclear Energy Enabling Technologies

Dr. Yi-Lung Mo
University of Houston

In collaboration with:
University of Texas-Austin
Prairie View A&M University
Argonne National Laboratory

Alison Hahn, Federal POC
Ron Harwell, Technical POC

NEUP Nuclear Energy
University Programs

U.S. Department of Energy

DEVELOPMENT OF SEISMIC ISOLATION SYSTEMS USING

PERIODIC MATERIALS

TECHNICAL REPORT

Project No. 3219

By

Yiqun Yan and Y.L. Mo
University of Houston

Farn-Yuh Menq and Kenneth H. Stokoe, II
The University of Texas at Austin

Judy Perkins
Prairie View A & M University

Yu Tang
Argonne National Laboratory

Performed in cooperation with the Department of Energy

September 2014

Department of Civil and Environmental Engineering
University of Houston
Houston, Texas

DISCLAIMER

This research was performed in cooperation with the Department of Energy (DOE), the University of Texas at Austin, Prairie View A&M University, and Argonne National Laboratory. The contents of this report reflect the views of the authors, who are responsible for the facts and accuracy of the data presented herein. The contents do not necessarily reflect the official view or policies of the DOE. This report does not constitute a standard, specification, or regulation, nor is it intended for construction, bidding, or permit purposes. Trade names were used solely for information and not product endorsement.

ACKNOWLEDGEMENTS

ABSTRACT

Advanced fast nuclear power plants and small modular fast reactors are composed of thin-walled structures such as pipes; as a result, they do not have sufficient inherent strength to resist seismic loads. Seismic isolation, therefore, is an effective solution for mitigating earthquake hazards for these types of structures. Base isolation, on which numerous studies have been conducted, is a well-defined structure protection system against earthquakes. In conventional isolators, such as high-damping rubber bearings, lead-rubber bearings, and friction pendulum bearings, large relative displacements occur between upper structures and foundations. Only isolation in a horizontal direction is provided; these features are not desirable for the piping systems.

The concept of periodic materials, based on the theory of solid-state physics, can be applied to earthquake engineering. The periodic material is a material that possesses distinct characteristics that prevent waves with certain frequencies from being transmitted through it; therefore, this material can be used in structural foundations to block unwanted seismic waves with certain frequencies. The frequency band of periodic material that can filter out waves is called the band gap, and the structural foundation made of periodic material is referred to as the periodic foundation. The design of a nuclear power plant, therefore, can be unified around the desirable feature of a periodic foundation, while the continuous maintenance of the structure is not needed.

In this research project, three different types of periodic foundations were studied: one-dimensional, two-dimensional, and three-dimensional. The basic theories of periodic foundations are introduced first to find the band gaps; then the finite element methods are

used, to perform parametric analysis, and obtain attenuation zones; finally, experimental programs are conducted, and the test data are analyzed to verify the theory. This procedure shows that the periodic foundation is a promising and effective way to mitigate structural damage caused by earthquake excitation.

TABLE OF CONTENTS

LIST OF FIGURES

LIST OF TABLES

1 INTRODUCTION

1.1 Significance of Research

Advanced fast nuclear power plants (AFR) and some small modular fast reactors (SMFR) operate at high temperatures but at very low pressures, usually close to atmospheric pressure. These plants have components and piping that are thin-walled, and as a result, they do not have sufficient inherent strength to resist seismic loads. The use of seismic isolation is, therefore, an attractive and effective strategy for AFR and SMFR. Base isolation also enhances the design of a standard plant, which can lower plant costs and construction schedules.

Current fast nuclear reactor designs using seismic isolation generally employ high damping rubber bearings, lead-rubber bearings, or friction pendulum bearings (FPS bearings). In all these designs, large relative displacements between the building and the foundation occur, which accompany the reduction in seismic input (acceleration) to the superstructure. A gap (sometimes called a "moat") is usually provided between the isolated structure and the surrounding non-isolated structures to avoid the hammering of these structures. Any piping or other utility lines crossing this moat, therefore, must be designed to accommodate these large displacements, a costly feature, especially for large diameter piping. The development of a seismic isolation material and design, which has no, or minimum, relative displacement during earthquakes, is highly desirable. The necessity of a moat, however, requires careful attention to avoid any rigid connection between the isolated and non-isolated portions of the plant throughout its life; a design

that eliminates the need for such restrictive requirements would be very attractive. This project addresses this need.

The analytical and experimental studies performed in this project were conducted on a new, innovative seismic base isolator that mitigates potential seismic damages to advanced fast reactors. The innovative base isolator is made of a new material known as periodic material; its distinct feature is that it has material deficiency. This periodic material lacks a certain frequency band; as a result, it cannot transmit motions falling within that frequency band gap. This deficiency is the much-needed feature for the seismic base isolation system. With proper design, the frequency band gap can be adjusted to match the strong frequency range of the earthquake design. This material, then, can filter out the strong frequency motion that the AFR may be subjected to. Or, alternatively, the frequency band gap can be adjusted to match the fundamental frequency of the super structure so that the motion transmitted from the foundation does not contain this frequency. Pictures may best explain this concept. Fig. 1.1 and Fig. 1.2 show the characteristics of frequency band gaps in a theoretical periodic material.[1] The wave shown in Fig. 1.1 cannot propagate into the periodic material when the frequency of the wave falls within the range of the frequency band gap of the material. The wave shown in Fig. 1.2, however, can propagate into and through the periodic material since the frequency of the wave is outside the range of the frequency band gap of the material;

Fig. 1.1 Reflection of wave possessing a frequency falling within the frequency band gap of the periodic material[1]

Fig. 1.2 Wave propagation of wave possessing a frequency outside of the frequency band gap of the periodic material[1]

2

this periodic material-based method manipulates or blocks seismic wave energies in isolation system. In other words, the materials and isolation systems, properly designed and constructed, will possess frequency band gaps that will alter or block the energy input without the undesirable effects of more traditional base isolation systems such as residual displacements between the foundation and the supported structure.

The band gap phenomenon of periodic material has been known since 1900; the theory was established in 1920. The major applications for this material have been in solid-state physics. Recently, this material was proposed for seismic isolation used in civil structures; if this innovative idea is applied to civil structures, the impact on the economy and safety could be enormous.

1.2   Objective of Report

The goal of the proposed research is to develop a base isolation system that uses periodic materials to obstruct completely or change the pattern of earthquake event energy before it reaches the foundation of structural systems in nuclear power plants. This goal reached would result in total isolation of the foundation from earthquake wave energy, because no energy would be passing through it. Total isolation would be of special significance to structures in nuclear power plants.

This project implemented an experimental program to verify and refine the analytical study results and the basic design parameters. The project also generated information needed to quantify the behavior of various periodic materials and material combinations when they are used in standard nuclear containment configurations and practices. The one-dimensional (1D) layered periodic foundation shake table test was conducted; two-dimensional (2D) and three-dimensional (3D) periodic foundations were

3

tested in the free field by using the truck-mounted dynamic load generators. The test results were used to verify and refine the design theory and procedures of periodic material-based seismic isolation systems.

1.3   Scope of the Research

This proposal is divided into eight chapters. The logical path of the project is shown in Fig. 1.3.
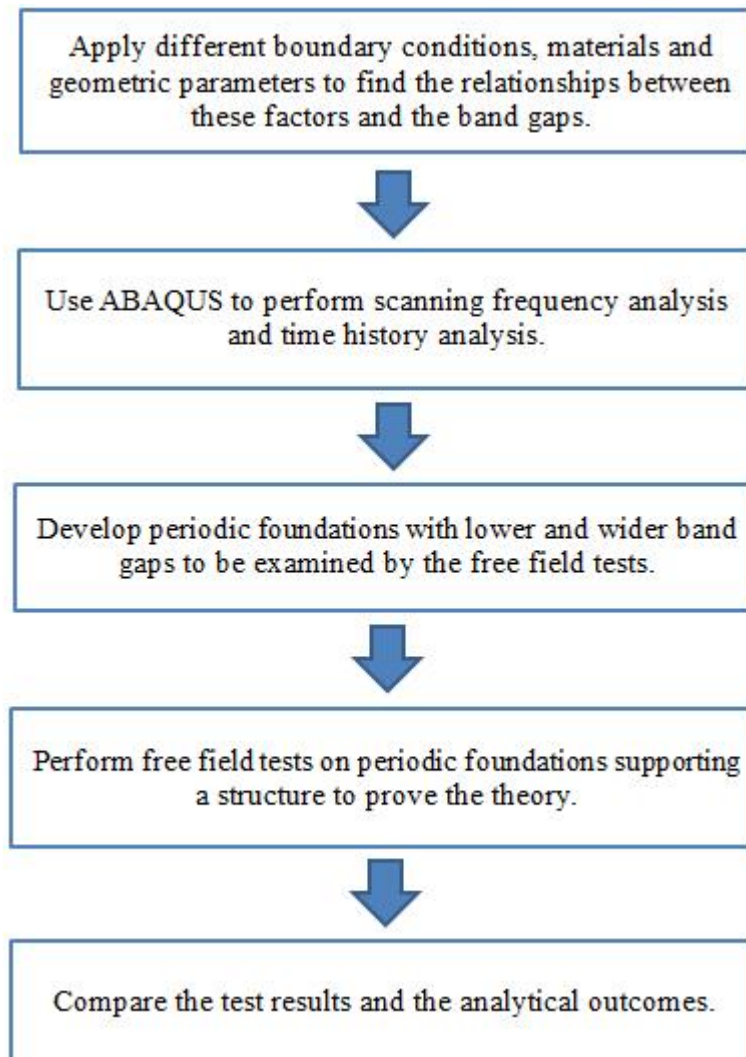
Fig. 1.3 Logic path of the research

Chapter 1 shows significance and objective of the research and presents the outline of the report.

Chapter 2 describes a literature study of the past relevant work in the base isolation system. Then, the background of phononic crystals is introduced since the basic idea of periodic foundations is delivered from the concept of phononic crystals. Finally, recent studies of periodic structures are introduced.

Chapter 3 presents the basic theory of periodic foundations. Next, theoretical solutions of frequency band gaps are obtained for the 1D, 2D, and 3D periodic foundations.

Chapter 4 discusses the attenuation zones of the periodic foundations given by using the finite element method (FEM). The parametric studies are conducted first for 1D, 2D, and 3D periodic foundations. Then, scanning frequency analysis is performed with both shear wave (S wave) and primary wave (P wave) excitations to obtain attenuation zones for 1D, 2D, and 3D periodic foundations.

Chapter 5 describes experimental programs according to the FEM results (in Chapter 4), specimens of periodic foundations are designed, and the test setup is described.

Chapter 6 presents the test results under different dynamic loads, i.e., stepped sine waves, fixed sine waves, and seismic waves for both S and P waves.

Chapter 7 shows the comparison of test results for 1D, 2D, and 3D periodic foundations and the finite element analysis (FEA) outcomes in both time domain and frequency domain.

Chapter 8 presents conclusions and suggests further studies in this area.

2   LITERATURE REVIEW

2.1   Overview of Base Isolation Systems

The design of buildings and other structures capable of withstanding earthquake events has been the focus of research by engineers for many decades. A commonly accepted method for the design of seismic-resistant buildings and structures, however, has not yet been developed. Traditional design methods based simply on static structural strength with impact factors to account for dynamic loads, fortunately, have been reviewed and gradually replaced by novel methodologies over the last three decades. Evolving concepts of structural element ductility and the importance of shear resistance have contributed to the effective design of structural elements and systems resistant to dynamic loadings from earthquakes. Passive and active systems have been proposed and implemented to augment the ability of the structure to resist an earthquake event.

2.1.1   The passive base isolation system

Recent designs of seismic isolation technologies have been proposed as ways to resist seismic loadings. One strategy implemented to date has been the addition of elastomeric bearings between the base of the structure and ground.[2] Fig. 2.1 shows testing of elastomeric bearings at University at Buffalo, The State University of New York.[3] This system attempts to modify the fundamental frequency of the structure, thereby decreasing its acceleration response. The strategy of adding an isolation system between the base of the structure and ground will typically result in a structure with much lower fundamental frequency than the original fundamental frequency of the non-isolated (fixed-base) structure.[4]-[7] A change in the fundamental frequency of a structure may

reduce the acceleration response significantly, according to the acceleration design spectrum, thereby enhancing the overall ability of the structure to withstand and survive the earthquake event.
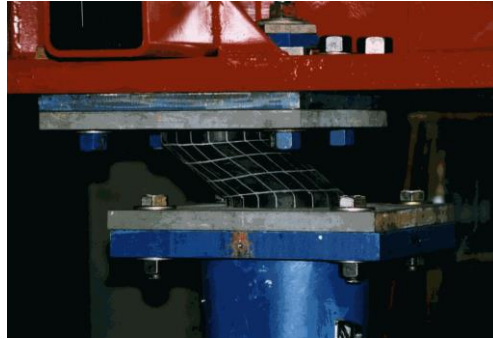
Fig. 2.1 Testing elastomeric bearings[3]

The first building with a base isolation system in United States, was the Foothill Communities Law and Justice Center located in Los Angeles, completed in 1985. The isolation system of the four-story building has 98 isolators of multilayered natural rubber bearings reinforced with steel plates.[8] There were over 450 buildings that used rubber bearings for seismic protection purposes in China until 2004, including houses, offices, schools, museums, libraries, and hospital buildings with 3-19 stories.[9] The successful experience of using elastomeric bearings shows the advantages of this system: effectiveness, stability, insensitive to foundation settlement, and the rubber bearings can decrease the temperature stress in structures by free horizontal deformation of bearings during pronounced change of temperature around the structure.[9]

Another type of passive isolation system is typified by the sliding system. This system works by limiting the transfer of shear across the isolation interface.[8] The pure friction base isolation system is very simple and requires an easy manufacturing process; therefore, it is highly suitable for low-cost structures.[10] The friction-pendulum system is

a sliding system using a special interfacial material sliding on stainless steel and has been used for several projects in the United States, both in new and retrofitted constructions.[8] Recently, more advanced techniques and materials have been added to sliding isolation systems, including the Electricite De France (EDF) system, the Resilient Friction Base Isolator (RFBI) system, the Sliding Resilient Friction (SRF), which combines the desirable feature of EDF and RFBI system, TAISEI Shake Suppression (TASS) system, the Friction Pendulum system (FPS), and the elliptical rolling rods.[11]

The Electricite De France (EDF) system is a friction-type base isolator consisting of a laminated (steel-reinforced) neoprene pad topped by a lead-bronze plate, which is in frictional contact with a steel plate anchored to the structure.[12] The EDF system has been used in a nuclear power plant at Koeberg in South Africa.

Mostaghel and Khodaverdian proposed the Resilient Friction Base Isolator (RFBI) system in 1987. The RFBI system consists of a set of flat rings, which can slide on each other and have a central rubber core and/or peripheral rubber cores. The RFBI (isolator) combines friction damping and the resiliency of rubber.[13]

Su et al., presented a Sliding Resilient Friction (SRF) system in 1991.[14] The SRF system combines the advantages of EDF and RFBI base isolators. Absent large displacements, using an SRF system can reduce a structure's peak accelerations and deflections; the system also provides additional safety against unexpected severe ground motions.

The TAISEI Shake Suppression (TASS) system is composed of two types of bearings, such as rubber bearings and sliding bearings.[15] The TASS system was developed for high-rise buildings.[16] It was proved experimentally with high-strength

materials; and a long-span structure system would provide seismic isolation for high-rise buildings undergoing strong ground motions.

A friction pendulum system (FPS) is based on the principles of pendulum motion. The friction damping absorbs the energy of the structure supported by FPS.[17] Fig. 2.2 shows the friction pendulum-bearing used in the Benicia-Martinez Bridge Retrofit.[18]

Fig. 2.2 Friction pendulum bearing used in Benicia-Martinez Bridge[18]

The elliptical rolling rods overcome the disadvantages of circular rolling rods, i.e., large peak and residual base displacements. Elliptical rolling rods were effective in reducing the seismic response of the system without undergoing large base displacements.[19] The roller bearings require maintenance throughout their working life, however, and the system can isolate the ground motion in only one direction.

One significant drawback of a traditional seismic isolation system is that it will usually have residual (permanent) horizontal displacements after earthquake events. The bearings are very stiff in the vertical direction and are very flexible in the horizontal direction. The action of the bearings under seismic loading is to isolate the building from horizontal components of earthquake ground movement, while vertical components of earthquake ground movement are transmitted through to the structure relatively unchanged.

2.1.2 The active base isolation system

Active base isolation, which is composed of a passive isolation system combined with control actuators, has been proposed as an alternative to overcome the disadvantages of passive base isolation systems. In active isolation systems, the control actuators are used to reduce drifts and floor accelerations. Many small-scale experiments of active base isolation systems have been performed and the effectiveness of such systems proved.

Nagarajaiah et al.,[20] presented an experimental and analytical study of hybrid control of bridges using sliding bearings, with re-centering springs and servo-hydraulic actuators; this study produced the control algorithm based on instantaneous optimal control laws. The study showed that, with hybrid control, accelerations were reduced substantially, while sliding displacement was confined within an acceptable range; post earthquake permanent offsets were eliminated almost completely.

Schmitendorf et al.,[21] presented an effective control technique for application to seismic-excited building structures. The control method was robust with respect to parameter uncertainty on the model, and it could easily incorporate actuator dynamics, thus eliminating the adverse effects resulting from the slow response of the actuator.

Yang et al.,[22] proposed robust control methods for seismic excited buildings isolated by a frictional-type sliding-isolation system. A three-story quarter-scale nonlinear building model was tested to verify the control methods. The building model was mounted on a base-mate supported by four frictional bearings. Experimental test results indicated that the control performance was remarkable, although a slight degradation was observed owing to noise pollution and system time delays.

Chang and Spencer[23] tested an active base isolation system with unique features including low-friction pendular bearings and custom-manufactured low-force hydraulic actuators. The control-structure interaction was also considered in these control strategies, and the strategies were proved to perform effectively for a wide range of seismic excitation.

As reported by Mehrparvar and Khoshnoudian,[24] several advantages of active control systems over passive devices can be cited, such as enhanced effectiveness in response control, relative insensitivity to site conditions and ground motions, applicability to multi-hazard mitigation situations, and selectivity of control objectives. The active control system nevertheless requires a large external power supply for structural systems during seismic events, which along with reliability and other issues, make them unsuitable for broad application in civil engineering. In contrast, semi-active control systems possess most of the advantages of active control systems without requiring large energy sources; however, the semi-active control systems lack reliability.[25] Complex details and high costs, moreover, put a drag on their practical application.

2.2   Overview of Phononic Crystals

The concept of phononic crystals is analogous to photonic crystals. Photonic crystals are composed of periodic dielectric, metallo-dielectric, or even superconductor microstructures or nanostructures that affect the propagation of electromagnetic waves (EM); specific frequency ranges of EM are unable to pass through the photonic crystal; these frequency ranges are called band gaps.

The band gap phenomenon also exists in phononic crystals. Investigations in the field of solid-state physics have shown that certain crystal arrangements may be used to manipulate the energy or patterns of acoustic (mechanical) wave energy.[26]-[30] These materials, termed phononic crystals, can be designed to produce specific gaps in the frequency response of the structure. When the frequency contents of a wave fall within the range of the frequency band gap of a periodic structure, the wave, and its energy, cannot propagate through the periodic structure.[31]

According to the dimensions of the periodic structures, there are three types of phononic crystal, i.e. one-dimensional (1D), two-dimensional (2D), and three-dimensional (3D) phononic crystals, as shown in Fig. 2.3.[29] Different colors in the figure represent different elastic materials arranged periodically. Depending on the materials used in the phononic crystals, they can be classified as solid-solid, solid-air (air-solid), or solid-liquid (liquid-solid) composites for 2D and 3D phononic crystals; solid-liquid phononic crystal means the solid scatters arrange periodically in a liquid matrix.
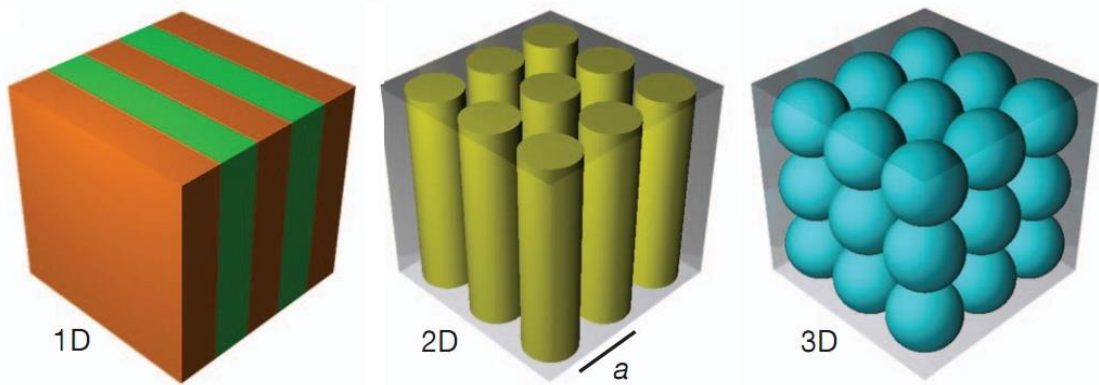
Fig. 2.3 1D, 2D and 3D phononic crystals[29]

2.2.1　History of phononic crystals

In 1992 for the first time, Sigalas and Economou[32] proved theoretically the existence of frequency band gaps of elastic and acoustic waves in periodic structures consisting of identical spheres placed periodically within a homogeneous host material. In 1993, Kushwaha et al.,[33] obtained the band gaps of 2D phononic crystal using the plane wave expansion method. They also pointed out that one can design the phononic crystal to provide a vibrationless environment for high-precision mechanical systems in a given frequency range.[34] Eusebio Sempere's kinematic sculpture as shown in Fig. 2.4, is made of a periodic array of hollow stainless-steel cylinders of 2.9cm diameter, arranged on a square 10×10cm lattice.[35] In 1995, researchers at the Materials Science Institute of Madrid showed that the sculpture strongly attenuated sound waves at certain frequencies, thus providing the first experimental evidence for the existence of phononic band gaps in periodic structures. In 2000, Liu and Zhang et al.,[27] proposed the idea of localized resonant structures, 3D periodic materials with lower frequency band gaps. The size of the lattice constant is two orders of magnitude smaller than the wavelength of the band gaps. The literature before 2000 showed that the wavelength of the band gaps had the same size as the lattice constant due to Bragg scattering. The theory of localized resonant structures may lead to applications in seismic wave reflection, since the frequency band gaps can be reduced to very low ranges.

Fig. 2.4 Sculpture by Eusebio Sempere[35]

The band gaps of localized resonant structures are determined by the material and geometric properties of phononic crystals. Liu et al.,[36] found that the frequency band gap was affected by elastic properties of the coating material. The elastic wave band-gap properties of three-component composites were studied using multiple-scattering theory. The composites consisted of a periodic arrangement of coated spheres inside an embedding medium. The elastic wave band-gap properties could be tuned continuously from a resonance gap to a Bragg gap just by varying the elastic properties of the coating material. The study of 2D phononic crystals by Zhang et al.,[37] consisted of coating cylinders embedded in a glass host using the plane wave expansion method. The study showed that the optimum gap was obtained by tuning the thickness ratio of the coating layer for the three-component 2D phononic crystals.

Liu et al.,[38] provided a simple analytic model for sonic band gaps owing to resonance. In their paper, they described the origin of band gaps in the local resonant phenomenon.

Goffaux et al.,[39]-[41] studied elastic wave propagation in a locally resonant sonic material. They introduced a simple mechanical model to show a physical insight of the local resonance phenomenon. The researchers[41] made a comparison of the Bragg gap and resonance gap; the Bragg gap had even better attenuation performances on a larger range of frequencies owing to Bragg interference phenomena at low frequencies.

Ho et al.,[42] demonstrated a broadband sound shield based on layers of locally resonant sonic materials. A broadband (200–500 Hz) sound barrier was achieved, and it was significantly better than that dictated by mass density law.

Zhang and Cheng[43][44] had already made a comparison of the band gaps between the binary and three-component composite 2D phononic crystal, theoretically and experimentally. Both results proved the existence of a much broader gap of the three-component crystal slab over the binary.

Hirsekorn et al.,[45][46] performed numerical simulations of acoustic wave propagation through sonic crystals consisting of local resonators using the Local Interaction Simulation Approach (LISA). Three strong attenuation bands were found at frequencies between 0.3 and 6.0 kHz, which do not depend on the periodicity of the crystal.

Wang et al.,[47][48] studied the propagation of elastic waves in 2D binary phononic crystals consisting of soft rubber cylinders in epoxy. The binary locally resonant

materials were studied using the lumped-mass method. The first and second in-plane locally resonant modes were localized in both the coating layer and the core.

Hsu and Wu[49] studied the 2D two-component phononic crystal plated with a finite thickness using the plane wave expansion method. The low-frequency gaps of Lamb waves owing to localized resonance mechanism and flexure-dominated plate modes were significantly dependent, not only on the filling ratios, but also on the plate thickness.

Oudich et al.,[50]-[52] presented a 2D locally resonant phononic crystal made of stubbed plate; the width of this locally resonant band gap was greatly dependent on the height and area of the cross-section of the stubs.[50] The authors[51] present locally resonant phononic crystal that served as straight and bent waveguides for elastic waves by using the finite element method combined with the super-cell technique. Fig. 2.5 shows bent wave-guide.[51] The existence of a locally resonant sonic band gap in a 2D stubbed plate was proved experimentally.[52]
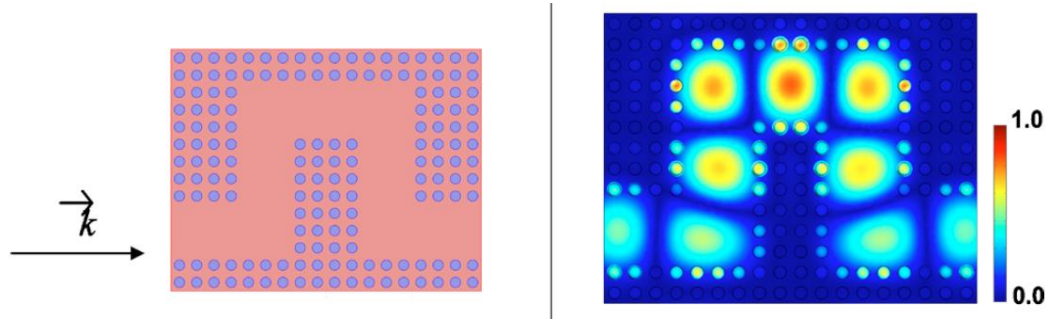
Fig. 2.5 Bent wave-guide and absolute value of the displacement field for the guiding mode[51]

To date, the existence of locally resonant frequency band gaps of phononic crystals has been proved both theoretically and experimentally.

2.2.2 Computing methods of phononic crystals

There are several ways to obtain frequency band gaps of phononic crystals. Five of them are commonly used: (1) the transfer matrix method, (2) the plane wave expansion method, (3) the finite different time domain method, (4) the multiple scattering theory, and (5) the finite element method.

The transfer matrix (TM) method[53]-[57] needs only a small amount of computation, and it is used in 1D phononic crystals, i.e., phononic crystal Euler beams and phononic crystal bars. Using the motion equations of the beams or bars, along with the continuous conditions at the interface, i.e., the displacement, rotation angle, bending moment, and shear force, the transfer matrix of the TM method can be obtained. One can obtain an Eigen value problem with the transfer matrix and periodic boundary conditions, which contain the dispersion relation of phononic crystals. The main advantage of the TM method is that only a small amount of computation is needed. The TM method cannot be used, however, to solve the band structures of 2D and 3D phononic crystals.

The plane wave expansion (PWE) method[32]-[34][39][58]-[61] is one of the most popular ways to obtain the band gaps of phononic crystals. Until now, the method has been used to solve the band gaps of phononic crystals with solid-solid, solid-air (air-solid), solid-liquid (liquid-solid) composites. Owing to the periodic boundary conditions of phononic crystals, the densities and elastic constants of the materials can be written as Fourier series expansions. Taken with the Bloch's theorem, the equations of motion can be written in the form of Eigen value equations, and the problem is converted to an Eigen value problem. The PWE method encounters convergence problems when the phononic crystal has a large elastic difference. The method becomes both time-consuming and difficult in memory requirements with the increasing of the plane waves.

18

The finite difference time domain (FDTD) method[62]-[65] is suitable for dealing with different geometric structures and for handling the numerical convergence problem. The wave equations are discretized in the time domain first, and the periodic boundary conditions and the Bloch's theorem are applied next. With a given excitation, the response of phononic crystals in the time domain can be obtained. After the Fourier Transform is applied, the Eigen values from the frequency spectrum can be obtained, and the band gaps of the phononic crystals solved. The FDTD method requires considerable calculation; therefore, parallel computing technology and high efficiency computers are needed.

Multiple scattering theory (MST)[66]-[69] can be used for 2D and 3D phononic crystals; MST is an exact theory without approximation; however, it is suitable only for highly symmetric scatters of 2D and 3D phononic crystals.

The finite element (FE) method is a numerical technique for finding approximate solutions to boundary value problems for differential equations. To obtain the band gaps of phononic crystals, the periodic boundary conditions are applied to the unit cells. Commercial software such as ABAQUS and ANSYS cannot be used to apply the periodic boundary conditions to the phononic crystals directly. COMSOL Multiphysics, however, provides periodic boundary conditions that can be used very easily.

2.2.3 Application of phononic crystals

Kushwaha[34] proposed for the first time in 1993 the idea that phononic crystals can be used for vibrationless environments. Maldovan[29] summarized the frequency ranges in which phononic crystals would work and their possible applications, as shown in Fig. 2.6. Sound waves oscillate at low frequencies (kilohertz) and propagate over large

19

distances, and most heat vibrations oscillate at high frequencies (terahertz) and travel over small distances. Phononic crystals can be used to insulate buildings thermally, reduce environmental noise, transform waste heat into electricity, and develop earthquake protection.
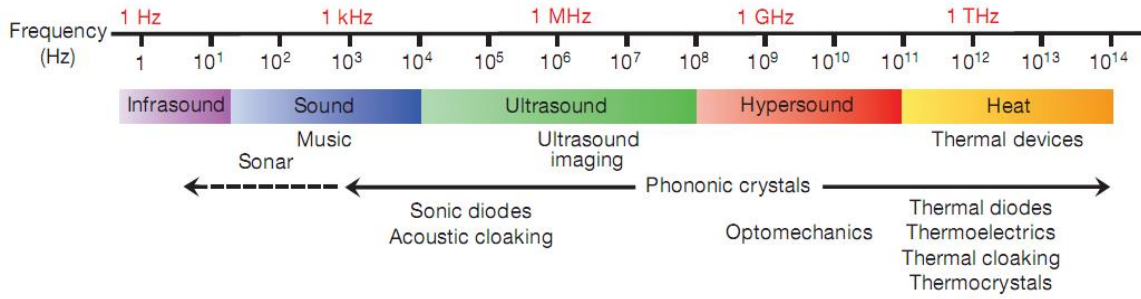
Fig. 2.6 Phononic spectrum[29]

Pennec et al.,[70] summarized the applications of 2D phononic crystals and found that frequency filters and efficient devices for wavelength de-multiplexing could be achieved owing to defect modes of phononic crystals (cavities, waveguides, stubs, etc.). The existence of guided modes in the band structure of the 2D plate of phononic crystals was proved; therefore, surface acoustic waves propagating in 2D phononic crystals should open new perspectives in high-frequency, radio-frequency devices. The locally resonant phononic crystals made possible sonic insulators that are relatively small thickness, with frequencies on the order of kHz.

In summary, although there are no commercial products based on phononic crystals, both theoretical and experimental studies indicate a promising future for phononic crystals.

2.3   Overview of Periodic Structures

Guided by recent advances in solid-state research and the concept of frequency band gaps in periodic materials such as phononic crystals, this new periodic material is used in seismic base isolation as an innovative means to mitigate potential damage to structures. With this periodic material, the pattern of the earthquake event energy will be completely obstructed or changed when it reaches the periodic foundation of the structural system; this will result in a total isolation of the foundation from the earthquake wave energy because no energy will pass through it. The upper structure, therefore, can be protected during an earthquake along with non-structural components. This total isolation will be of special significance to some specific structures housing highly vibration-sensitive equipment such as research laboratories, medical facilities with sensitive imaging equipment, or high-precision facilities specializing in the fabrication of electronic components. Further, the full isolation of emergency-critical structures such as bridges, hospitals housing emergency response units or equipment, and power generation or distribution structures will have a better earthquake emergency response; consequently, there will be fewer compromises to the entire emergency response system. Periodic foundations are arranged in a periodic way in one, two, and three directions, which are defined in Fig. 2.7 as one-dimensional periodic foundation (1D), two-dimensional periodic foundation (2D), and three-dimensional periodic foundation (3D), respectively. The frequency band gaps of the periodic foundations are also called attenuation zones. Many studies have been conducted to investigate the 1D layered periodic structures both theoretically and experimentally.
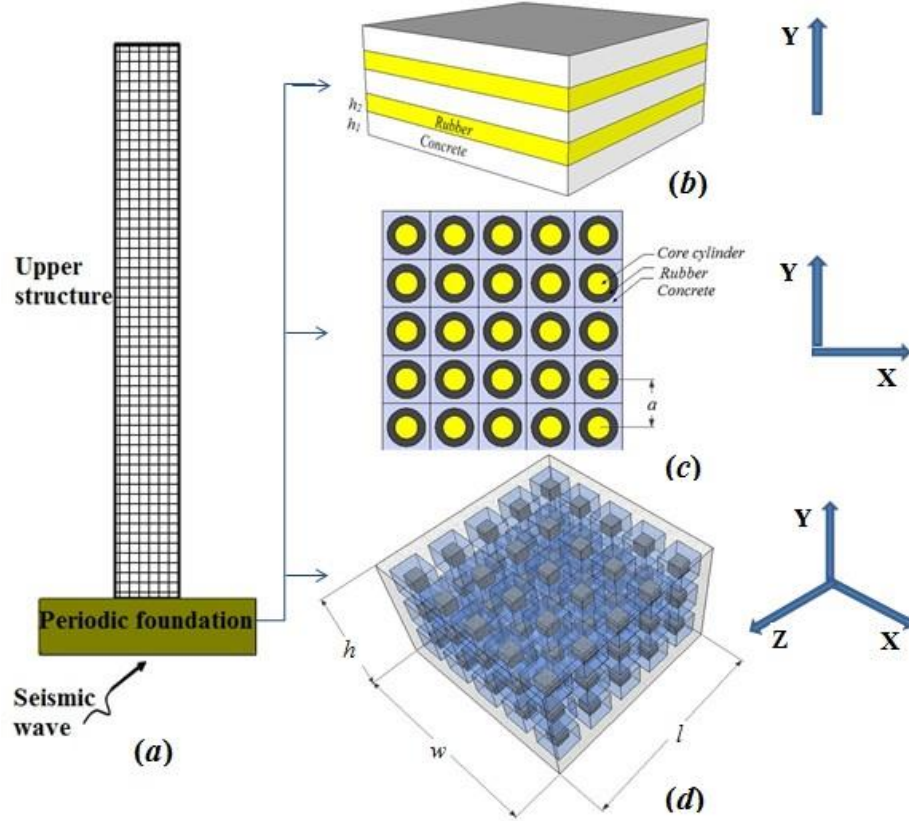
Fig. 2.7 (a) Periodic foundation with upper structure; (b) 1D periodic foundation; (c) 2D periodic foundation; (d) 3D periodic foundation.

Numerical studies on flexural vibration periodic beams were conducted by many researchers.[71]-[75] The existence of vibration gaps was found through comprehensive studies. Wen et al.,[71] studied, theoretically and experimentally in 2005, a periodic binary straight beam with different cross-sections. The existence of flexural wave band gaps in the periodic beam was proved, and a vibration isolation structure was designed. Hussein et al.,[72] proposed in 2007 a novel design paradigm called multi-scale dispersive design (MDD). According to the MDD method, periodic unit cells could be designed for desired frequency band properties, and with appropriate scaling, these cells could be used as building blocks for forming fully periodic or partially periodic structures with related dynamic characteristics. Using the differential quadrature method[73][74], flexural vibration

band gaps in periodic beams were studied, considering the influences of shear deformation, geometrical parameters, and material parameters. Attenuation in band gaps delivered a new idea in structural design to weaken vibration. The critical frequency was found, owing to the Pasternak foundation, and a comprehensive parameter study was conducted to highlight the influence of the foundation modulus on the band gaps. Yu et al., [75] found that, by analyzing the beam on elastic foundations using the transfer matrix method, a gap with low frequency and wide range could exist in a beam on elastic foundations.

The 1D periodic structure was used as the legs of an offshore platform, as shown in Fig. 2.8.[76][77] The periodic legs were discussed theoretically using the transfer matrix method and validated experimentally using a scaled experimental model of an offshore platform. Periodic legs were found to isolate the vibration transmitted from sea waves to offshore platform structures in the axial and lateral directions over a broad frequency band.

Fig. 2.8 Oil and gas offshore platform

The 1D periodic structures were used as foundations and to isolate upper structures.[78]-[80] The 1D layered periodic foundation is discussed theoretically.[78] Studies

23

of dynamic responses of a seven-story frame structure with three different foundations were conducted and compared to test the validity of the periodic isolated foundation. A 1D periodic structure, it was found, was an effective method to block seismic waves for structures in civil engineering. Shi et al.,[79] proposed a new type of a seismic isolation foundation configuration containing several concrete layers and rubber blocks. The equivalent analytical model for the periodic foundation and two formulas were established. The first attenuation zone of the new configuration of a seismic isolation foundation was as low 2.15 Hz to 15.01 Hz for seismic protection. Cheng and Shi[80] proposed a multi-mass-spring model to study the band of frequency gaps of 1D periodic structures, and they investigated the dynamic properties of finite periodic structures from an energy viewpoint.

The existence of frequency band gaps of a 2D periodic structure has been studied theoretically and experimentally. [81]-[86] Two-dimensional periodic foundations have been studied theoretically[81]-[84]; the 2D periodic foundation with a low frequency gap was achieved. Simulations demonstrated that periodic foundations could greatly reduce the dynamic response of upper structures under both vertical and longitudinal ground motions. Two-dimensional periodic structures were used as pile barriers owing to the frequency band gap effect of the periodic structure.[85] The periodic pile barrier significantly reduced the vibration in the frequency band gaps. A large-scale experiment, as shown in Fig. 2.9, was performed.[86] The test showed that a structured soil consisting of clay with 5-m deep boreholes shielded surface elastic waves of around 50 Hz. Then, numerical simulations were conducted to simulate the energy field, and they were

24

compared to the test results. The paper showed that periodic structures were promising in civil engineering applications.
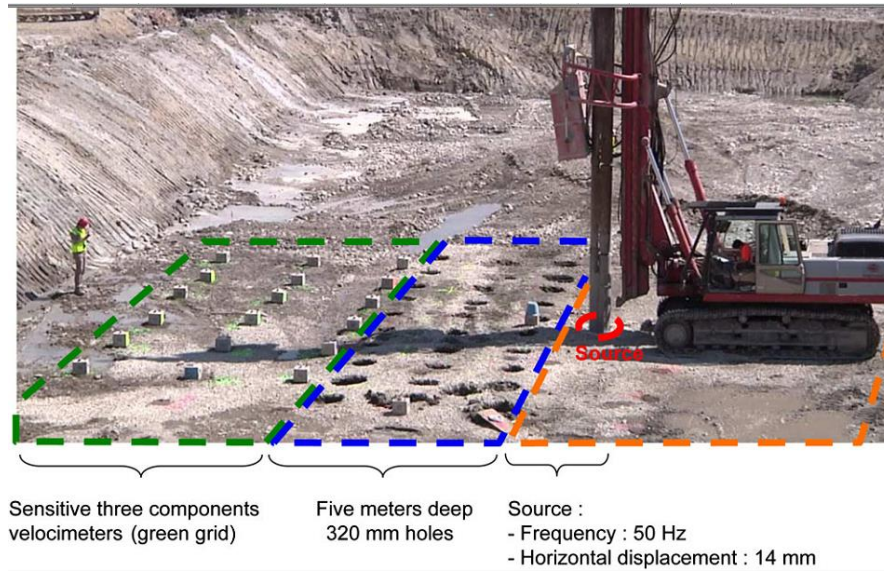
Fig. 2.9 Large scale experiment of 2D periodic structure to shield surface elastic waves[86]

Shi and Huang[87] presented a 3D seimic isolation system using periodic materials with three components, i.e., a high-density core, a soft coating, and a concrete matrix. They used the finite element method to perform the parametric study, including physical and geometric parameters of the typical cell. The periodic foundation was found to greatly reduce the seismic response, which implies that the periodic foundation had great potential application to seismic isolation. Until now, however, very few literary sources have reported on 2D and 3D periodic foundations relative to the experimental study in civil engineering research.

3   THE BASIC THEORIES OF PERIODIC FOUNDATIONS

The basic theories of periodic structures composed of infinite unit cells are illustrated in this chapter. The transfer matrix method, plane wave expansion method, and finite difference time domain method for 1D, 2D, and 3D periodic foundations are introduced in detail; the frequency band gaps of periodic foundations with infinite unit cells are calculated.

3.1   Basic Theories of 1D Layered Periodic Foundations

The transfer matrix method of 1D periodic foundation band gaps was used to solve the wave equations. Xiang et al.,[88] illustrated a method to solve the 1D layered periodic foundation. Fig. 3.1a. shows the 1D layered periodic material composed of two materials, A and B; Fig. 3.1b. shows one unit cell of the 1D layered periodic foundation. Each layer is extended infinitely in the XY plan, and the unit cells are repeated in the Z direction infinitely for the coordinate system specified. The thickness of layer A and layer B of a unit cell is h_1 and h_2, respectively. The periodicity of the foundation structure and displacement makes it possible to investigate the frequency band gap by studying one unit cell.
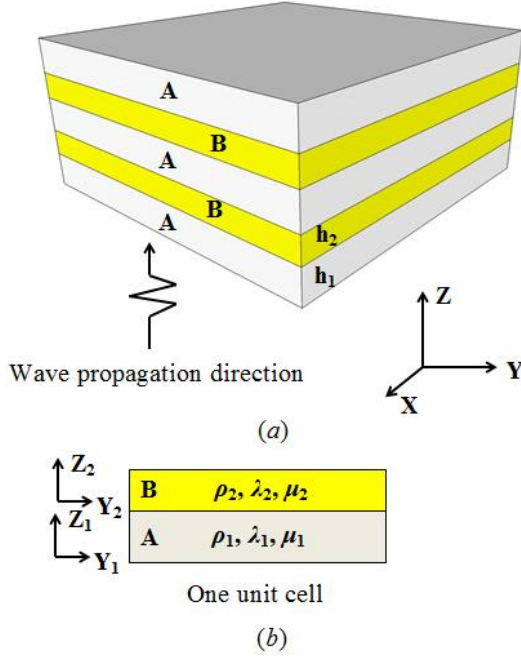
Fig. 3.1 Configuration of a layered periodic foundation and its unit cell
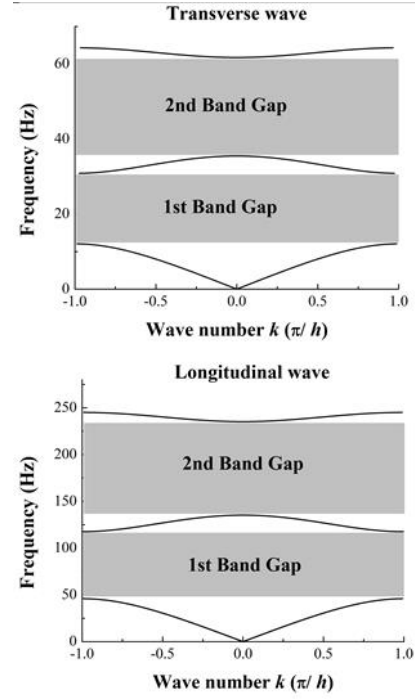
Fig. 3.2 Dispersion curves of 1D periodic foundation

Let v, w represent displacements in the Y and Z directions, respectively. Consider an elastic wave with propagation along Z. The equation of motion in each layer is:

$$\frac{\partial^2 u_i}{\partial t^2} = C_i^2 \frac{\partial^2 u_i}{\partial z_i^2}$$

(3-1)

Where $u = w$ and $C = C_p = \sqrt{(\lambda + 2\mu)/\rho}$ for the longitudinal wave (P wave), or $u = v$ and $C = C_t = \sqrt{\mu/\rho}$ for the transverse wave (S wave). λ and μ are Lamé's elastic constant, ρ is the density of material. The index $i = 1, 2$ indicates layers A and B, respectively. The solution to Eq. (3-1)for the free vibration analysis is given by Eq. (3-2)

$$u_i(z_i, t) = e^{i\omega t} u_i(z_i)$$

(3-2)

Where k is the wave number and ω the angular frequency, the case of transverse waves is taken as an example. Substituting Eq. (3-2) into Eq. (3-1) yields:

$$C_{ti}^2 \frac{\partial^2 u_i(z_i)}{\partial z_i^2} + \omega^2 u_i(z_i) = 0 \tag{3-3}$$

The general solution of this equation is found as follows:

$$u_i(z_i) = A_i \sin\left(\omega z_i / C_{ti}\right) + B_i \cos\left(\omega z_i / C_{ti}\right) \tag{3-4}$$

The shear stress can be expressed as:

$$\tau_i(z_i) = \mu_i \partial u_i / \partial z_i = \mu_i \omega \left[A_i \cos\left(\omega z_i / C_{ti}\right) - B_i \sin\left(\omega z_i / C_{ti}\right) \right] / C_{ti} \tag{3-5}$$

There are four unknown constants A_1, A_2, B_1 and B_2, which are determined by boundary and continuity conditions.

The displacement and stress at the interface of materials A and B satisfy continuity conditions:

$$u_1(h_1) = u_2(0), \; \tau_1(h_1) = \tau_2(0) \tag{3-6}$$

According to the Bloch's theorem,[34] displacement and stress satisfy the periodic boundary conditions

$$u_1(0)e^{ik \cdot h} = u_2(h_2), \; \tau_1(0)e^{ik \cdot h} = \tau_2(h_2) \tag{3-7}$$

Substituting Eqs. (3-4) and (3-5) into Eqs. (3-6) and (3-7), yields:

$$\begin{bmatrix} \sin\left(\omega h_1 / C_{t1}\right) & \cos\left(\omega h_1 / C_{t1}\right) & 0 & -1 \\ \mu_1 C_{t2} \cos\left(\omega h_1 / C_{t1}\right) & -\mu_1 C_{t2} \sin\left(\omega h_1 / C_{t1}\right) & -\mu_2 C_{t1} & 0 \\ 0 & e^{ik \cdot h} & -\sin\left(\omega h_2 / C_{t2}\right) & -\cos\left(\omega h_2 / C_{t2}\right) \\ \mu_1 C_{t2} \cdot e^{ik \cdot h} & 0 & -\mu_2 C_{t1} \cos\left(\omega h_2 / C_{t2}\right) & \mu_2 C_{t1} \sin\left(\omega h_2 / C_{t2}\right) \end{bmatrix} \begin{bmatrix} A_1 \\ B_1 \\ A_2 \\ B_2 \end{bmatrix} = 0 \tag{3-8}$$

A necessary and sufficient condition for the existence of a non-trivial solution to Eq. (3-8) is that the determinant of the co-efficient matrix is zero. Eq. (3-9) can be obtained:

$$(e^{ikh})^2 + \left[\left(\frac{\mu_2 C_{t1}}{\mu_1 C_{t2}} + \frac{\mu_1 C_{t2}}{\mu_2 C_{t1}}\right) \sin\left(\frac{\omega h_2}{C_{t2}}\right) \sin\left(\frac{\omega h_1}{C_{t1}}\right) - 2\cos\left(\frac{\omega h_2}{C_{t2}}\right) \cos\left(\frac{\omega h_1}{C_{t1}}\right) \right] e^{ikh} + 1 = 0 \tag{3-9}$$

Eq. (3-9) is a quadratic equation with one unknown e^{ikh}. Assume the solution of the unknown is X_1 and X_2, according to Vieta's formulas:

$$X_1 + X_2 = 1 \qquad (3\text{-}10)$$

Therefore, $X_1 = e^{ikh}$ and $X_2 = e^{-ikh}$, according to Vieta's formulas, Eq. (3-11) can be written as follows:

$$e^{ikh} + e^{-ikh} = 2\cos\left(\frac{\omega h_2}{C_{t2}}\right)\cos\left(\frac{\omega h_1}{C_{t1}}\right) - \left(\frac{\mu_2 C_{t1}}{\mu_1 C_{t2}} + \frac{\mu_1 C_{t2}}{\mu_2 C_{t1}}\right)\sin\left(\frac{\omega h_2}{C_{t2}}\right)\sin\left(\frac{\omega h_1}{C_{t1}}\right) \qquad (3\text{-}11)$$

$$e^{ix} = \cos x + i \sin x \qquad (3\text{-}12)$$

Applying Euler's formula in Eqs. (3-12) to (3-11), the dispersion relation for ω as a function of k is given as:

$$\cos(k \cdot h) = \cos(\frac{\omega h_1}{C_{t1}})\cos(\frac{\omega h_2}{C_{t2}}) - \frac{1}{2}(\frac{\rho_1 C_{t1}}{\rho_2 C_{t2}} + \frac{\rho_2 C_{t2}}{\rho_1 C_{t1}})\sin(\frac{\omega h_1}{C_{t1}})\sin(\frac{\omega h_2}{C_{t2}}) \qquad (3\text{-}13)$$

The right-hand side of Eq. (3-13) is between -1 and 1, owing to $|\cos(k \cdot h)| \leq 1$. For any ω, if k is a real number, the Eq. (3-13) is satisfied; if k is a complex number, ω is located in the band gap frequency range. When k is in the first Brillouin zone,[34] i.e., $k \in [-\pi/h, \pi/h]$ are all considered, the dispersion curve can be drawn. Following the same procedure, one can derive a similar result in the case of longitudinal waves.

Fig. 3.2 shows an example of two materials: concrete and rubber; they are used to fabricate the periodic foundation. The material and dimensional properties are detailed in Section 5.1.1. The thickness of both layers is $h_1 = h_2 = 0.2$m. The curves are related to real wave numbers, and the frequency band gaps are related to complex wave numbers, which are not calculated and don't appear in Fig. 3.2. The first two band gaps of the transverse wave are 12.7 Hz-30.9 Hz and 35.5 Hz-61.8 Hz. The first band gap of the longitudinal mode is from 46.0 Hz to 117.7 Hz, and the second band gap is from 135.2 Hz-235.2 Hz.

3.2   Basic Theories of 2D Periodic Foundations

Consider a particle in isotropic linear elastic solid of infinite extension: In the absence of external forces, and omitting the quadratic term and damping, the governing equations in the XY plane vibration for the continuum, are

$$(\lambda+2\mu)\frac{\partial^2 u}{\partial x^2}+\mu\frac{\partial^2 u}{\partial y^2}+(\lambda+\mu)\frac{\partial^2 v}{\partial x \partial y}=\rho\frac{\partial^2 u}{\partial t^2} \tag{3-14}$$

$$(\lambda+2\mu)\frac{\partial^2 v}{\partial y^2}+\mu\frac{\partial^2 v}{\partial x^2}+(\lambda+\mu)\frac{\partial^2 u}{\partial x \partial y}=\rho\frac{\partial^2 v}{\partial t^2} \tag{3-15}$$

Where u *and* v are displacement in the X and Y directions, respectively, ρ is the material density, and μ, λ are Lamé constants,

The Bloch's theorem[34] focuses on an inhomogeneous medium, which exhibits special periodicity. According to the Bloch's theorem, therefore, the material constants in Eqs. (3-14) and (3-15) can all be expanded in the Fourier series.

$$\rho(\mathbf{r})=\sum_{\mathbf{G}}\rho(\mathbf{G})e^{i\mathbf{G}\cdot\mathbf{r}} \tag{3-16}$$

$$\lambda(\mathbf{r})=\sum_{\mathbf{G}}\lambda(\mathbf{G})e^{i\mathbf{G}\cdot\mathbf{r}} \tag{3-17}$$

$$\mu(\mathbf{r})=\sum_{\mathbf{G}}\mu(\mathbf{G})e^{i\mathbf{G}\cdot\mathbf{r}} \tag{3-18}$$

$$\mathbf{G}=n_x\mathbf{b}_1+n_y\mathbf{b}_2 \tag{3-19}$$

$$\mathbf{b}_1=\frac{2\pi}{a}i \quad \mathbf{b}_2=\frac{2\pi}{a}j \tag{3-20}$$

Where $\mathbf{r}$ is the coordinate vector, $\mathbf{r}=\{x, y\}$; n_x, n_y, are the integral numbers, and $\mathbf{b}_1$, $\mathbf{b}_2$ are the basis Fourier wave-vector in the X and Y directions, respectively; a is the dimension of one unit cell. In this case, the periodicity is two-dimensional, and the corresponding

reciprocal-lattice vector **G** has the same dimensionality. According to Eqs. (3-16) to (3-18), the material properties in Eqs. (3-14) and (3-15) can be written as periodic functions in periodic materials; Eqs. (3-16) to (3-18) sum up all the Fourier wave-vectors. The displacement u(r), therefore, can be expressed as:

$$\mathbf{u}(\mathbf{r},t) = e^{i(\mathbf{k}\cdot\mathbf{r}-\omega t)}\sum_{\mathbf{G}}\mathbf{u_k}(\mathbf{G})e^{i\mathbf{G}\cdot\mathbf{r}} \tag{3-21}$$

Where **k** is the Bloch wave vector and ω is the circular frequency of the wave. The plane wave expansion method is illustrated as an example solution to the equations.

A square lattice periodic plate with three components is shown in Fig. 3.3; A, B, and C are three different components. In this model, it is assumed that the plate only deforms in the X-Y plane and that bending deformation is ignored.
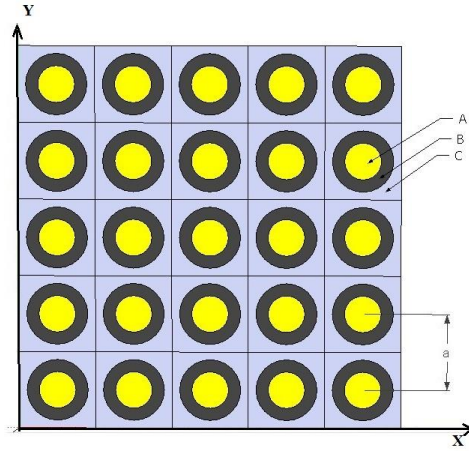
Fig. 3.3 A three-components square lattice periodic structure

According to the boundary conditions of a thin plate, the stress and strain relationships can be obtained[89] as follows:

$$\sigma_{xx} = \frac{E}{1-v^2}\left(\frac{\partial u}{\partial x}+v\frac{\partial v}{\partial y}\right) \tag{3-22}$$

32

$$\sigma_{yy} = \frac{E}{1-v^2}\left(\frac{\partial v}{\partial y} + v\frac{\partial u}{\partial x}\right) \tag{3-23}$$

$$\sigma_{xy} = \mu\left(\frac{\partial u}{\partial y} + v\frac{\partial v}{\partial x}\right) \tag{3-24}$$

$$\sigma_{xz} = \sigma_{yz} = \sigma_{zz} = 0 \tag{3-25}$$

Where E is Young's modulus, μ is the shear modulus and v is the Poisson ratio; u and v are the displacement in the X and Y directions, respectively. The following governing equations of the periodic plate can be obtained by applying Newton's Second Law in the absence of external forces:

$$\rho\frac{\partial^2 u}{\partial t^2} = \frac{\partial \sigma_{xx}}{\partial x} + \frac{\partial \sigma_{xy}}{\partial y} \tag{3-26}$$

$$\rho\frac{\partial^2 v}{\partial t^2} = \frac{\partial \sigma_{yx}}{\partial x} + \frac{\partial \sigma_{yy}}{\partial y} \tag{3-27}$$

Substituting Eqs. (3-22) to (3-25) into Eqs. (3-26) and (3-27), one obtains:

$$\frac{E}{1-v^2}\left(\frac{\partial^2 u}{\partial x^2} + v\frac{\partial^2 v}{\partial x\partial y}\right) + \mu\left(v\frac{\partial^2 u}{\partial y^2} + \frac{\partial^2 v}{\partial x\partial y}\right) = \rho\frac{\partial^2 u}{\partial t^2} \tag{3-28}$$

$$\mu\left(\frac{\partial^2 u}{\partial x\partial y} + \frac{\partial^2 v}{\partial x^2}\right) + \frac{E}{1-v^2}\left(\frac{\partial^2 v}{\partial y^2} + v\frac{\partial^2 u}{\partial x\partial y}\right) = \rho\frac{\partial^2 v}{\partial t^2} \tag{3-29}$$

For the three-component unit cell, the Fourier coefficient ρ (**G**), μ (**G**) and v (**G**) can be expressed uniformly as:

$$f(\mathbf{G}) = \frac{1}{s}\int_{cell} f(\mathbf{r})exp(-i\mathbf{G}\cdot\mathbf{r})d^2r \tag{3-30}$$

Where $s = a^2$ is the area of one unit cell. The filling ratios of material A and material B are defined as F_1 and F_2.

$$F_1 = \frac{(\pi R_1^2)}{a^2} \tag{3-31}$$

$$F_2 = \frac{\pi \left(R_2^2 - R_1^2 \right)}{a^2} \tag{3-32}$$

When **G**=0,

$$f(\mathbf{G}) = f_A F_1 + f_B F_2 + f_C \left(1 - F_1 - F_2 \right) \tag{3-33}$$

When **G**≠0,

$$
\begin{aligned}
f(\mathbf{G}) &= \frac{1}{s} f_A \int_A exp\left(-i\mathbf{G}\cdot\mathbf{r}\right) d^2 r + \frac{1}{s} f_B \int_B exp\left(-i\mathbf{G}\cdot\mathbf{r}\right) d^2 r + \frac{1}{s} f_C \int_C exp\left(-i\mathbf{G}\cdot\mathbf{r}\right) d^2 r \\
&= \frac{1}{s} f_A \int_A exp\left(-i\mathbf{G}\cdot\mathbf{r}\right) d^2 r + \frac{1}{s} f_B \int_B exp\left(-i\mathbf{G}\cdot\mathbf{r}\right) d^2 r + \frac{1}{s} f_C \int_{cell} exp\left(-i\mathbf{G}\cdot\mathbf{r}\right) d^2 r \\
&\quad - \frac{1}{s} f_C \int_A exp\left(-i\mathbf{G}\cdot\mathbf{r}\right) d^2 r - \frac{1}{s} f_C \int_B exp\left(-i\mathbf{G}\cdot\mathbf{r}\right) d^2 r \\
&= \frac{1}{s}\left(f_A - f_C \right) \int_A exp\left(-i\mathbf{G}\cdot\mathbf{r}\right) d^2 r + \frac{1}{s}\left(f_B - f_C \right) \int_B exp\left(-i\mathbf{G}\cdot\mathbf{r}\right) d^2 r + \frac{1}{s} f_C \int_{cell} exp\left(-i\mathbf{G}\cdot\mathbf{r}\right) d^2 r
\end{aligned}
$$

$$\tag{3-34}$$

Because

$$\int_{cell} exp\left(-i\mathbf{G}\cdot\mathbf{r}\right) d^2 r = 0 \tag{3-35}$$

the Fourier coefficient $f(\mathbf{G})$ can be simplified as:

$$f(\mathbf{G}) = \frac{1}{s}\left(f_A - f_C \right) \int_A exp\left(-i\mathbf{G}\cdot\mathbf{r}\right) d^2 r + \frac{1}{s}\left(f_B - f_C \right) \int_B exp\left(-i\mathbf{G}\cdot\mathbf{r}\right) d^2 r \tag{3-36}$$

Let

$$P(\mathbf{G}) = \frac{1}{s} \iint e^{-i\mathbf{G}\cdot\mathbf{r}} d^2 r \tag{3-37}$$

P (**G**) is called the structure function, which is decided by the array of unit cells.

When the unit cells are in a square arrangement for the 2D periodic foundation,

$$P(\mathbf{G}) = 2f \frac{J_1(GR)}{GR} \tag{3-38}$$

Where J_1 is the Bessel function of the first kind.

For the three-component 2D periodic foundation, the structure function of material A is:

$$P_A(\mathbf{G}) = \frac{1}{s} \int_A exp(-i\mathbf{G} \cdot \mathbf{r}) d^2 r = \frac{1}{s} \frac{2\pi R_1 J_1(GR_1)}{G} \tag{3-39}$$

Similarly, for the structure function of material B:

$$P_B(\mathbf{G}) = \frac{1}{s} \int_B exp(-i\mathbf{G} \cdot \mathbf{r}) d^2 r = \frac{1}{s} \int_{A+B} exp(-i\mathbf{G} \cdot \mathbf{r}) d^2 r - \frac{1}{s} \int_B exp(-i\mathbf{G} \cdot \mathbf{r}) d^2 r$$
$$= \frac{1}{s} \frac{2\pi R_2 J_1(GR_2)}{G} - \frac{1}{s} \frac{2\pi R_1 J_1(GR_1)}{G} \tag{3-40}$$

By substituting $P_A(\mathbf{G})$ and $P_B(\mathbf{G})$ into Eq. (3-36), we obtain:

$$f(\mathbf{G}) = \begin{cases} f_A F_1 + f_B F_2 + f_C(1 - F_1 - F_2), \mathbf{G} = 0 \\ (f_A - f_B)P_A(\mathbf{G}) + (f_B - f_C)P_B(\mathbf{G}), \mathbf{G} \neq 0 \end{cases} \tag{3-41}$$

The coefficients in Eqs. (3-28) and (3-29) are periodic functions. According to Bloch's theory, the displacements in Eqs. (3-28) and (3-29) can be expressed in the Fourier expansion:[66]

$$u(\mathbf{r},t) = e^{i(\mathbf{k} \cdot \mathbf{r} - \omega t)} u_{\mathbf{k}}(\mathbf{r}) = e^{-i\omega t} \sum_{\mathbf{G}} u_{\mathbf{k}+\mathbf{G}} e^{i(\mathbf{k}+\mathbf{G}) \cdot \mathbf{r}} \tag{3-42}$$

Where k is the wave vector in the reciprocal space, ω is the angular frequency, and $\mathbf{u}_k(\mathbf{r})$ the wave amplitude. By substituting the periodic functions of displacement in Eq. (3-42) and the periodic functions of material properties from Eqs. (3-39) to (3-41) into the governing equations of motion from Eqs. (3-28) and (3-29), one can obtain the

characteristic equations for the XY mode of periodic structures, i.e., Eqs. (3-43) and (3-44) in the X and Y directions, respectively.[90]

$$\omega^2 \sum_{\mathbf{G}'} \rho(\mathbf{G}''-\mathbf{G}') u_{\mathbf{k}+\mathbf{G}'}$$

$$= \sum_{\mathbf{G}'} \left[\alpha(\mathbf{G}''-\mathbf{G}')(\mathbf{k}+\mathbf{G}')_x (\mathbf{k}+\mathbf{G}'')_x + \mu(\mathbf{G}''-\mathbf{G}')(\mathbf{k}+\mathbf{G}')_y (\mathbf{k}+\mathbf{G}'')_y \right] u_{\mathbf{k}+\mathbf{G}'} \qquad (3\text{-}43)$$

$$+ \sum_{\mathbf{G}'} \left[\beta(\mathbf{G}''-\mathbf{G}')(\mathbf{k}+\mathbf{G}')_y (\mathbf{k}+\mathbf{G}'')_x + \mu(\mathbf{G}''-\mathbf{G}')(\mathbf{k}+\mathbf{G}')_x (\mathbf{k}+\mathbf{G}'')_y \right] v_{\mathbf{k}+\mathbf{G}'}$$

$$\omega^2 \sum_{\mathbf{G}'} \rho(\mathbf{G}''-\mathbf{G}') v_{\mathbf{k}+\mathbf{G}'}$$

$$= \sum_{\mathbf{G}'} \left[\beta(\mathbf{G}''-\mathbf{G}')(\mathbf{k}+\mathbf{G}')_x (\mathbf{k}+\mathbf{G}'')_y + \mu(\mathbf{G}''-\mathbf{G}')(\mathbf{k}+\mathbf{G}')_y (\mathbf{k}+\mathbf{G}'')_x \right] u_{\mathbf{k}+\mathbf{G}'} \qquad (3\text{-}44)$$

$$+ \sum_{\mathbf{G}'} \left[\alpha(\mathbf{G}''-\mathbf{G}')(\mathbf{k}+\mathbf{G}')_y (\mathbf{k}+\mathbf{G}'')_y + \mu(\mathbf{G}''-\mathbf{G}')(\mathbf{k}+\mathbf{G}')_x (\mathbf{k}+\mathbf{G}'')_x \right] v_{\mathbf{k}+\mathbf{G}'}$$

Where $\mathbf{G}''=\mathbf{G}+\mathbf{G}'$, $\alpha = \dfrac{E}{1-v^2}$, $\beta = \dfrac{Ev}{1-v^2}$.

If wave vector $\mathbf{k}$ is given in the First Brillouin zone, and $\mathbf{G}$ is given points in the reciprocal space, then a set of Eigen vectors $u_{\mathbf{k}+\mathbf{G}'}$ and Eigen values ω can be obtained. In other words, to get the curve of attenuation zones, by selecting wave vector $\mathbf{k}$ in the first Brillouin zone, a series of ω can be obtained.[34] The next paragraph explains the Brillouin zone of square lattice periodic structure.

In mathematics and solid-state physics, the first Brillouin zone is uniquely defined as a primitive cell in reciprocal space. The boundaries of this cell are given by planes related to points on the reciprocal lattice as shown in Fig. 3.4. The first Brillouin zone reduced by all of the symmetries in the point group of the lattice is shown in Fig. 3.5. In high symmetric periodic structures, the first Brillouin zone is the typical area for finding the boundary conditions using Bloch theory; see Eq. (3-21), for example. The relationship between Eigen-frequency and wave vector, therefore, can be obtained. The

wave vector **k** for waves that travel along the boundary of the first Brillouin zone can be used to obtain the corresponding ω. The relationship between ω and k is called dispersion curve or dispersion relationship.
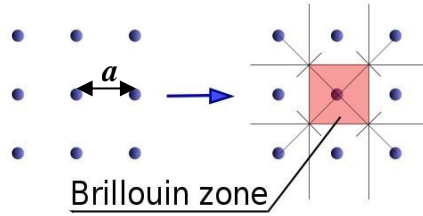
Fig. 3.4 Brillouin zone of 2D periodic structures
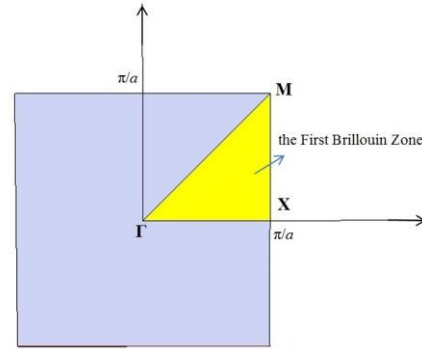
Fig. 3.5 The first Brillouin zone of 2D periodic structures

Fig. 3.6 shows the relationship between the wave vector **k** and Eigen values ω of the 2D periodic foundation with the geometric and material properties in Section 5.2.1. The wave vector travelling through three vertices Γ, X, and M of the first Brillouin zone, as shown in the horizontal axis in Fig. 3.6 and the corresponding ω, is shown in the vertical axis in Fig. 3.6. The frequency band in yellow, 41.2 Hz-58.7 Hz, is shown as the frequency band gap, which means the propagation of the wave is blocked.
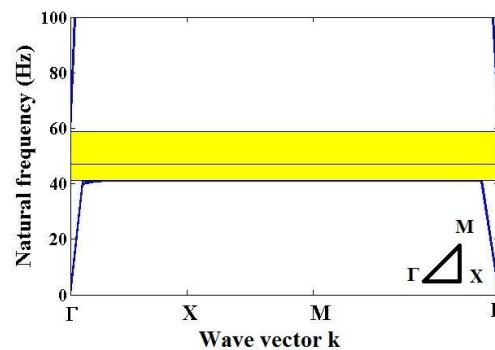
Fig. 3.6 Theoretical solution of the first band gap of 2D periodic foundation

37

3.3   Basic Theory of 3D Periodic Foundations

In the phononic crystal, many 3D structures are reported including simple cubic (SC), body-centered cubic (BCC), and face-centered cubic (FCC).[91]-[94] The PWE method is used for 2D periodic structure analysis. The multiple scattering theory (MST) is also used in 3D periodic acoustic composites and the band structures of a phononic crystal consisting of complex and frequency-dependent Lamé coefficients.[66]-[69] The MST method, however, is only used for sphere scatters of 3D periodic structures and cylinder scatters for 2D periodic structures; the PWE method encounters convergence problems when the composites of the phononic crystal show a great difference in Young's modulus. The finite difference time domain (FDTD) method is suitable for handling different geometric structures and the convergence problem, but it requires considerable calculation.[63]

3.3.1   Basic equations of elastic wave

Three basic equations can be written for linear elastic isotropic material:

(1) Differential equation of motion;

$$\sigma_{ij,j} + \rho f_i = \rho \ddot{u}_i \qquad (3\text{-}45)$$

(2) Equation of compatibility;

$$\varepsilon_{ij} = \left(\partial_j u_i + \partial_i u_j \right) / 2 \qquad (3\text{-}46)$$

(3) Constitutive law.

$$\sigma_{ij} = \lambda \varepsilon_{kk} \delta_{ij} + 2\mu \varepsilon_{ij} \ \text{ or } \ \varepsilon_{ij} = \left[\left(1 + \upsilon \right) \sigma_{ij} - \upsilon \sigma_{kk} \delta_{ij} \right] / E \qquad (3\text{-}47)$$

Where i, $j=x$, y, z, ρ is density, λ and μ are Lamé constants, E is Young's modulus; v is Poisson's ratio; σ_{ij}, ε_{ij}, and u_i are stress, strain, and displacement respectively. Wave equations in terms of $\mathbf{u}$ can be written as Eq. (3-48):

$$\mu\nabla^2\mathbf{u}+(\lambda+\mu)\nabla(\nabla\cdot\mathbf{u})+\rho\cdot\mathbf{f}=\rho\ddot{\mathbf{u}} \text{ or } \partial_i\left(\lambda\partial_j u_j\right)+\partial_j\left[\mu\left(\partial_j u_i+\partial_i u_j\right)\right]+\rho f_i=\rho\ddot{u}_i$$

(3-48)

3.3.2 Finite difference time domain method

The finite difference time domain method is illustrated in footnotes:[63]-[64] The Eigen-value of the periodic structure is found by the analysis of the time-dependent response of a structure on the pulse excitation. Note that the field computation is carried out within the unit cell only. The periodicity of the structure is emulated by setting up periodic boundary conditions. Such conditions define the radiation wave vector by tuning the phase of the radiation when translating it from one side of the unit cell to another. After the field computation is completed, the Fourier transform is applied, which yields the response spectrum. Eigen-states of the periodic structure correspond to local maxima of the spectrum since the Eigen-state is the resonant frequency of the structure, which means the phase-conditions, noted above as a way to define the radiation wave vector, support radiation propagation inside the infinite structure.

In general, the band gap structure computation using FDTD should be carried out as follows:[64]

1. Determine the computation area.

2. Set up periodic boundary conditions.

3. Define the radiation excitation function: The radiation spectrum should be wide enough to cover whole investigated frequency ranges.

39

4. Carry out spectral analysis of the time-dependent response of the structure on the probe pulse by searching all local maxima and plotting them over the frequency axis.

5. Repeat steps 2 to 4 at different values of the phase shift in the periodic boundary conditions corresponding to all selected points within the Brillouin zone for which the band structure is computed.

In this FDTD method, the displacement, velocity, and stress are used as the basis to describe variables in material, the equation of motion and constitutive law, and to develop the difference-equations. According to the wave equation, and considering the elastic isotropic materials, the wave equations without body force can be expressed as Eqs. (3-49) and (3-50):

$$\rho(\mathbf{r})\ddot{u}_i(\mathbf{r},t) = \partial_j \sigma_{ij}(\mathbf{r},t) \tag{3-49}$$

$$\sigma_{ij}(\mathbf{r},t) = C_{ijkl}(\mathbf{r})\partial_l u_k(\mathbf{r},t) \tag{3-50}$$

The first-order wave equations without body force can be expressed as Eqs. (3-51) and (3-51):

$$\rho(\mathbf{r})\dot{v}_i(\mathbf{r},t) = \partial_j \sigma_{ij}(\mathbf{r},t) \tag{3-51}$$

$$\dot{\sigma}_{ij}(\mathbf{r},t) = C_{ijkl}(\mathbf{r})\partial_l v_k(\mathbf{r},t) \tag{3-52}$$

where $\mathbf{r}=(x,y,z)$, C_{ijkl} is elastic tensor shown as Eq. (3-53).

$$C_{ijkl}(\mathbf{r}) = \lambda(\mathbf{r})\delta_{ij}\delta_{kl} + \mu(\mathbf{r})\left(\delta_{ik}\delta_{jl} + \delta_{il}\delta_{jk}\right) \tag{3-53}$$

Then, the equation can be written in the matrix as Eqs. (3-54) and (3-55).

$$\begin{bmatrix} \dot{v}_x \\ \dot{v}_y \\ \dot{v}_z \end{bmatrix} = \frac{1}{\rho} \begin{bmatrix} \sigma_{xx} & \sigma_{xy} & \sigma_{xz} \\ \sigma_{yx} & \sigma_{yy} & \sigma_{yz} \\ \sigma_{zx} & \sigma_{zy} & \sigma_{zz} \end{bmatrix} \begin{bmatrix} \partial_x \\ \partial_y \\ \partial_z \end{bmatrix} \tag{3-54}$$

$$
\begin{bmatrix} \dot{\sigma}_{xx} \\ \dot{\sigma}_{yy} \\ \dot{\sigma}_{zz} \\ \dot{\sigma}_{yz} \\ \dot{\sigma}_{xz} \\ \dot{\sigma}_{xy} \end{bmatrix} = \begin{bmatrix} \lambda+2\mu & \lambda & \lambda & 0 & 0 & 0 \\ \lambda & \lambda+2\mu & \lambda & 0 & 0 & 0 \\ \lambda & \lambda & \lambda+2\mu & 0 & 0 & 0 \\ 0 & 0 & 0 & \mu & 0 & 0 \\ 0 & 0 & 0 & 0 & \mu & 0 \\ 0 & 0 & 0 & 0 & 0 & \mu \end{bmatrix} \begin{bmatrix} \partial_x v_x \\ \partial_y v_y \\ \partial_z v_z \\ \partial_y v_z + \partial_z v_y \\ \partial_x v_z + \partial_z v_x \\ \partial_y v_x + \partial_x v_y \end{bmatrix}
\tag{3-55}
$$

The position of the staggered grids is defined by these discrete wave equations. Fig. 3.7 shows the unit of the staggered grids in the calculation of the FDTD method and the relationship between the velocity grids and the stress grids.
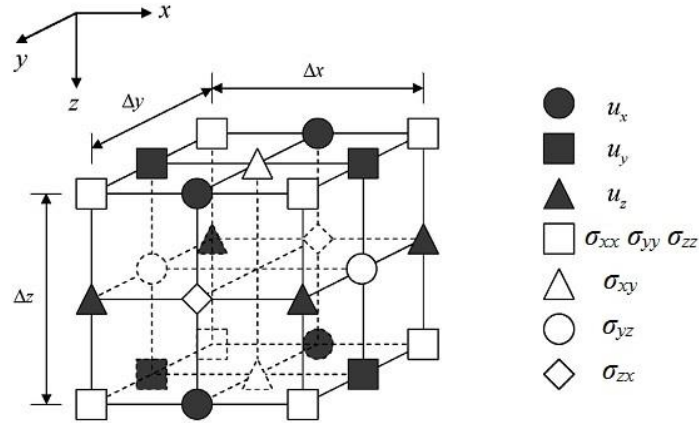
Fig. 3.7 The unit of the grids in the FDTD method[63]

After the discrete procedure, the first-order difference equations of the velocity and stress are Eqs. (3-56) to (3-64):

$$
\begin{aligned}
\frac{v_x^{i+1/2,j,k;n+1/2} - v_x^{i+1/2,j,k;n-1/2}}{\Delta t} &= \frac{1}{\rho^{i+1/2,j,k}} \Big(\frac{\sigma_{xx}^{i+1,j,k;n} - \sigma_{xx}^{i,j,k;n}}{\Delta x} \\
&+ \frac{\sigma_{xy}^{i+1/2,j+1/2,k;n} - \sigma_{xy}^{i+1/2,j-1/2,k;n}}{\Delta y} + \frac{\sigma_{zx}^{i+1/2,j,k+1/2;n} - \sigma_{zx}^{i+1/2,j,k-1/2;n}}{\Delta z} \Big)
\end{aligned}
\tag{3-56}
$$

$$
\begin{aligned}
\frac{v_y^{i,j+1/2,k;n+1/2} - v_y^{i,j+1/2,k;n-1/2}}{\Delta t} &= \frac{1}{\rho^{i,j+1/2,k}} \Big(\frac{\sigma_{xy}^{i+1/2,j+1/2,k;n} - \sigma_{xy}^{i-1/2,j+1/2,k;n}}{\Delta x} \\
&+ \frac{\sigma_{yy}^{i,j+1,k;n} - \sigma_{yy}^{i,j,k;n}}{\Delta y} + \frac{\sigma_{yz}^{i,j+1/2,k+1/2;n} - \sigma_{yz}^{i,j+1/2,k-1/2;n}}{\Delta z} \Big)
\end{aligned}
\tag{3-57}
$$

41

$$\frac{v_z^{i,j,k+1/2;n+1/2} - v_z^{i,j,k+1/2;n-1/2}}{\Delta t} = \frac{1}{\rho^{i,j,k+1/2}}(\frac{\sigma_{zx}^{i+1/2,j,k+1/2;n} - \sigma_{zx}^{i-1/2,j,k+1/2;n}}{\Delta x}$$

$$+\frac{\sigma_{yz}^{i,j+1/2,k+1/2;n} - \sigma_{yz}^{i,j-1/2,k+1/2;n}}{\Delta y} + \frac{\sigma_{zz}^{i,j,k+1;n} - \sigma_{zz}^{i,j,k;n}}{\Delta z})$$

(3-58)

$$\frac{\sigma_{xx}^{i,j,k;n+1} - \sigma_{xx}^{i,j,k;n}}{\Delta t} = (\lambda^{i,j,k} + 2\mu^{i,j,k})\frac{v_x^{i+1/2,j,k;n+1/2} - v_x^{i-1/2,j,k;n+1/2}}{\Delta x}$$

$$+\lambda^{i,j,k}\frac{v_y^{i,j+1/2,k;n+1/2} - v_y^{i,j-1/2,k;n+1/2}}{\Delta y} + \lambda^{i,j,k}\frac{v_z^{i,j,k+1/2;n+1/2} - v_z^{i,j,k-1/2;n+1/2}}{\Delta z}$$

(3-59)

$$\frac{\sigma_{yy}^{i,j,k;n+1} - \sigma_{yy}^{i,j,k;n}}{\Delta t} = \lambda^{i,j,k}\frac{v_x^{i+1/2,j,k;n+1/2} - v_x^{i-1/2,j,k;n+1/2}}{\Delta x}$$

$$+(\lambda^{i,j,k} + 2\mu^{i,j,k})\frac{v_y^{i,j+1/2,k;n+1/2} - v_y^{i,j-1/2,k;n+1/2}}{\Delta y} + \lambda^{i,j,k}\frac{v_z^{i,j,k+1/2;n+1/2} - v_z^{i,j,k-1/2;n+1/2}}{\Delta z}$$

(3-60)

$$\frac{\sigma_{zz}^{i,j,k;n+1} - \sigma_{zz}^{i,j,k;n}}{\Delta t} = \lambda^{i,j,k}\frac{v_x^{i+1/2,j,k;n+1/2} - v_x^{i-1/2,j,k;n+1/2}}{\Delta x}$$

$$+\lambda^{i,j,k}\frac{v_y^{i,j+1/2,k;n+1/2} - v_y^{i,j-1/2,k;n+1/2}}{\Delta y} + (\lambda^{i,j,k} + 2\mu^{i,j,k})\frac{v_z^{i,j,k+1/2;n+1/2} - v_z^{i,j,k-1/2;n+1/2}}{\Delta z}$$

(3-61)

$$\frac{\sigma_{xy}^{i+1/2,j+1/2,k;n+1} - \sigma_{xy}^{i+1/2,j+1/2,k;n}}{\Delta t} = \mu^{i+1/2,j+1/2,k}(\frac{v_x^{i+1/2,j+1,k;n+1/2} - v_x^{i+1/2,j,k;n+1/2}}{\Delta y}$$

$$+\frac{v_y^{i+1,j+1/2,k;n+1/2} - v_y^{i,j+1/2,k;n+1/2}}{\Delta x})$$

(3-62)

$$\frac{\sigma_{yz}^{i,j+1/2,k+1/2;n+1} - \sigma_{yz}^{i,j+1/2,k+1/2;n}}{\Delta t} = \mu^{i,j+1/2,k+1/2}(\frac{v_y^{i,j+1/2,k+1;n+1/2} - v_y^{i,j+1/2,k;n+1/2}}{\Delta z}$$

$$+\frac{v_z^{i,j+1,k+1/2;n+1/2} - v_z^{i,j,k+1/2;n+1/2}}{\Delta y})$$

(3-63)

$$\frac{\sigma_{zx}^{i+1/2,j,k+1/2;n+1} - \sigma_{zx}^{i+1/2,j,k+1/2;n}}{\Delta t} = \mu^{i+1/2,j,k+1/2}(\frac{v_z^{i+1,j,k+1/2;n+1/2} - v_z^{i,j,k+1/2;n+1/2}}{\Delta x}$$

$$+\frac{v_x^{i+1/2,j,k+1;n+1/2} - v_x^{i+1/2,j,k;n+1/2}}{\Delta z})$$

(3-64)

Boundary conditions were applied to the unit cell to calculate the dispersion curves of the periodic structures. The periodic boundary conditions are satisfied with Bloch's theorem. The velocity and stress components in the periodic structure, therefore, can be expressed as follows:

$$v_i\left(\mathbf{x}+a,t\right)=e^{i\mathbf{k}\cdot a}v_i\left(\mathbf{x},t\right) \tag{3-65}$$

$$\sigma_{ij}\left(\mathbf{x}+a,t\right)=e^{i\mathbf{k}\cdot a}\sigma_{ij}\left(\mathbf{x},t\right) \tag{3-66}$$

Then, expanding Eqs. (3-65) and (3-66) to get the discrete forms of the surface normal to the X, Y, and Z axes, shows the boundary conditions for the FDTD method in Eqs. (3-67) to (3-84) are:

Normal to X axis:

$$v_x^{-1/2,j,k;n}=e^{ik_1a}v_x^{a-1/2,j,k;n} \tag{3-67}$$

$$v_y^{0,j+1/2,k;n}=e^{ik_1a}v_y^{a,j+1/2,k;n} \tag{3-68}$$

$$v_z^{0,j,k+1/2;n}=e^{ik_1a}v_z^{a,j,k+1/2;n} \tag{3-69}$$

$$\sigma_{xx}^{0,j,k;n}=e^{ik_1a}\sigma_{xx}^{a,j,k;n} \tag{3-70}$$

$$\sigma_{xy}^{-1/2,j+1/2,k;n}=e^{ik_1a}\sigma_{xy}^{a-1/2,j+1/2,k;n} \tag{3-71}$$

$$\sigma_{zx}^{-1/2,j,k+1/2;n}=e^{ik_1a}\sigma_{zx}^{a-1/2,j,k+1/2;n} \tag{3-72}$$

Normal to Y axis:

$$v_x^{i+1/2,0,k;n}=e^{ik_2a}v_x^{i+1/2,a,k;n} \tag{3-73}$$

$$v_y^{i,-1/2,k;n}=e^{ik_2a}v_y^{i,a-1/2,k;n} \tag{3-74}$$

$$v_z^{i,0,k+1/2;n}=e^{ik_2a}v_z^{i,a,k+1/2;n} \tag{3-75}$$

$$\sigma_{xy}^{i+1/2,-1/2,k;n}=e^{ik_2a}\sigma_{xy}^{i+1/2,a-1/2,k;n} \tag{3-76}$$

$$\sigma_{yy}^{i,0,k;n}=e^{ik_2a}\sigma_{yy}^{i,a,k;n} \tag{3-77}$$

$$\sigma_{zy}^{i,-1/2,k+1/2;n} = e^{ik_2a}\sigma_{zy}^{i,a-1/2,k+1/2;n} \tag{3-78}$$

Normal to Z axis:

$$v_x^{i+1/2,j,0;n} = e^{ik_3a}v_x^{i+1/2,j,a;n} \tag{3-79}$$

$$v_y^{i,j+1/2,0;n} = e^{ik_3a}v_y^{i,j+1/2,a;n} \tag{3-80}$$

$$v_z^{i,j,-1/2;n} = e^{ik_3a}v_z^{i,j,a-1/2;n} \tag{3-81}$$

$$\sigma_{zx}^{i+1/2,j,-1/2;n} = e^{ik_3a}\sigma_{zx}^{i+1/2,j,a-1/2;n} \tag{3-82}$$

$$\sigma_{zy}^{i,j+1/2,-1/2;n} = e^{ik_3a}\sigma_{zy}^{i,j+1/2,k-1/2;n} \tag{3-83}$$

$$\sigma_{zz}^{i,j,0;n} = e^{ik_3a}\sigma_{zz}^{i,j,a;n} \tag{3-84}$$

Where $\mathbf{k}=(k_1,k_2,k_3)$ are wave vectors.

Excitation from a single point of the computation region is considered as the excitation. It is widely known that the spectrum of the delta-pulse is infinitely wide so that it gives structural responses at any frequency. After the delta-pulse is introduced, the excitation is turned off; however, owing to periodic boundary conditions, radiation exists for infinite duration in the structure without absorption. In the case of delta-pulse, the excitation function takes the following form:

$$\delta\left(x-x_0, y-y_0, z-z_0, t-t_0\right)=1 \tag{3-85}$$

After the pulse response of the structure is obtained, it should be analyzed. The time-dependent response of the structure could be found at any point of the computational domain. Next, the fast Fourier transform (FFT) is used to obtain the discreet spectrum. Then, the resonant frequencies of the periodic structure can be obtained. The resonant points are the existing peaks in the frequency spectra. When $\mathbf{k}$

travels through the first Brillouin zones of the 3D periodic structures, the band structures can be obtained.

3.3.3 Theoretical solutions of 3D test specimens by COMSOL

COMSOL can be used to find the theoretical solution of a 3D periodic structure; in this section we will see COMSOL used to obtain frequency band gaps for a test specimen. Fig. 3.8 shows that the first absolute band gap is 32.9 Hz-35.6 Hz, which blocks the elastic waves in three directions, X, Y, and Z for both the S wave and P wave. The seismogram can be decoupled, however, in three directions, and, by using ABAQUS, we can find the attenuation zones in the X, Y, and Z directions of 3D periodic foundations composed of finite unit cells.
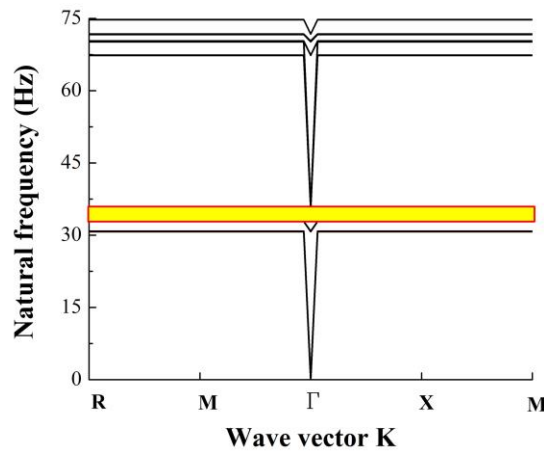
Fig. 3.8 Theoretical band gap for 3D periodic foundation solved by COMSOL

4 FINITE ELEMENT MODELING OF PERIODIC FOUNDATIONS

This section shows parametric studies conducted for 1D, 2D, and 3D periodic structures with infinite unit cells to obtain wider and lower band gaps for seismic resistance. The factors for parametric study include material properties and geometric properties such as density, Young's modulus of materials, size of unit cells, etc. With the results obtained from the parametric study, the test specimens of 1D, 2D, and 3D periodic foundations with finite unit cells are designed according to the analysis results of the parametric study. We see in this chapter the attenuation zones of 1D, 2D, and 3D periodic foundations obtained using ABAQUS.

4.1 FE Modeling of 1D Layered Periodic Foundations

4.1.1 Parametric study of 1D periodic foundations

A periodic foundation is composed of two materials as one unit: the rubber layer and the concrete layer. Many units repeat along the vertical direction to compose a 1D periodic foundation; this kind of periodic foundation reduces dynamic response. The effects of material and geometric properties of 1D periodic structures on the first band gap are discussed in this section, with both longitudinal and transverse waves, using the method mentioned in Section 3.1. Fig. 4.1 shows one unit cell of a 1D periodic structure for parametric study: A is the rubber layer, and B is the concrete layer. The thickness ratio is defined as the ratio between the thicknesses of layer A relative to that of layer B. To conduct the parametric study, the parameter to be investigated is selected, and other parameters are fixed. The relationship between the parameter to be investigated and the first band gap can be plotted.

47
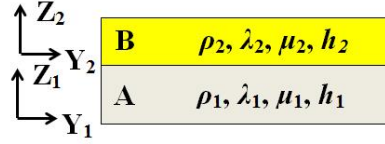
Fig. 4.1 One unit cell of 1D periodic structure

4.1.1.1 *Material Properties*

To study the material properties, the geometric properties are fixed as shown in Table 4.1; the unit cell size is 0.4m, and the thickness ratio is 1. Fig. 4.2 to Fig. 4.5 shows the effects of material properties on the frequency band gap with longitudinal wave input.

Table 4.1 The properties of 1D material parametric study

Parameters	Young's modulus of rubber (Pa)	Young's modulus of concrete (Pa)	Density of rubber (kg/m^3)	Density of concrete (kg/m^3)	Unit cell size (m)	Thickness ratio
Young's modulus of rubber (Pa)	Selected	3.14×10^{10}	1300	2300	0.4	1
Young's modulus of concrete (Pa)	5.8×10^5	Selected	1300	2300	0.4	1
Density of rubber (kg/m^3)	5.8×10^5	3.14×10^{10}	Selected	2300	0.4	1
Density of concrete (kg/m^3)	5.8×10^5	3.14×10^{10}	1300	Selected	0.4	1
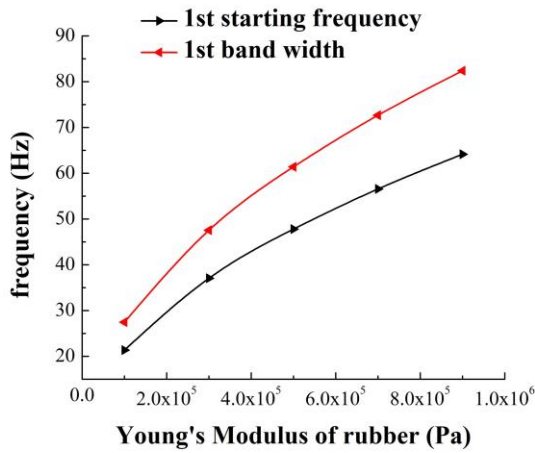
Fig. 4.2 Young's modulus of rubber vs. the first band gap with longitudinal wave
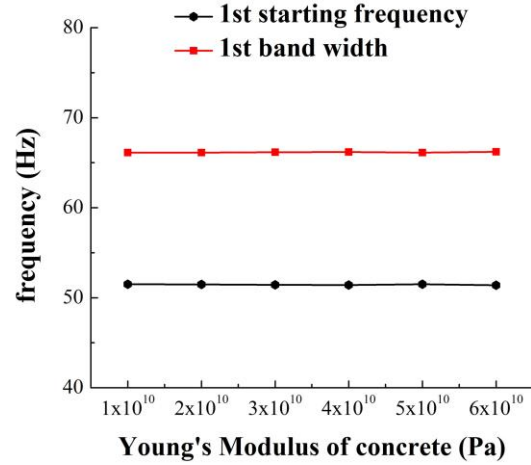
Fig. 4.3 Young's modulus of concrete vs. the first band gap with longitudinal wave

Fig. 4.2 shows the effect of Young's modulus of rubber (layer) on the starting frequency and the bandwidth of the first band gap. The other parameters were fixed and Young's modulus of rubber changed from 1×10^5 Pa to 9×10^5 Pa. Both the starting frequency and the bandwidth increase with the increasing of Young's modulus of rubber. Fig. 4.3 shows the effect of Young's modulus of concrete changing from 1×10^{10} Pa to 6×10^{10} Pa. The Young's modulus of concrete has no effect on the first band gap.

Fig. 4.4 shows the relationship between the first frequency band gaps and the density of concrete. The first starting frequency decreases, and the bandwidth increases as the density of the concrete layer increases. Greater concrete density, therefore, leads to a lower and wider first frequency band gap. Fig. 4.5 shows the effects of rubber density on the first frequency band gap. Although the density of rubber has little effect on the first starting frequency, the bandwidth of the first band gap decreases rapidly with the increase of rubber density.
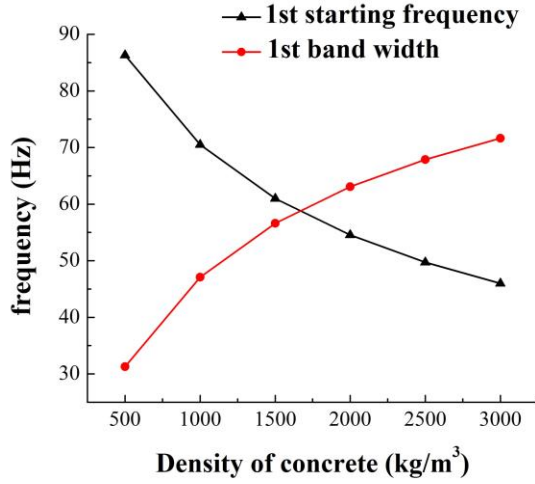
Fig. 4.4 Density of concrete vs. the first band gap with longitudinal wave
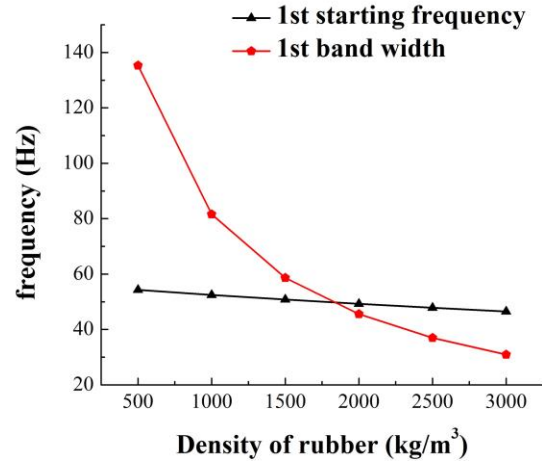
Fig. 4.5 Density of rubber vs. the first band gap with longitudinal wave

Fig. 4.6 to Fig. 4.9 show the effects of material properties on the first band gaps with transverse wave input. When compared to Fig. 4.2 to Fig. 4.5, the effects of transverse wave input show results similar to those of longitudinal wave input. To obtain lower first starting frequency, lower Young's modulus of rubber, and greater concrete density are desireable. Greater Young's modulus of rubber, and concrete density, with less rubber density, lead to a wider frequency bandwidth for both longitudinal and transverse wave input.
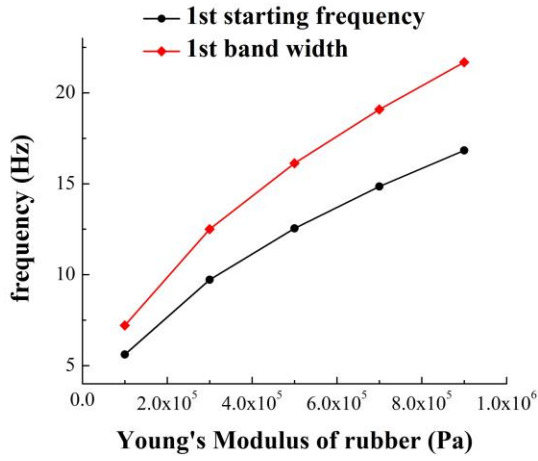
Fig. 4.6 Young's modulus of rubber vs. the first band gap with transverse wave
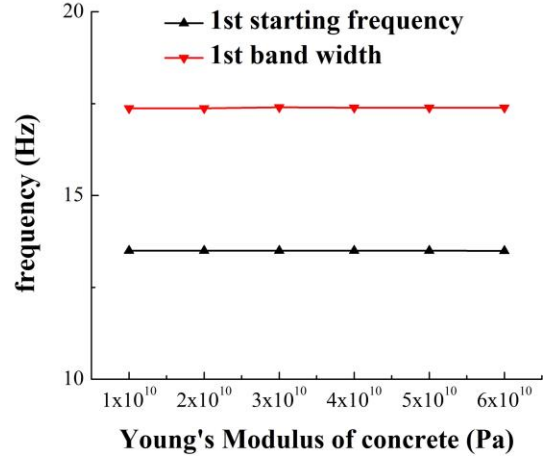
Fig. 4.7 Young's modulus of concrete vs. the first band gap with transverse wave
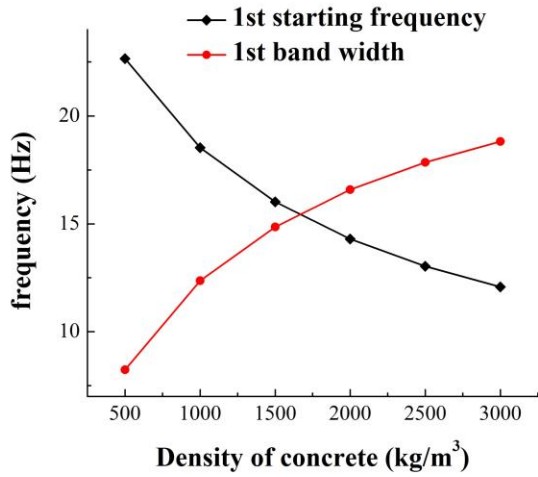
Fig. 4.8 Density of concrete vs. the first band gap with transverse wave
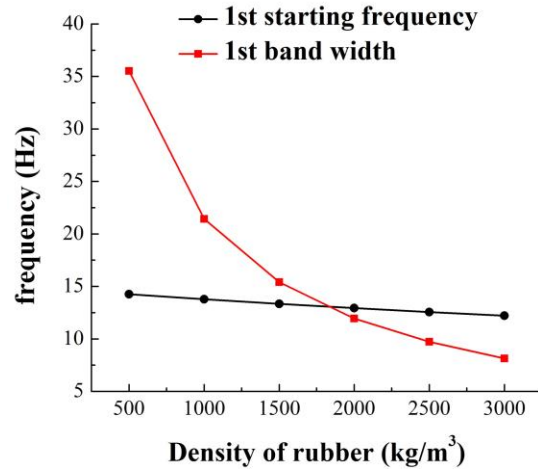
Fig. 4.9 Density of rubber vs. the first band gap with transverse wave

4.1.1.2 Geometric Properties

There are two main geometric dimensions for a unit cell in the 1D periodic structure: unit cell size and thickness-ratio material-properties are kept constant for all the cases, shown in Table 4.2, and two investigated parameters, i.e., unit cell size and

thickness ratio, are used for plotting the curve between the first band gap and the investigated parameters.

Table 4.2 The properties of 1D geometrical parametric study

Parameters	Young's modulus of rubber (Pa)	Young's modulus of concrete (Pa)	Density of rubber (kg/m^3)	Density of concrete (kg/m^3)	Unit cell size (m)	Thickness ratio
Young's modulus of rubber (Pa)	5.8×10^5	3.14×10^{10}	1300	2300	0.4	Selected
Young's modulus of concrete (Pa)	5.8×10^5	3.14×10^{10}	1300	2300	Selected	1

Fig. 4.10 to Fig. 4.12 show the first band gap vs. the geometric properties with longitudinal wave input. The relationship between the thickness ratio and the starting frequency of the first band gap is plotted in Fig. 4.10; the thickness ratio changes from 0.5 to 5. The starting frequency first decreases then increases after 1.5. The bandwidth of the first band gap decreases with an increase in the thickness ratio, as shown in Fig. 4.11. Fig. 4.12 shows the effects on the unit cell size. A lower starting frequency of the first band gap can be obtained with an increase of the unit cell size.
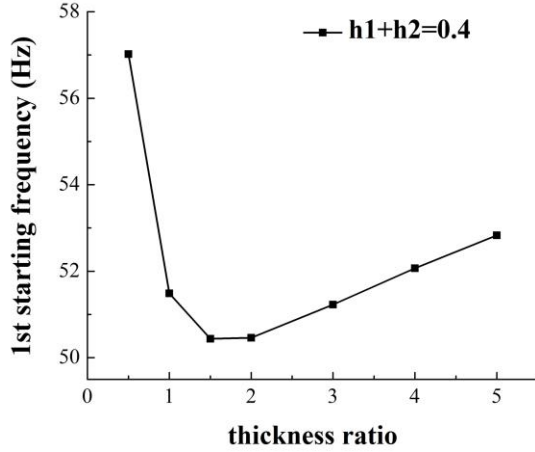
Fig. 4.10 Thickness ratio vs. the starting frequency of first band gap with longitudinal wave
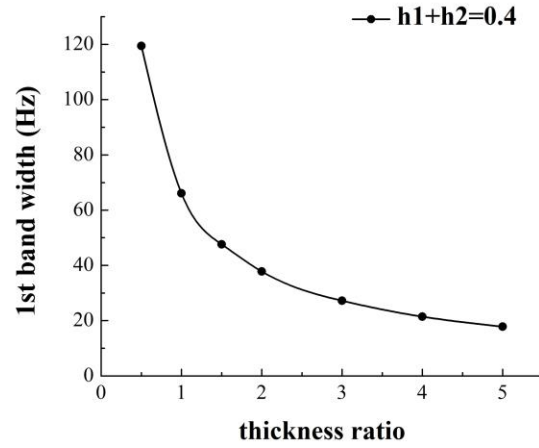
Fig. 4.11 Thickness ratio vs. the starting frequency width of first band gap with longitudinal wave
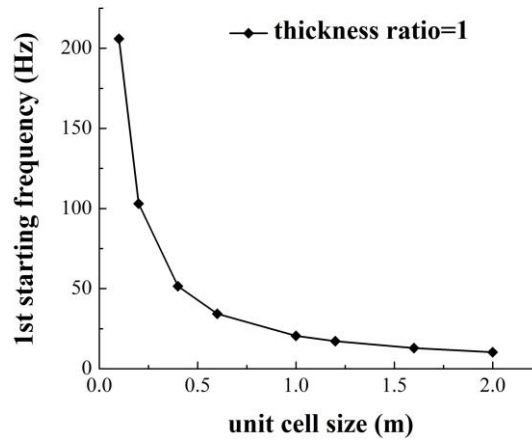
Fig. 4.12 Unit cell size vs. first band gap with longitudinal wave

The first frequency band gap with the transverse wave input is shown in Fig. 4.13 to Fig. 4.15. The same conclusions can be drawn as with an increase of the thickness ratio; the bandwidth of the first band gap decreases, and the lowest starting frequency band gap can be obtained when the thickness ratio is equal to 1.5. The lower frequency band gap can be obtained with a larger unit cell size.
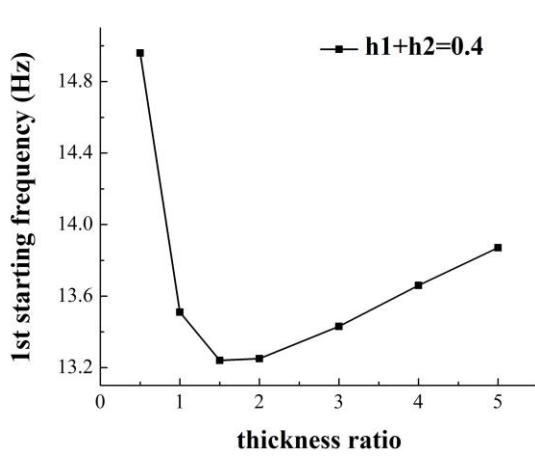
Fig. 4.13 Thickness ratio vs. the starting frequency of first band gap with transverse wave
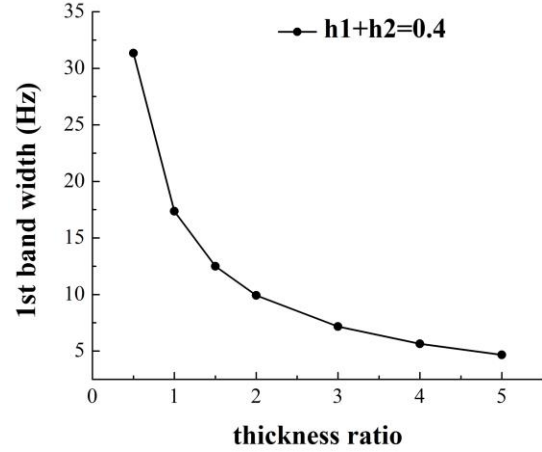
Fig. 4.14 Thickness ratio vs. the starting frequency width of first band gap with transverse wave
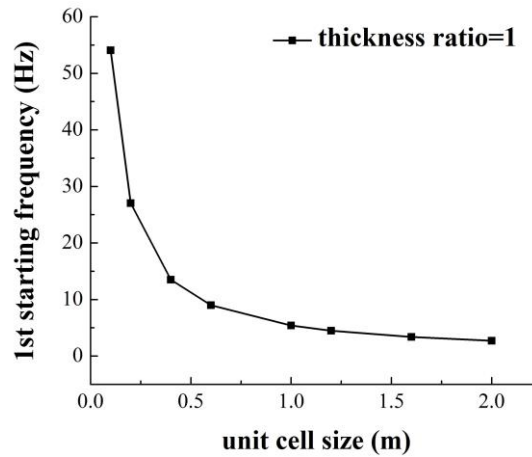
Fig. 4.15 Unit cell size vs. first band gap with transverse wave

To summarize: when both main factors of the first frequency band gap are considered in the 1D parametric study, i.e., the starting frequency and the bandwidth, the test yields a thickness ratio of 1 and a unit cell size of 0.4m for the 1D periodic foundation.

4.1.2 FE modeling of 1D periodic foundations using ABAQUS

This section shows the development of a 1D finite element model using the finite element analysis commercial software ABAQUS to investigate the band gaps of the

periodic foundation. The corresponding geometric and material properties are introduced as follows:

(1) Geometric and material properties:

The periodic foundation studied, with a size of 1.0 m×1.0 m×1.0 m, as shown in Fig. 4.16, included three concrete layers and two rubber layers, where the thickness of each layer was 0.2 m. A steel frame was fixed on the top of the foundation. The cross-section dimensions of the box-section beams were 0.03 m×0.06 m with a thickness of 0.0032 m, and the cross-section dimensions of the columns was 0.06 m×0.06 m with a thickness of 0.0032 m. The thickness of each of the slabs on the frame was 0.003 m. At each column and beam joint, a 5 kg mass was attached. The parameters for 1D periodic foundations and the material properties are shown in Table 4.3 and Table 4.4.

Table 4.3 Parameters of one unit cell of 1D periodic foundations

Part Name	Thickness (m)
Rubber layer	0.2
Concrete layer	0.2

Table 4.4 Material properties of 1D periodic foundation tests

Material	Density (kg/m^3)	Young's Modulus (Pa)	Poisson's Ratio
Rubber	$1.3×10^3$	$5.8×10^5$	0.463
Steel frame	$7.85×10^3$	$2.05×10^{11}$	0.28
Concrete	$2.3×10^3$	$3.144×10^{10}$	0.33

(2) Element types:

The quadratic element type was adopted for all the modeling elements in this study, since it has the advantage of improving accuracy of analysis. In addition, the reduced integration element type selected was rubber; this integration algorithm can avoid the volume-locking phenomena for those materials with a Poisson's ratio of about

0.5, such as the rubber used in this case. Specifically, the elements include: (a) S8R, an 8-node doubly-curved thick-shell with reduced integration for slabs on the frame; (b) B32, a 3-node quadratic beam in space for beams and columns of the frame; (c) C3D20R, a 20-node quadratic brick with reduced integration for concrete and rubber layers of the foundation.

(3) Constraints:

The steel frame was fixed on a periodic foundation. The slabs were tied to the steel frame, and the concrete and rubber layers in the periodic foundation were tied together.

(4) Boundary conditions:

To simulate the S wave excitations, the displacements in the X direction and the rotations with respect to the X, Y, and Z axes were free, while the displacements in the Y and Z directions were restrained at the bottom surface of the periodic foundation. At the bottom surface, an instantaneous displacement with a unity of an excitation frequency from 0 to 100 Hz was applied in the X direction. The boundary conditions are shown in Fig. 4.16. To simulate the P wave input, the displacements in the Y direction, and the rotations with respect to the X, Y, and Z axes were free, while the displacements in the X and Z directions were restrained at the bottom surface of the periodic foundation. At the bottom surface, an instantaneous displacement with a unity at an excitation frequency of 0 to 100 Hz was applied in the X direction. The boundary conditions are shown in Fig. 4.17.
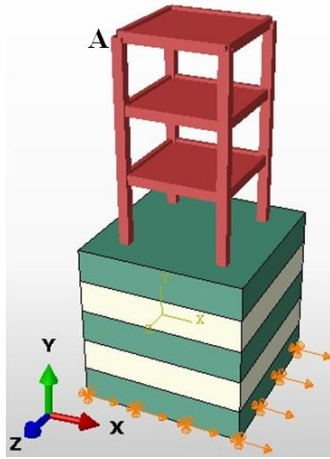
Fig. 4.16 The boundary conditions of
1D periodic foundation under S wave
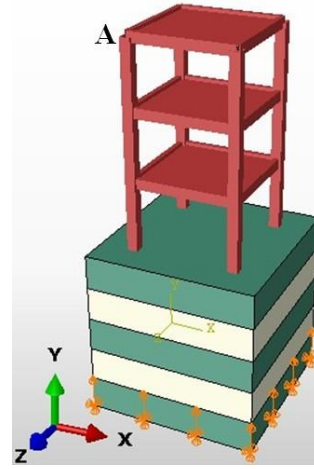
Fig. 4.17 The boundary conditions of
1D periodic foundation under P wave

To assess the efficiency of the periodic foundation in the frequency domain, a frequency response function (FRF) was defined as 20 log(δ_o/δ_i). An instantaneous displacement in the X direction with amplitude of δ_i was applied at the bottom. The displacement in the X direction of node A at the top of the frame was denoted by δ_o. When the output δ_o was equal to the input δ_i, the value of FRF equaled zero. The black dashed curve shown in Fig. 4.18 and Fig. 4.19 represents the FRF of node A on the frame without the periodic foundation, while the red curve shows the FRF of node A on the frame with the periodic foundation. The predicated FRF in the case with the periodic foundation is evidently reduced when compared to that without the periodic foundation. This phenomenon indicates that the periodic foundation can lower the dynamic response of the upper structures. In addition, Fig. 4.18 shows that, for this specific strucutre on the periodic foundation, the first, second, and third attenuation zones are in the range of 12 Hz-19 Hz, 20.5 Hz-53.5 Hz, and 30.5 Hz-55 Hz, respectively. The first three attenuation zones for the P wave excitation shown in Fig. 4.19 are 25 Hz-41 Hz, 48 Hz-53.5 Hz, and 53.5 Hz-62 Hz.
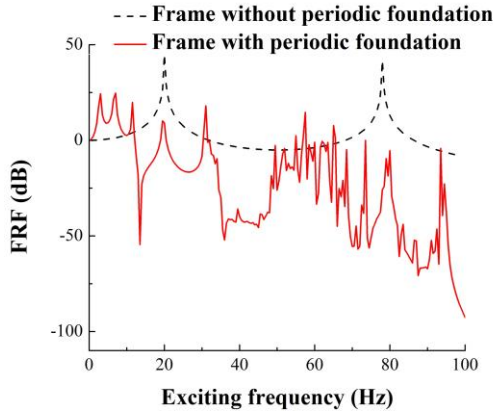
Fig. 4.18 FRF of node A under S wave

Fig. 4.19 FRF of node A under P wave

4.2   FE Modeling of 2D Periodic Foundations

4.2.1   FE modeling of 2D periodic foundations using COMSOL

The FE method was applied to predict the band gaps of the periodic structures with infinite unit cells. The parametric study was conducted to find lower and wider band gaps of periodic structures with infinite unit cells. The model of one unit of a 2D periodic foundation, as shown in Fig. 4.20, was developed in the FEA program using the commercial software COMSOL (2013) to do the optimized design. The periodic boundary conditions can be applied easily to the four sides of the cell in COMSOL. In this way, the model was assumed to be an infinite plate consisting of infinite cells having the same size. Then, the Eigen frequency problem is solved to find the band gaps that theory introduced (above), this case being the same as the case assumed in theory. Many variables can affect the band gaps and bandwidths of the 2D periodic foundation.[95] To analyze the effects of these two parameters separately, the following two new parameters were defined: the filling ratio, $f = \dfrac{\pi r_b^2}{a^2}$, and the ratio of the radius of the core cylinder to

the thickness of the rubber layer $\beta = \dfrac{r_a}{r_b - r_a}$. To obtain the optimized lower first band gap

and wider bandwidth, four variables were investigated, namely, the core density, Young's

modulus of the rubber layer, the ratio of the radius of the core cylinder to the thickness of

the rubber layer β, and the filling ratio, f. The parameters used for each analysis are listed

in Table 4.5.
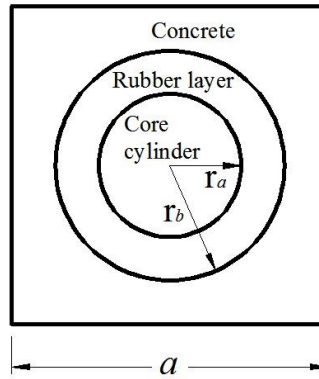
Fig. 4.20 One unit cell of 2D periodic foundation

Table 4.5 The properties of 2D parametric study

Parameters	Geometrical properties			Core cylinder material properties		
	β	f	a	ρ_{core}	E_{core}	v_{core}
Core density	1.5	50%	0.25	Selected	1.65×10^{11}	0.275
Young's modulus of rubber	1.5	50%	0.25	7184	1.65×10^{11}	0.275
β	Selected	50%	0.25	7184	1.65×10^{11}	0.275
f	1.5	Selected	0.25	7184	1.65×10^{11}	0.275
	Rubber material properties			Concrete material properties		
Core density	ρ_{rub}	E_{rub}	v_{rub}	ρ_{con}	E_{con}	v_{con}
Young's modulus of rubber	1196	5.7×10^{5}	0.463	2300	3.144×10^{10}	0.33
β	1196	Selected	0.463	2300	3.144×10^{10}	0.33
f	1196	5.7×10^{5}	0.463	2300	3.144×10^{10}	0.33
Core density	1196	5.7×10^{5}	0.463	2300	3.144×10^{10}	0.33

4.2.1.1   Material Properties

Five different materials with very different densities were chosen as the core cylinders: aluminum, iron, steel, copper, and lead. Fig. 4.21 presents the relationships between core density and the first band gap. With the increase of core cylinder density, the starting frequency of the first band gap decreases from 70 Hz to 32 Hz, and the bandwidth of the first band gap increases from 3.5 Hz to 5 Hz. The results indicated that for earthquake seismograms, which usually have lower frequencies, lower than 10 Hz, Cu and Pb are the preferred materials to obtain the lower band gaps.
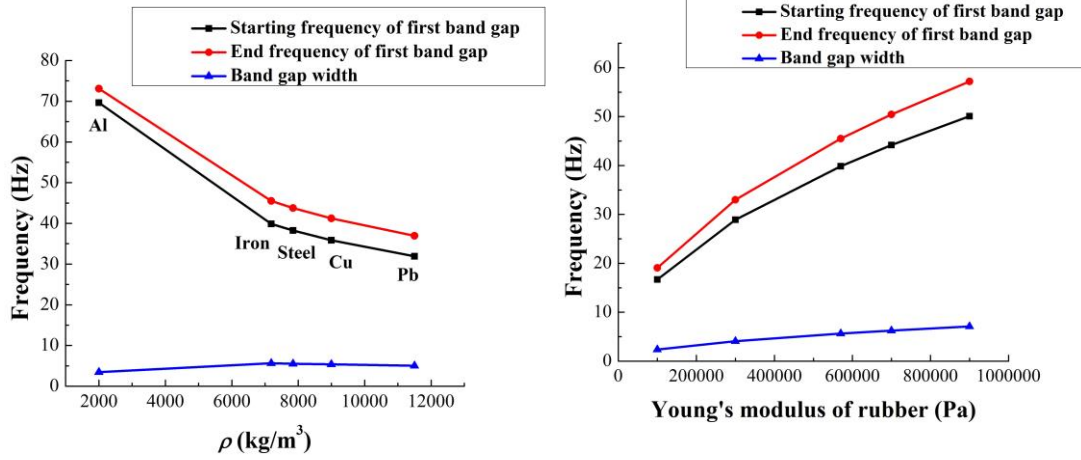
Fig. 4.21 Core density vs. the first band gap

Fig. 4.22 Young's modulus of rubber layer vs. the first band gap

Fig. 4.22 shows that a smaller Young's modulus can provide a lower starting frequency of the first band gap starting at 16.7 Hz. This phenomenon may be partly explained by the characteristics of the 2D periodic foundation. The whole unit can be considered as a spring oscillator system, and the steel cylinder and concrete can be taken as the mass. The rubber layer between the core cylinder and concrete can be considered as a spring. Then, according to the frequency equation, i.e., $\omega = \sqrt{\dfrac{k}{m}}$, the larger the k is, the higher the ω. In this system, k is Young's modulus of the rubber.

60

4.2.1.2 Geometric Properties

To study the effects of geometrical properties, β was selected with a constant f =50% to get the first band gap curve. The predicted results are plotted in Fig. 4.23, from which it can be observed that the starting frequency of the first band gap, first decreases with the increase of β, then increases. In addition, the starting frequency reaches its lowest value when β=1.5 in this case.

For the effects of the filling ratio, the value of β=1.5 is fixed, and f is selected. Fig. 4.24 indicates that, with the increase of f, a smaller starting frequency of the band gap can be obtained, but a smaller band gap width is also provided.

The most optimized parameters, therefore, were chosen according to the above analysis. In a practical design, considering the bearing capacity, a higher f means less concrete in the foundation. Therefore, f should be limited to a reasonable range. To make sure the periodic foundation has enough bearing capacity, as well as to lower the band gaps, f=50% and β=1.5 were chosen for further study.
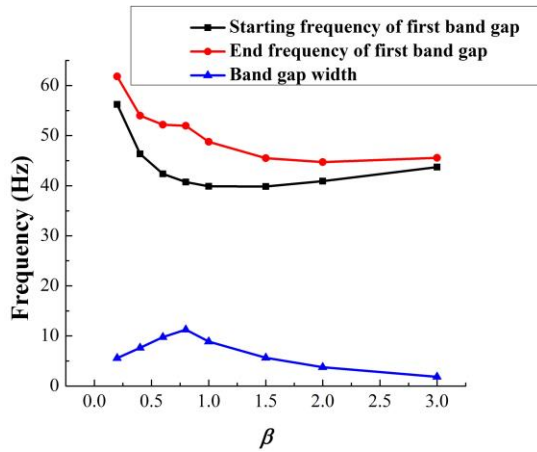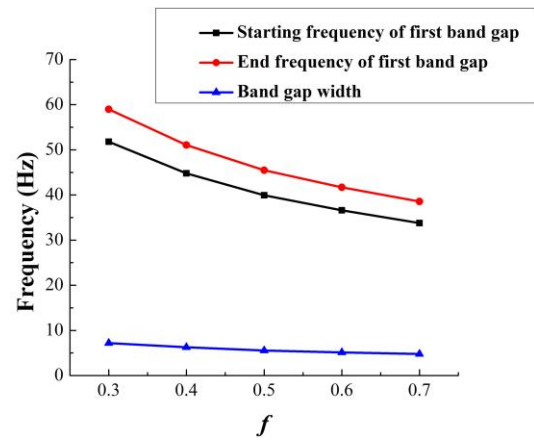
Fig. 4.23 β vs. the first band gap   Fig. 4.24 f vs. the first band gap

4.2.2 FE modeling of 2D periodic foundations using ABAQUS

A model was set up using the commercial software ABAQUS (2013) and scanning frequency analysis to learn the dynamic characteristics of the specimen with finite unit cells. The scanning frequency analysis results were comparable to the stepped sine tests in the experimental programs, which are presented in Section 5.2.5. Both the theoretical solution in Section 3.2 and the FEM solution of COMSOL in Section 4.2.1 are band gaps of the periodic structure with infinite unit cells.

The dimension of the frame and the additional mass assigned on the top of the frame are the same as those used in the test specimen detailed in Table 4.6. The steel frame was 1m high and 0.5 m wide. The column and beam members were A36 steel, with a cross-section of S 3×5.7.[96] A 5.44 kg mass was attached at each column and beam joint. The material properties, which were the same as the test specimen, are illustrated in Table 4.7, the parametric analysis results shown in Section 4.2.1 being taken into consideration.

Table 4.6 Parameters of one unit cell of 2D periodic foundations

Item	Material	Dimension
Core cylinder	Ductile cast iron	Diameter = 0.12 m.
Rubber coating	Supper soft rubber (Duro 10)	Outer diameter = 0.2 m.
Matrix	Reinforced concrete	Length of unit cell (a) = 0.254 m

Table 4.7 Material properties of 2D periodic foundation tests

Material	Density (kg/m³)	Young's Modulus (Pa)	Poisson's Ratio
Ductile cast iron	7.184×10^3	1.65×10^{11}	0.275
Supper soft rubber	1.196×10^3	5.7×10^5	0.463
Steel	7.85×10^3	2.05×10^{11}	0.28
Concrete	2.3×10^3	3.144×10^{10}	0.33

The S wave boundary conditions were applied to the model. The displacements of the bottom surface in the Y and Z directions were fixed, as shown in Fig. 4.25. These boundary conditions simulated the input motion of the horizontal component of harmonic

motion, or an earthquake. When the output displacement was 31.6% of the input displacement, the value of FRF was -10, which meant the periodic foundation significantly reduced the propagation of waves. As shown in Fig. 4.26, the ranges of the attenuation zone were 40 Hz-42.5 Hz, 43 Hz-84.5 Hz, and 86 Hz-100 Hz. Theoretically, when input waves fall within the band gaps, the response of the frame can be reduced significantly as compared to the frame response without the periodic foundation. For example, when the input wave frequency is 48.5 Hz, the FRF is -66 dB, which indicates that the amplitude of node A was 0.05% times the input amplitude.

The same analysis was conducted to learn the dynamic characteristics of the frequency band gaps in the Y direction of the P waves, as shown in Fig. 4.27; the displacements of the bottom surface in the X and Z directions were fixed, and the displacements in the Y direction were excited instantaneously. These boundary conditions simulate the input motion of the vertical component of an earthquake. The FRF of a node, A on the frame, is shown as the black curve in Fig. 4.28, and the red dashed curve is the FRF of the frame without periodic foundation. The ranges of frequency band gaps were 30 Hz-50 Hz and 52 Hz-100 Hz.
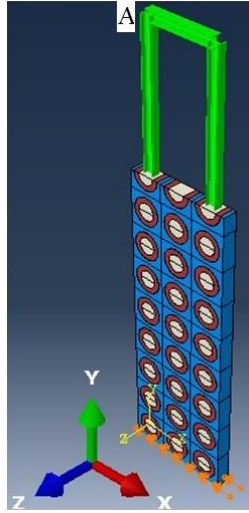
Fig. 4.25 Boundary condition
of 2D periodic foundation
under S wave
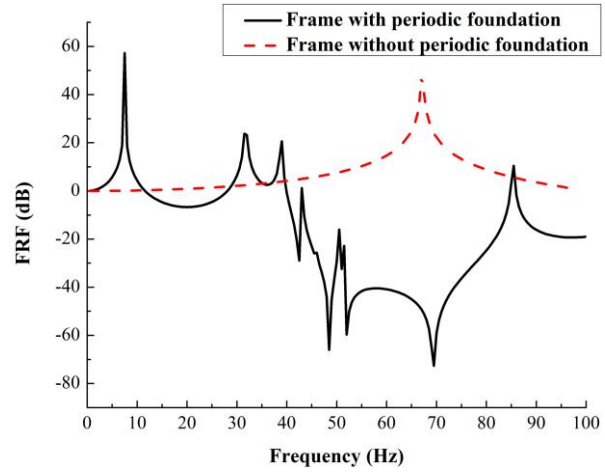
Fig. 4.26 FRF of node A in S wave
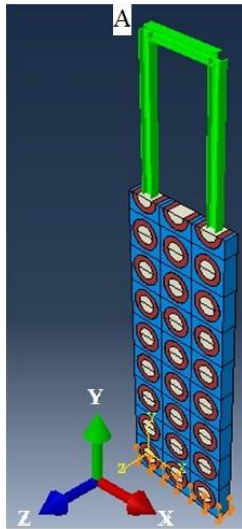
Fig. 4.27 Boundary conditions
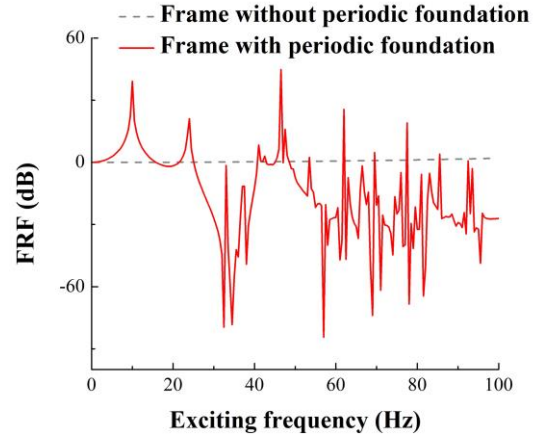of 2D periodic foundation
under P wave
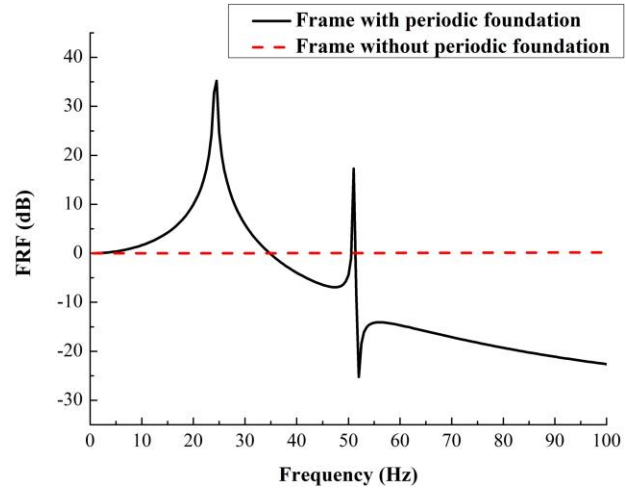
Fig. 4.28 FRF of node A in P wave

4.3   FE Modeling for 3D Periodic Foundations

4.3.1   FE modeling of 3D periodic foundations using COMSOL

Frequency band gaps of 3D periodic foundations with infinite unit cells were

calculated using COMSOL. To get lower and wider band gaps, the optimal design was

conducted for a 3D periodic foundation by taking into account the geometric dimensions and material properties as variables. The unit cell used in the analysis and the cross-section of the unit cell are shown in Fig. 4.29. To analyze separately the effects of these parameters, two new parameters were defined, including the filling ratio, $f = \frac{b^3}{a^3}$, and the ratio of the core cube side-length to the thickness of the rubber layer, $\beta = \frac{b}{t}$. In the analysis, the core cube side-length was fixed at 0.1m.
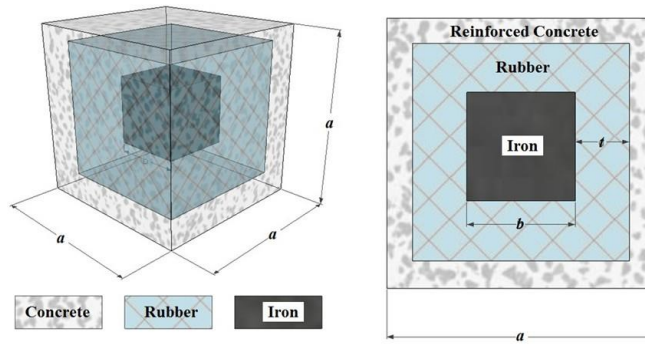
Fig. 4.29 One unit cell of 3D periodic foundation

4.3.1.1 Material Properties

According to the previous analysis, two main parameters affect the first band gap once the geometric dimensions are defined, i.e., the density of the core cube and Young's modulus of the rubber. The geometric dimensions with b=0.1 m, β=2, and f=0.524 are employed in this section to investigate the effects of the two material properties on the attenuation zones.

Fig. 4.30 shows the relationship between the core cube density and the first band gap. Five different materials were chosen for the core cubes, including aluminum, cast iron, steel, copper, and lead; their densities are 2.0×10^3 kg/m^3, 7.184×10^3 kg/m^3, 7.85×10^3 kg/m^3, 9.0×10^3 kg/m^3, and 11.5×10^3 kg/m^3, respectively.[81] With the increase of core

cube density, the starting frequency of the first band gap will decrease; in contrast, the bandwidth of the first band gap will increase.

Similarly, Fig. 4.31 shows the effects of Young's modulus of the rubber layers on the first band gap. Fig. 4.31 shows that a smaller Young's modulus will provide a lower starting frequency and smaller bandwidth than the first band gap.
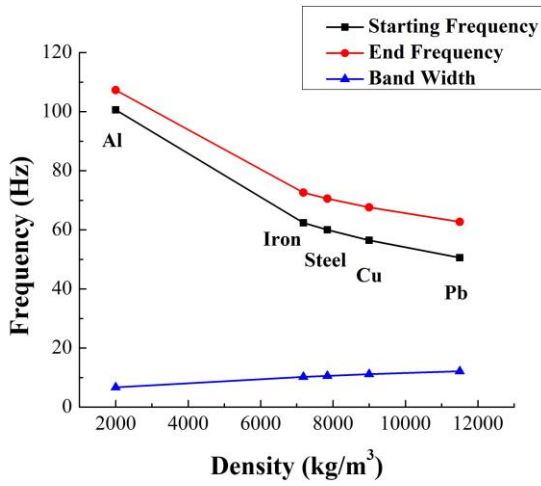
Fig. 4.30 Core density vs. the first band gap
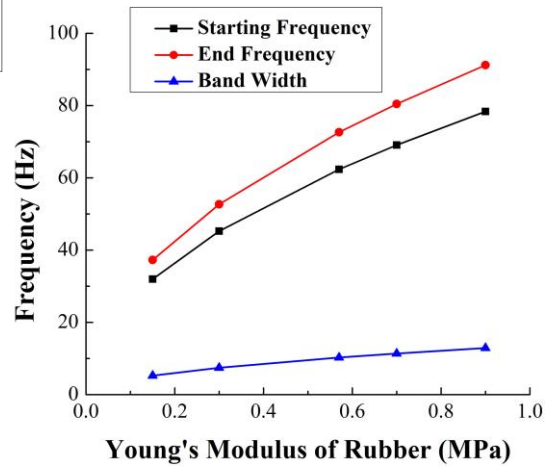
Fig. 4.31 Young's modulus of rubber vs. the first band gap

4.3.1.2 Geometric Properties

There are three main geometric dimensions for a unit cell in the 3D periodic foundation including the side-length of the core cube *b*, the thickness of the rubber *t*, and the side-length of the unit cell *a*, as shown in Fig. 4.29.

Fig. 4.32 shows the relationship between the first band gap and the filling ratio when β=2.5. With the increase of the filling ratio, the width of the first band gap increases while the starting frequencies of the first band gap stay almost the same.

Fig. 4.33 shows the relationship between β and the first band gap for f =0.524. Fig. 4.33 shows that the starting frequency of the first band gap increases with increasing β; therefore, the bandwidth has a similar trend.

66
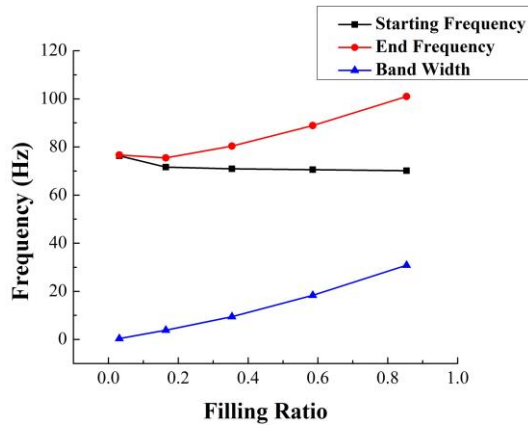
Fig. 4.32 Filling ratio vs. the first band gap   Fig. 4.33 β vs. the first band gap
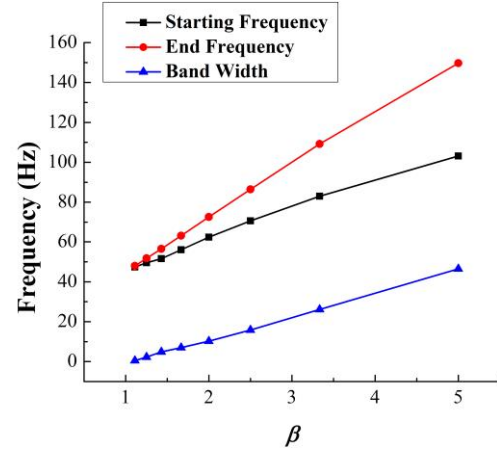
One more comparison illustrates the effects of the two parameters more clearly: The filling ratio f is considered to have four different values, 0.354, 0.465, 0.524, and 0.586. For each f, β is selected to be 1.25, 1.428, 1.667, 2, 2.5, 3.334, and 5; the results are shown in Table 4.8. For a constant β with an increase in f, the starting frequency stays about the same, while the width of the band gap increases. When f is fixed, both the starting frequency and the bandwidth increase with the increase of β. To take into account both the starting frequency and the bandwidth, therefore, one design option for specimen tests is to choose f=0.524 and β=2, where both the starting frequency and the band gap width are acceptable for the test facility.

Table 4.8 β vs. the first band gap with different f

β	$f=0.354$		$f=0.465$		$f=0.524$		$f=0.586$	
	Starting frequency	Bandwidth	Starting frequency	Bandwidth	Starting frequency	Bandwidth	Starting frequency	Bandwidth
1.25	50.38	0.83	51.22	1.71	51.8	2.29	52.12	2.9
1.428	54.98	2.88	55.79	4.19	56.51	4.88	57.28	5.71
1.667	60.49	4.3	62.19	6.06	63.08	7.02	64.29	8.13
2	68.69	6.17	71.15	8.72	72.6	10.26	74.2	11.86
2.5	80.39	9.48	84.22	13.49	86.4	15.79	88.79	18.25
3.334	98.75	15.75	104.85	21.84	109.15	26.15	112.89	30.16
5	132.65	28.31	142.86	39.69	149.68	46.5	158.75	55.59

4.3.2 FE modeling of 3D periodic foundations using ABAQUS

The ABAQUS models were developed to determine the dynamic characteristics of the specimens. Fig. 4.29 shows one unit cell of the periodic foundation and the cross-section. The dimensions of the steel column and the additional mass assigned on the top of the column were the same as those used in the test specimen, as detailed in Table 4.9. The steel column was 1m high; the column member was A36 steel, with a cross-section of S 3×5.7,[96] and the beam was 0.6m with the same cross-section as the column. A 5.44kg mass was added to the beam and column-joint or the top of the column to reduce the natural frequency of the superstructure. The material properties, which were the same as the test specimen, are also illustrated in Table 4.10.

Table 4.9 Parameters of one unit cell of 3D periodic foundations

Part name	Material	Length of side
core cube	ductile cast iron	b=102 mm
polyurethane coating	polyurethane (Oo 30)	b +2t=203 mm
matrix	concrete	a=305 mm

Table 4.10 Material properties of 3D periodic foundation tests

Material	Density (kg/m^3)	Young's Modulus (Pa)	Poisson's Ratio
Ductile cast iron	7.184×10^3	1.65×10^{11}	0.275
Polyurethane	1.277×10^3	1.586×10^5	0.463
Steel column	7.85×10^3	2.05×10^{11}	0.28
Concrete	2.3×10^3	4.0×10^{10}	0.33

The dynamic characteristics under an S wave were studied first. Fig. 4.34 presents the 3D periodic foundation with a frame on it; the 3D periodic foundation was composed of 5 by 5 unit cells, shown as Case 1. The 3D periodic foundation composed of 3 by 3 unit cells are shown as Case 2. To simplify the model, a periodic foundation with a

column was also set up with ABAQUS, shown as Case 3. Case 3 is a strip of Case 1 with the same unit cell dimensions but with different arrangements. The displacements of the bottom surface of the footing in the Y and Z directions were fixed for the ABAQUS model, and an instantaneous displacement in the X direction with an amplitude δ_i was applied at the bottom surface, as shown in Fig. 4.34. These boundary conditions simulate the input motion of the horizontal component of an earthquake. The FRFs of the three cases in Fig. 4.35 show the same trend, and to make the field tests both time and cost efficient, the model in Case 3 was tested instead of the model in Case 1 and Case 2, as shown in Fig. 4.38.
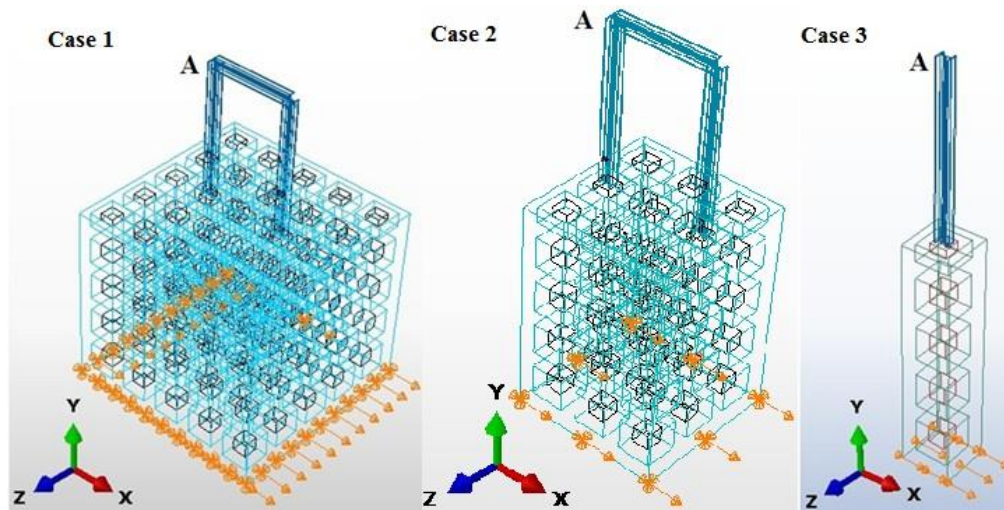
Fig. 4.34 Boundary conditions under S wave

Displacements of the bottom surface in X and Z were fixed, as shown in Fig. 4.36, to find the attenuation zones under the P wave in the Y direction, and the displacements in the Y direction were excited instantaneously. The same analysis was completed for the S wave excitation; the three cases under the P wave excitation are shown in Fig. 4.36. The three cases are named Case 4, Case 5, and Case 6. The FRF of the three cases are shown in Fig. 4.37. The FRF values of the three cases are very close;

therefore, Case 3 and Case 6 can predict the attenuation zones of the six cases. Considering cost and time efficiency, the 3D periodic foundation can be simplified as shown in Fig. 4.38.
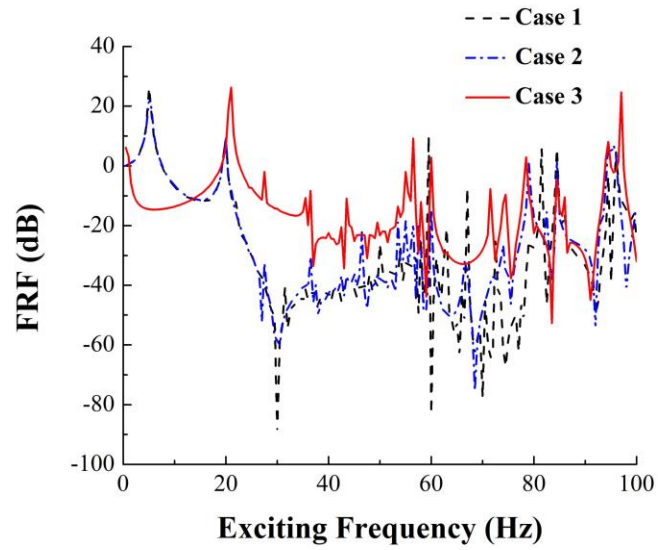
Fig. 4.35 FRF under S wave
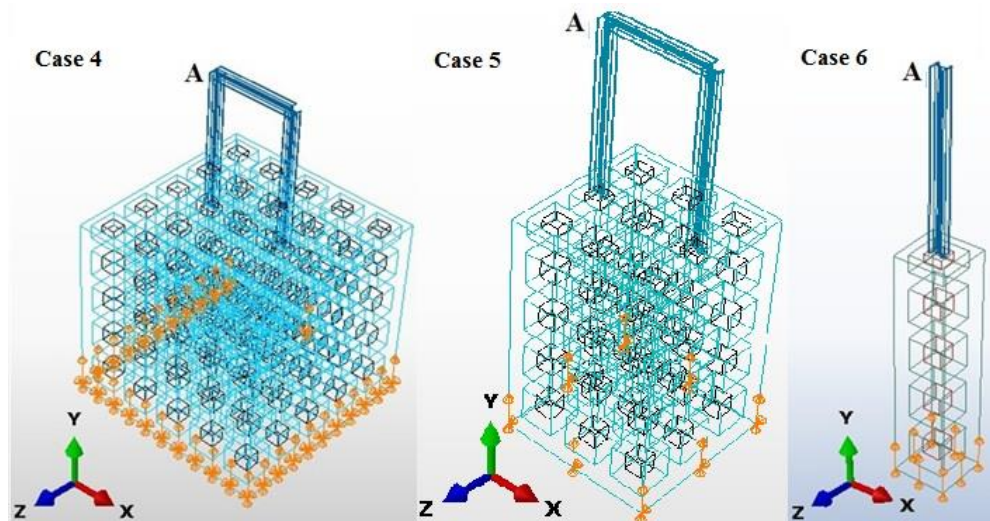
Fig. 4.36 Boundary conditions under P wave
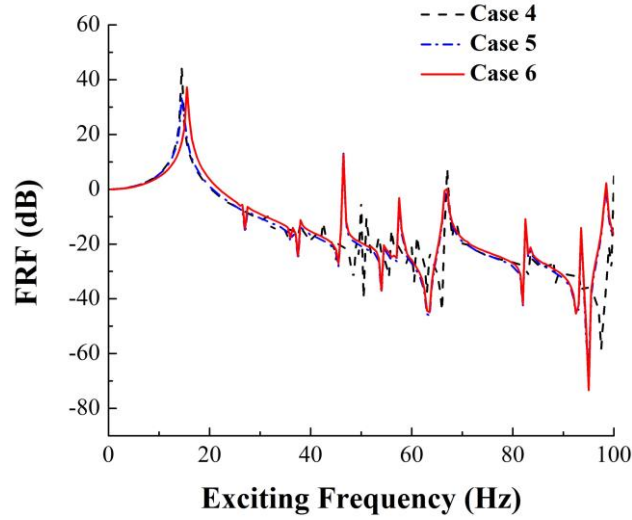
Fig. 4.37 FRF under P wave

The periodic foundation and a traditional reinforced concrete with the column were analyzed in ABAQUS. The curves are shown in Fig. 4.39; the ranges of attenuation zones under an S wave are 1.5 Hz-19 Hz, 23 Hz-56 Hz, 57 Hz-59.5 Hz, 60.5 Hz-78 Hz, 79 Hz-93.5 Hz, 95 Hz-96 Hz, and 97.5 Hz-100 Hz; the input waves are attenuated in most frequency ranges. The FRF of a node on the steel column is shown with the red curve in Fig. 4.40, and the dashed black curve is the FRF of the column without the 3D periodic foundation. The attenuation zones of a simplified 3D periodic foundation are 22 Hz-46 Hz, 47 Hz-66.5 Hz, 67.5 Hz-98 Hz, and 99 Hz-100 Hz.
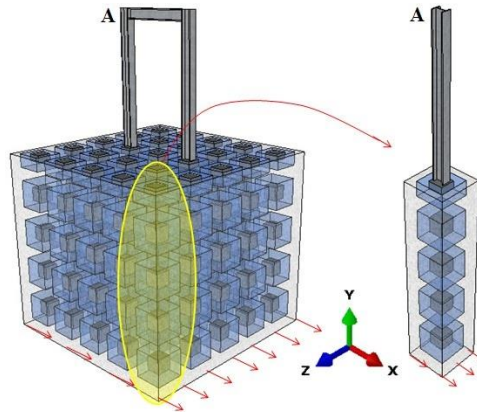
Fig. 4.38 Simplification of 3D periodic foundations

71
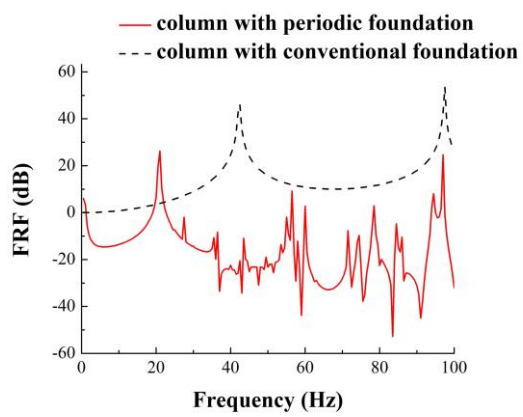
Fig. 4.39 FRF of node A under S wave
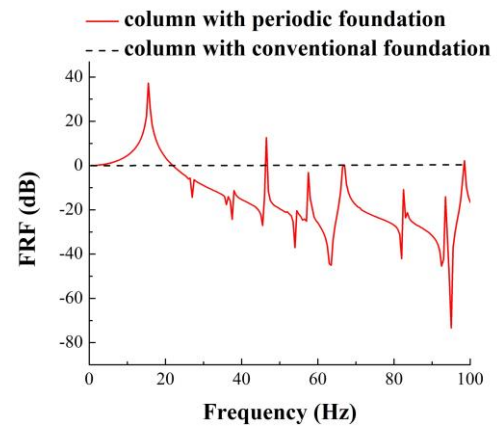
Fig. 4.40 FRF of node A under P wave

5   EXPERIMENTAL PROGRAM

In this chapter, the experimental program of 1D, 2D, and 3D periodic foundations are introduced in Section 5.1, Section 5.2, and Section 5.3, respectively. The material properties, test setup, and test procedures are illustrated.

5.1   Experimental Program of 1D Layered Periodic Foundations

5.1.1   1D layered periodic foundations specimen and test setup

The experimental program of 1D layered periodic foundation was performed in the National Center for Research on Earthquake Engineering (NCREE) in Taiwan. To test the 1D periodic foundation, two specimens were prepared. Specimen A was a three story steel frame. The steel frame was fixed on the shake table. A mass of 20kg was added for each floor. The cross-section of the columns in the steel frames was a square tube with a sectional dimension of 6 cm (breadth) $\times$ 6 cm (depth) $\times$ 0.32 cm (thickness); the cross-section of the beams was a rectangular tube with a sectional dimension of 3 cm (breadth) $\times$ 6 cm (depth) $\times$ 0.32 cm (thickness), and the thickness of the slabs was 0.3 cm. The height and plane dimensions of each story of the steel frames were 30 cm and 60 cm by 60 cm, respectively. Specimen B was a steel frame of the same design as that of Specimen A, but it was fixed on a 1D layered periodic bearing. The 1D periodic foundation was composed of three concrete layers and two rubber layers with the material properties as listed in Table 5.1. The thickness of each layer was 0.2 m, and the dimension of each layer was 1 m$\times$1 m. Fig. 5.1 shows the test specimens and the shake table. The concrete layers and rubber layers were bonded together by polyurethane (PU)

glue. The PU glue had enough resistance to tear forces to ensure that the concrete layer and rubber layer worked with the maximum test peak ground acceleration (PGA) input.
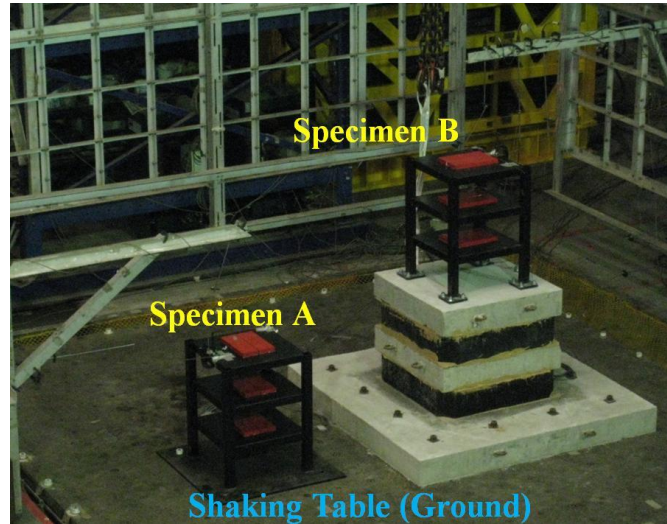
Fig. 5.1 Test setup for 1D periodic foundation

Table 5.1 Material constants of 1D layered periodic foundation tests

Materials	Young's Modulus	Poisson's Ratio	Density (kg/m^3)
Concrete	3.14×10^{10}Pa	0.330	2300
Rubber	5.8×10^{5}Pa	0.463	1300

The shake table shown in Fig. 5.1, with dimensions of 5m×5m, had the capability of six degrees of freedom (DOFs) to perform a ground motion in three directions. Specimen A and Specimen B were fixed on the shake table to have identical seismic input during the tests; the arrangement of sensors is shown in Fig. 5.2 and Fig. 5.3. The accelerometers, shown as A in Fig. 5.2 and Fig. 5.3, and the displacement transducers, Linear Variable Differential Transformers (LVDTs), shown as T in Fig. 5.2 and Fig. 5.3, were arranged on top of the frame, on each concrete layer, and on top of the shake table.
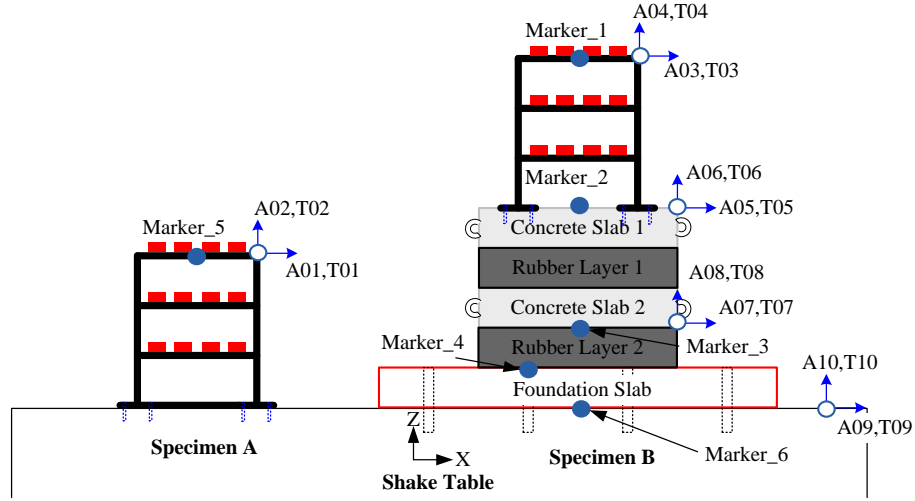
Fig. 5.2 Sensor arrangement for 1D periodic foundation test
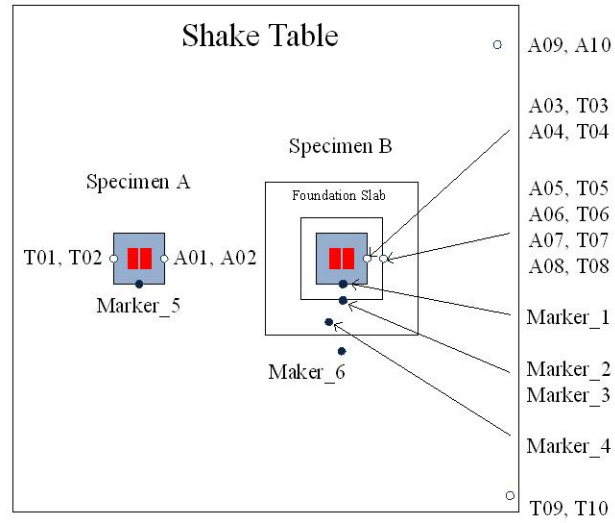
Fig. 5.3 Sensor arrangement for 1D periodic foundation test top view

5.1.2 Test procedure of 1D layered periodic foundations

Three different types of vibration tests were performed in the shake table test scheme; the ambient vibration test was conducted first. The main frequency of the recorded ambient vibration was about 50 Hz, which was assumed to be induced mainly by the shake table engine operation. The seismogram was obtained from the PEER Ground Database.[97] The 1975 Oroville was used as the input motion for the seismic

tests. The 1975 Oroville seismic record (station: 1051 Oroville Seismograph Station) was scaled to 50% of the original recorded peak ground acceleration values, and the 1975 Oroville seismic record (station: 1543 DWR Garage) was scaled to 200% of the original recorded peak ground acceleration values. Finally, a fixed sine wave with amplitude of 0.1cm and excitation frequency of 7 Hz was chosen for the harmonic test. As in the seismogram tests, the fixed sine wave was input in two directions, horizontal and vertical. A summary of the test steps is shown in Table 5.2.

Table 5.2 Experimental program of 1D periodic foundation

Test Name	Input Excitation	Control Algorithm	Input Direction	
Ambient vibration test	Ambient vibration	None	Varied	
Seismic test	1975 Oroville Seismogram	Acceleration	Biaxial	Horizontal
				Vertical
Sine wave	7 Hz	Displacement	Biaxial	Horizontal
				Vertical

5.2 Experimental Program of 2D Periodic Foundations

5.2.1 2D periodic foundation specimen materials

5.2.1.1 Concrete

The ready-mixed concrete with a 28-day compressive strength (f_c') of 41.3 MPa (6 ksi), which has a 0.2 m (8 in.) slump, was used in the test. The average concrete cylinder compressive strength is 44.1 MPa (6.4 ksi). According to the American Concrete Institute (ACI),[98] Young's modulus of the concrete can be obtained from Eq. (5-1).

$$E_c = 57000\sqrt{f_c'} \tag{5-1}$$

Young's modulus of concrete, therefore, was calculated to be 3.144×10^{10} Pa (4.56×10^6 psi). The density of the concrete was 2.3×10^3 kg/m^3.

5.2.1.2　Rubber

　　The stress-strain curve for the rubber used in the experiment was obtained by a series of tests according to the American Society for Testing of Materials (ASTM) D575-91.[99] The size of the specimen was 0.029 m (1.129 in.) diameter and 0.0127 m (0.5 in.) thickness, as shown in Fig. 5.4. Force was applied to produce a deflection rate of 0.0127±0.00254 m/min (0.5±0.1 in/min) until the specified deflection was reached; the force was released simultaneously, and the loading cycle was repeated for a second time. The force was applied for a third time until the specified deflection was reached again. The data from the third application were recorded to reach the stress-strain curve. The instrument of the test is shown in Fig. 5.5. The range of the linear variable differential transformer (LVDT) was 0.0508 m (2 in.), and the capacity of the load cell was 5 ton (10 kips).

　　Fig. 5.6 shows the average of the secant modulus at a strain of 0.1 is 0.57 MPa. The density of the super-soft neoprene (Duro10) was 1.196×10^3 kg/m^3.

Fig. 5.4 Soft neoprene (Duro10) test sample

Fig. 5.5 Rubber compressive test system

77
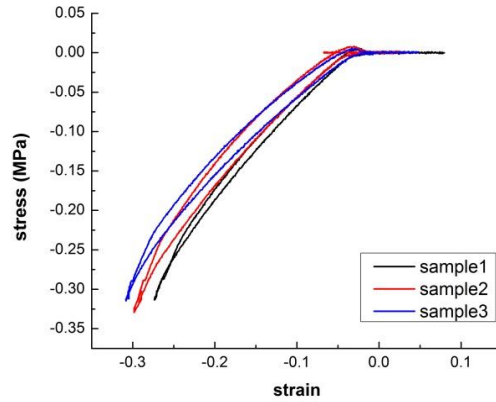
Fig. 5.6 Stress-strain relationship of rubber samples

5.2.1.3 Ductile Iron

Ductile iron was used for the core cylinders. The density of the ductile iron was 7.184×10^3 Kg/m^3. Young's modulus and Poisson's ratio were 1.65×10^{11} Pa and 0.275, respectively. These data are referred to as Ductile Iron Society.[100]

5.2.1.4 Unit Cell Component

A roll of super-soft rubber with a thickness of 0.0254 m (0.5 in.) was cut into small pieces with dimensions of 0.1 m (4 in.) × 1.6 m (64 in.). Parts of the inner and outer rubber layers were sanded into a large slope to make sure the connection between different layers was tight and smooth. Double-sided tape was used to ensure strong and smooth connections were made between different rubber layers. The iron core cylinder with super-soft rubber wrapping for the top and elevation views is shown in Fig. 5.7 and Fig. 5.8, respectively.
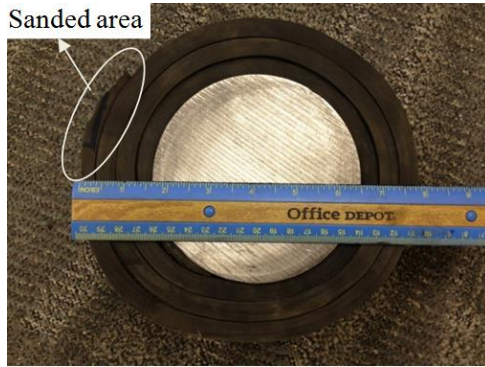
Fig. 5.7 Top view of iron core cylinder
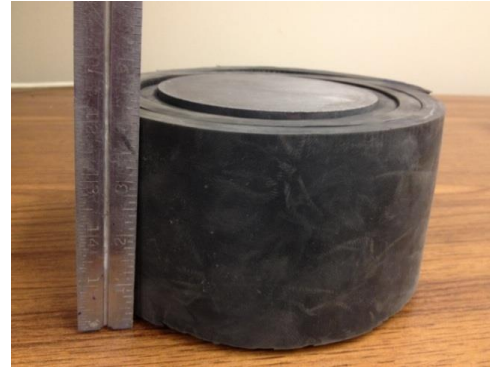
Fig. 5.8 Elevation view of iron core cylinder

5.2.2　2D periodic foundations specimen design

Two specimens were designed for the experimental program based on the most optimized parameters proposed, i.e., the steel frame with concrete foundation (Specimen C) and the periodic foundation (Specimen D), respectively. The models of the test specimens are shown in Fig. 5.9. specimens C and D were both supported by a reinforced concrete (RC) footing. The RC footing was 1.35 m×0.9 m with 0.3 m height. Specimen D shows the periodic foundation with a steel frame; it was cast simultaneously with the RC footing. The steel frame was 1m high and 0.5m wide; the column member was A36 steel, with a cross-section of S 3×5.7.[96] The connections between the column and the periodic foundation were bolted. The geometrical properties of the test specimens are listed in Table 5.3; Section 5.2.1 shows Table 5.4, which summarizes the material properties.
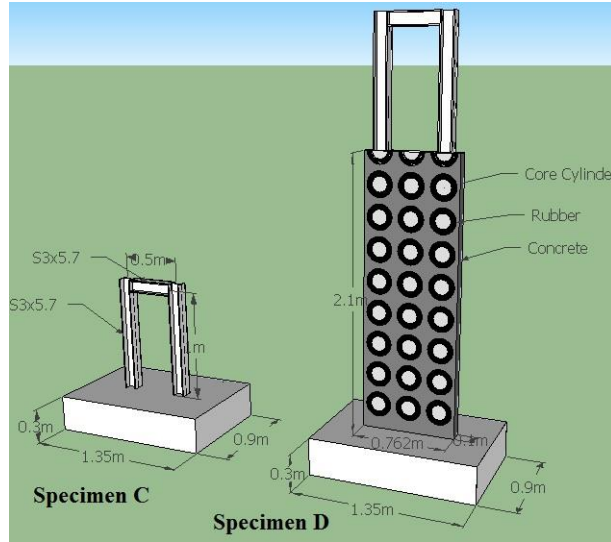
Fig. 5.9 Test specimens of 2D periodic foundation tests

Table 5.3 Geometric properties of one unit cell

Item	Material	Dimension
Core cylinder	Ductile cast iron	Diameter = 0.12 m.
Rubber coating	Supper soft rubber (Duro 10)	Outer diameter = 0.2 m.
Matrix	Reinforced Concrete	Length of unit cell (a) = 0.254 m

Table 5.4 Material properties of 2D periodic foundation specimens

Material	Density (kg/m3)	Young's Modulus (Pa)	Poisson's Ratio
Ductile cast iron	7.184×103	1.65×10^{11}	0.275
Supper soft rubber	1.196×103	5.7×10^{5}	0.463
Steel	7.85×103	2.05×10^{11}	0.28
Concrete	2.3×103	3.144×10^{10}	0.33

5.2.2.1 *Arrangement of Reinforcement*

The reinforcement arrangement in Specimen D is shown in Fig. 5.10 to Fig. 5.11. The rebar adopted in the periodic foundation was #2 (diameter of 6.35 mm), and the rebar in the RC base was #5 Grade 60 (diameter of 15.875 mm). Table 5.5 shows the reinforcement ratio in the 2D periodic foundation and the RC footing, respectively. In addition, four more steel rebars, i.e., #6 Grade 60 (diameter of 19.05 mm), were applied

to ensure enough stiffness at the connection of the periodic foundation and the RC footing. The rebar, with extra anchorage length to avoid premature cohesive failure under seismic loads, was embedded in the footing on both sides. The yield strength of #2 rebar used in the periodic foundations was 419.2 MPa; the ultimate strength was 562.6 MPa, and the elastic modulus was 187,496 MPa. There were two layers of rebar designed in the RC footing: For the reinforcement concrete footing, #5 Grade 60 rebar was used to resist soil reaction and punching shear during the field test. The minimum yield strength of Grade 60 rebar was 413.7 MPa, and the minimum ultimate strength of Grade 60 rebar was 620.5 MPa. The rebar in the RC footing of Specimen C was arranged in the same way as the rebar in the RC footing of Specimen D.

Table 5.5 Reinforcement ratio of 2D periodic foundation specimens

	Reinforcement Ratio in Longitudinal Direction ρ_l	Reinforcement Ratio in Transverse Direction ρ_t
2D Periodic Foundation (Specimen D)	0.00327	0.0023
RC Footing (Specimen C)	0.00359	0.0034
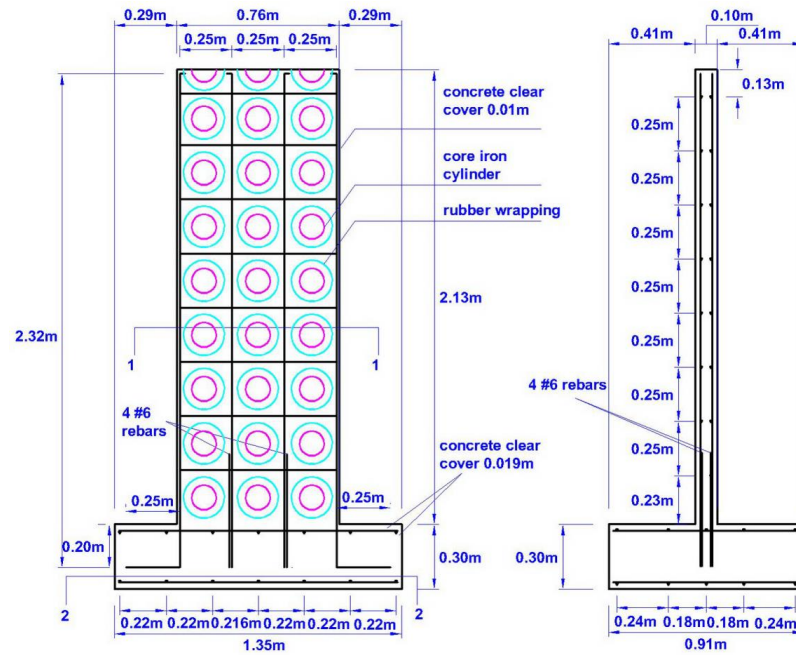
Fig. 5.10 Reinforcement of Specimen D
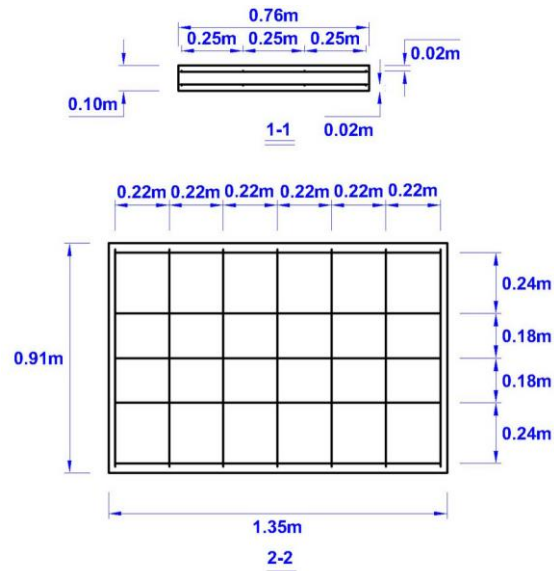
Fig. 5.11 Cross-section 2-2 of Specimen D

82

5.2.2.2 Upper Structure

The frame was composed of A 36 steel column and beam with a cross-section of S 3×5.7.[96] The central length of the column was 1m, and the central length of the beam was 0.5m. A 0.18 m×0.13 m×0.0127 m steel plate was welded to the bottom of each steel column. This same steel plate was welded to the cast iron as shown in Fig. 5.12. The two plates were fixed with four 0.0127 m (1/2 in.) diameter Grade 8 steel hex bolts with standard thread.

Detailed information of the connection between the beam and the column is shown in Fig. 5.12. A plate with dimensions of 0.18 m×0.03 m×0.00635 m was welded onto each end of the beam. The bolts used in the joint had 0.3125 m (5/16 in.) diameters with standard threads and 0.0254 m (1 in.) lengths. The columns and beams were connected together to make the steel frames. A 5.44kg mass was fixed at each connection point after the frame was assembled.
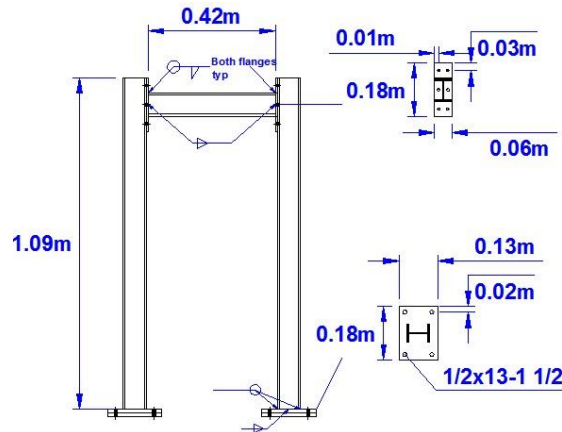
Fig. 5.12 Frame dimension and welding

5.2.2.3   Steel Frame with Reinforced Concrete Footing

The control specimen (Specimen C) with steel frame had the same RC footing as that of Specimen D. Fig. 5.13 shows the rebar cage in a formwork of RC footing. As shown in the figure, eight coupling nuts were embedded in the control specimen to connect the RC footing and the steel frame. The upper steel frame had the same size as that of Specimen D.
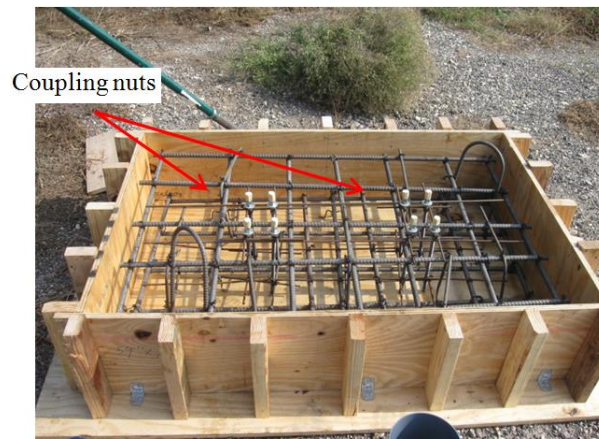
Fig. 5.13 Rebar cage of the RC footing

5.2.3   Formwork design

To ensure that the connection of the 2D periodic foundation and RC footing were rigid, making certain that the wave could be transferred completely, the 2D periodic foundation and RC footing were cast simultaneously. Another RC footing of the same size was made in parallel to support the control steel frame, as shown in Fig. 5.13. The formwork of 2D periodic foundation with unit cells and cage are shown in Fig. 5.14. The formwork of RC footing and 2D periodic foundation were leveled to make sure that the 2D periodic foundation was perpendicular to the RC footing. Fig. 5.15 shows that 0.1 m (4 in.) by 0.1 m (4 in.) pinewood with 0.4 m length was under every ductile iron core cylinder to ensure that the formwork was deformed to the allowable limitation.

Fig. 5.14 Unit cells in formwork of 2D periodic foundations

5.2.4 Test setup of 2D periodic foundations

5.2.4.1 S Wave Test Setup

5.2.4.1.1 Use of T-Rex Shaker

A tri-axial shaker named T-Rex at the University of Texas at Austin provided input seismic motions.[101] T-Rex is capable of shaking in the three directions, i.e., vertical, horizontal in-line, and horizontal cross-line. The horizontal in-line shaking (S wave) was used to generate horizontal vibrations along the X direction, as shown in Fig. 5.15.

T-Rex, which is based on vibroseis technology, was developed by Industrial Vehicles International, Inc. Vibroseis technology uses vehicle-mounted vibrators (commonly called "vibes") to drive coded seismic energy into the ground. The T-Rex is one of only a few large vibroseis vehicles that provide axis transformation among vertical, inline, and cross-line directions at the push of a button; it is 9.75 m long and 2.44 m wide with a total weight of 32 tons. T-Rex provides three vibration orientations, i.e., vertical, longitudinal, and transverse. The peak force in the vertical direction can reach 30 tons with a frequency of 12 Hz-180 Hz, while a peak force in the horizontal direction can reach up to 15 tons with a frequency range of 5 Hz-180 Hz.
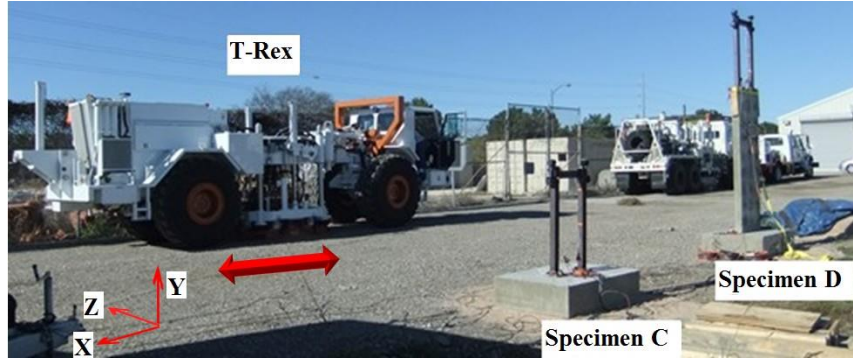
Fig. 5.15 Picture of field test setup using T-Rex
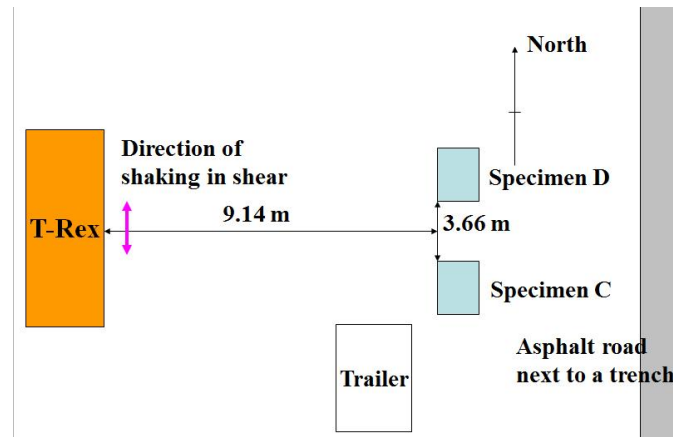
Fig. 5.16 Layout of test setup under S wave excitations using T-Rex

5.2.4.1.2 Use of Rattler Shaker

Rattler was used to generate an S wave to verify the effectiveness of the 2D periodic foundation. The 3D accelerometers were mounted on the top of the frame on Specimen C and Specimen D to record the accelerations. The positions of the accelerometers are marked in Fig. 5.17. The reinforced concrete footing with an upper steel frame is shown as Specimen C, and the periodic foundation with an upper steel frame is shown as Specimen D in Fig. 5.17. The input accelerations were provided by Rattler,[102] which is 8.7 m long and 2.6 m wide with a total weight of 24,176 kg. Rattler provides shear waves with a peak force of 133 kN and a frequency from 100 Hz to 5 Hz.

The positions of the specimens, Rattler, and trailer are shown in Fig. 5.18. Specimen D is located to the north of Specimen C. Rattler is parked with the driver side facing east, west of the two specimens, with a distance of 6.3m from the edge of the base plate to the edge of the specimens. The control room in the trailer is parked to the south of the two specimens. An I-beam connected the two specimens, and an angle steel beam reduced the rocking and rotating of the two foundations when the excitation accelerations were applied.
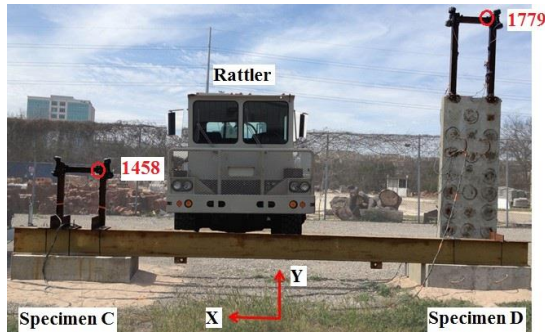
Fig. 5.17 Test setup for S wave excitations
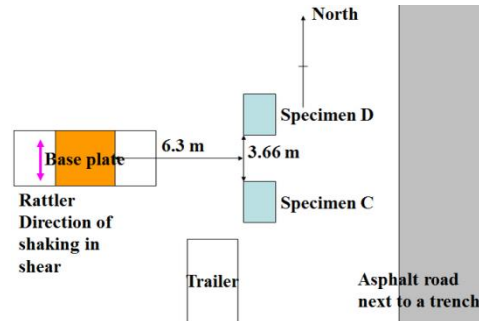
Fig. 5.18 Layout of test setup under S wave excitation using Rattler

5.2.4.2 P Wave Test Setup

The accelerometer arrangement is shown in Fig. 5.19. The four digital numbers in the figure are the gauge number of the accelerometers, i.e., 1782. Sensor 1782 was arranged on the concrete of the second row of unit cells from the top of the periodic foundation, and Sensor 1461 was in the middle of the iron cylinder of the second row of unit cells from the top. Sensor 1463 and Sensor 1784 were arranged on the seventh row from the top of the periodic foundation on the concrete and iron cylinder, respectively. Fig. 5.20 shows the layout of the test setup under P wave excitations using Thumper.

The test setup for P wave tests is shown in Fig. 5.21. The reinforced concrete footing with a steel frame is shown as specimen C. The periodic foundation with a steel

frame is shown as Specimen D. The shaker, Thumper,[103] was developed by Industrial Vehicles International, Inc. Thumper is a high frequency shaker with a capacity of up to 500 Hz. The peak force in the vertical direction can be up to 26.7 kN with a frequency in the range of 17 Hz to 225 Hz. The shaker provides two vibration orientations in both vertical and horizontal directions (360 degrees); its length is 8.23 m, and its width is 2.6 m, with a total weight of 11,258 kg.
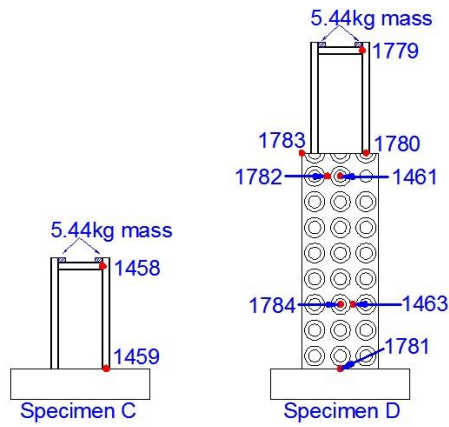
Fig. 5.19 Accelerometer arrangement for P wave tests
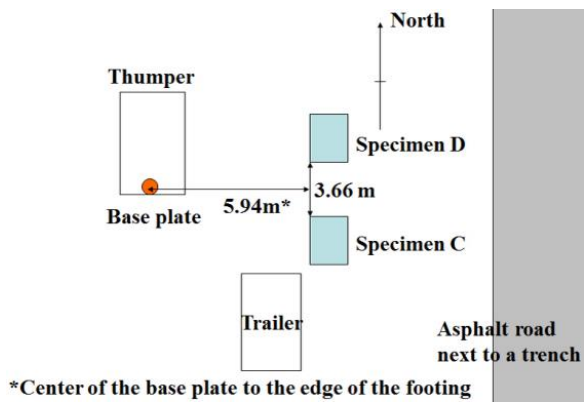
Fig. 5.20 Layout of test setup under P wave excitations
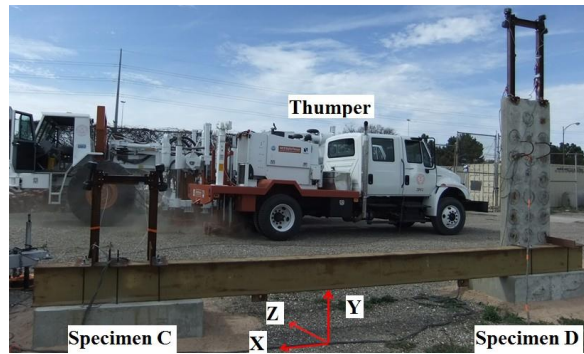
Fig. 5.21 Test setup for P wave excitations

5.2.5 Test procedure of 2D periodic foundations

Three different types of vibration tests were conducted. Stepped sine wave tests were first conducted to determine the frequency band gaps of the periodic foundation. A

stepped sine test is a test function provided by the Data Physics SignalCal 730 dynamic signal analyzer comparable to the scanning frequency analysis in FEM analyses. Fixed frequency sine waves from 100 Hz down to 5 Hz were applied to the test specimens according to the analytical results. Amplitudes and phases of each sensor at each frequency step were recorded. Based on the stepped sine wave test results, harmonic excitations with a fixed frequency were applied to the specimens. In the last step, a seismogram obtained from the Pacific Earthquake Engineering Research (PEER) Ground Database[97] was used as the input motion for the seismic tests. In the last two tests, the time histories of each sensor were recorded.

Table 5.6 Experimental program of 2D periodic foundation

Test Mode	Vibrator	Test Name	Input Excitation	Control Algorithm
S wave	T-Rex	Stepped sine test	100 Hz-40 Hz	Acceleration
		Fixed sine test	50 Hz with 10 cycles	Acceleration
		Seismic test	Bishop (Rnd Val) P0486/MCG-UP; Bishop (Rnd Val) P0486/MCG-360	Acceleration
S wave	Rattler	Stepped sine test	100 Hz-5 Hz	Acceleration
		Fixed sine test	46 Hz with 40 cycles; 20 Hz with 40 cycles	Acceleration
		Seismic test	BORAH.AS/HAU000; BORAH.AS/HAU090; LANDERS/LCN-UP	Acceleration
P wave	Thumper	Stepped sine test	100 Hz-5 Hz	Acceleration

		Fixed sine test	72.6 Hz with 40 cycles; 36 Hz with 40 cycles	Acceleration
		Seismic test	Bishop (Rnd Val) P0486/MCG-UP ; Bishop (Rnd Val) P0486/MCG-360	Acceleration

5.3   Experimental Program of 3D Periodic Foundations

5.3.1   3D periodic foundation specimen materials

5.3.1.1   Concrete

The ready mixed concrete had a 28-day compressive strength (f_c') of 6 ksi. Nine standard cylinders, with the dimension of 152 mm×305 mm (6 in.×12 in.) were cast along with the specimens. The cylinders were cured under the same conditions as the test specimens. The standard cylinders were under a moist environment covered by a plastic sheet for the first seven days. The cylinders were tested the same day as the field test was conducted. The average concrete cylinder compressive strength is 55.8 MPa (8.1 ksi); Young's modulus of concrete is calculated as 5.67×10^6 psi (4.0×10^{10} Pa); the density of the concrete is 2.3×10^3 kg/m^3.

5.3.1.2   Ultra-Soft Polyurethane

The Young's modulus of the wrapping rubber is an important parameter on the starting frequency band gap. According to the previous analysis in Section 4.3.1.1, a lower Young's modulus will provide a lower starting frequency and smaller bandwidth than the first band gap. To get a lower Young's modulus, ultra-soft polyurethane is used as the wrapping coat for the 3D periodic foundation specimen. This nonporous material,

also known as Sorbothane, has a fluid-like consistency and is durable and resilient enough to return to its original shape after repetitive compression.[105]

Fig. 5.22 shows the hardness, i.e., the resistance of a material to surface penetration, in different measuring scales. Durometer is the international standard for measuring the hardness of rubber, plastic, and most nonmetallic materials. Harder materials have more wear resistance, but they are also less flexible. As hardness decreases, the Young's modulus of the material decreases.[105] Note that the super-soft rubber used in the 2D periodic foundation has a hardness of Shore A 10.
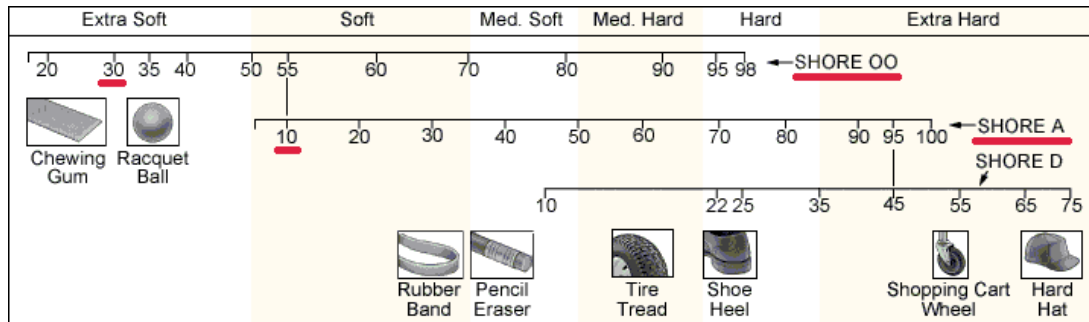
Fig. 5.22 Hardness comparison in different scales[105]

The stress-strain curve for the polyurethane used in the experiment was obtained by a series of tests according to American Society for Testing of Materials (ASTM) D575-91.[99] The size of the specimen was 34 mm diameter and 12.5 mm thickness. Force was applied to produce a deflection rate of 0.5 ± 0.1 in/min (12.7 ± 2.54 mm/min) until the specified deflection was reached. The force was released immediately and at the same rate. This loading cycle was repeated for a second time and a third time until the specified deflection was reached twice more. The data of the third application were recorded to find the stress-strain curve. The instrument of the test is shown in Fig. 5.23. The range of the linear variable differential transformer (LVDT) is 2 in. (50.8 mm), and the capacity of the load cell is 5 kips (22 kN).
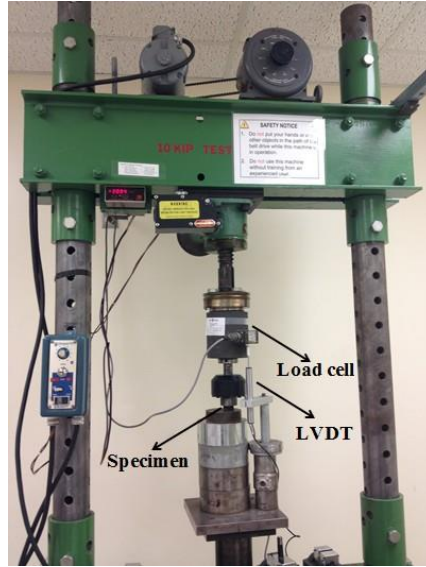
Fig. 5.23 Ultra-soft polyurethane compression test setup

Fig. 5.24 shows that the average of the secant modulus for Oo 30 at a strain of -0.1 is 0.1586 MPa is smaller than Oo40 and Oo 70 polyurethane and also smaller than the A 10 super-soft rubber used in the 2D periodic foundation. The density of the ultra-soft polyurethane is 1.277×10^3 kg/m^3. Tensile Strength of Oo 30 is 83 psi (0.572 MPa), and the mechanical properties of Oo 30 are valid in a temperature range of 0° to 160° F.
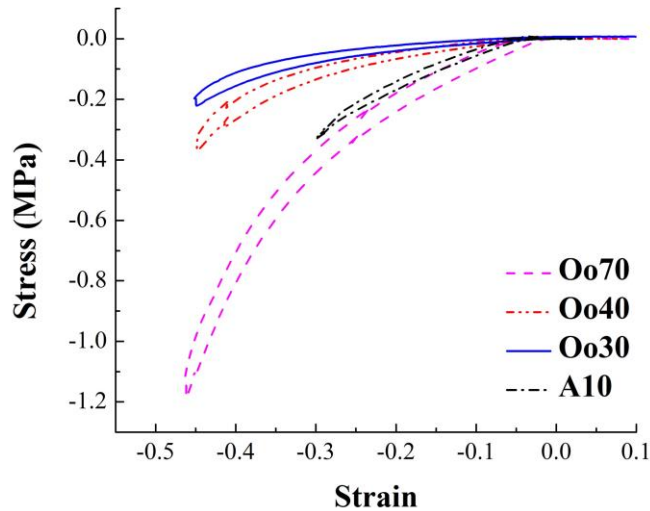
Fig. 5.24 Stress-strain relationship for polyurethane and rubber

5.3.1.3 Ductile Iron

Ductile iron was used for core cubes as shown in Fig. 5.25. The density of the ductile iron was 7.184×10^3 Kg/m^3. The Young's modulus and Poisson's ratio are 1.65×10^{11} Pa and 0.275, respectively. These data are referred to as Ductile Iron Society.[100]
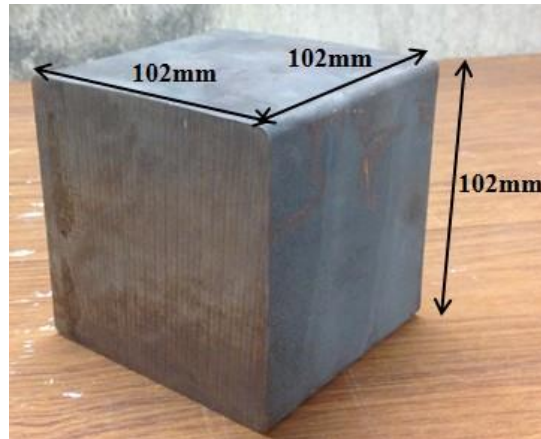
Fig. 5.25 Cast iron cube

5.3.1.4 Unit Cell Component

The polyurethane sheet with 25.4 mm thickness was cut into small pieces and pasted to the outside of the iron cube. The total thickness of the polyurethane layer was 50.8 mm. The side length of the iron core cube with polyurethane wrapping was 203 mm. Double-sided tapes were used to ensure strong and smooth connections were made between different rubber layers. The iron core cube with polyurethane wrapping is shown in Fig. 5.26.
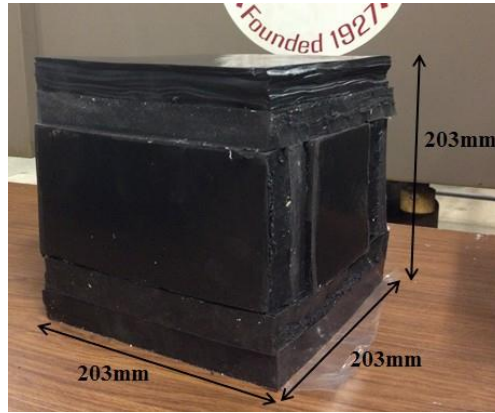
Fig. 5.26 Cast iron with polyurethane wrapping

5.3.2   3D periodic foundation specimen design

The 3D periodic foundation specimen was designed based on prior analysis, Section 4.3; Fig. 5.27 shows the dimensions of the test specimens. In Fig. 5.27, Specimen E is the control specimen, and Specimen F is the 3D periodic foundation with an upper structure. Both specimens E and F were supported by a reinforced concrete (RC) footing. The RC footing was 1.346 m×0.914 m, with a height of 0.305 m. Specimen F shows the periodic foundation with a steel column; it was cast simultaneously with the RC footing. The steel column was 1m high. The column member was A36 steel, with a cross-section of S 3×5.7.[96] The connections between column and the periodic foundation were bolted. Specimen E was a steel column that was fixed on the RC footing with the same size as the periodic foundation. The sizes of the steel column and the RC footing were the same as those of Specimen F; a 5.44kg mass was added to the top of the column to reduce the natural frequency of the superstructure. Table 5.8 is a summary of the material properties of the 3D periodic foundation according to Section 5.3.1
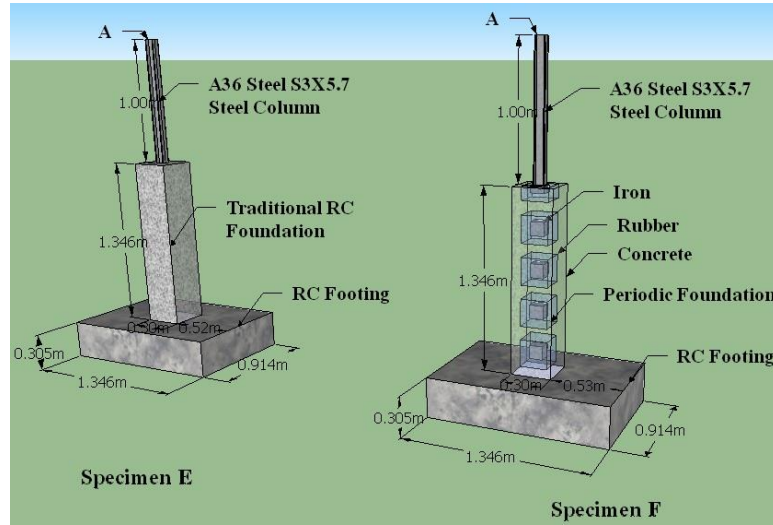
Fig. 5.27 Test specimens of 3D periodic foundation tests

Table 5.7 Parameters of one unit cell of 3D periodic foundation specimens

Part name	Material	Length of Side
Core cube	Ductile cast iron	b=102 mm
Polyurethane coating	Polyurethane (Oo 30)	b +2t=203 mm
Matrix	Concrete	a=305 mm

Table 5.8 Material properties of 3D periodic foundation

Material	Density (kg/m^3)	Young's Modulus (Pa)	Poisson's Ratio
Ductile cast iron	7.184×10^3	1.65×10^{11}	0.275
Polyurethane	1.277×10^3	1.586×10^5	0.463
Steel column	7.85×10^3	2.05×10^{11}	0.28
Concrete	2.3×10^3	4.0×10^{10}	0.33

5.3.3 Formwork design

To ensure that the connection of 3D periodic foundation and RC footing are rigid, thus ensuring the input S and P wave can be transferred completely, the 3D periodic foundation and RC footing were cast simultaneously. The dimensions of the formwork are represented in Fig. 5.28, which show that two pieces of 10 cm×10 cm pinewood were

used under the formwork of the periodic foundation to ensure that the formwork deformation was negligible.
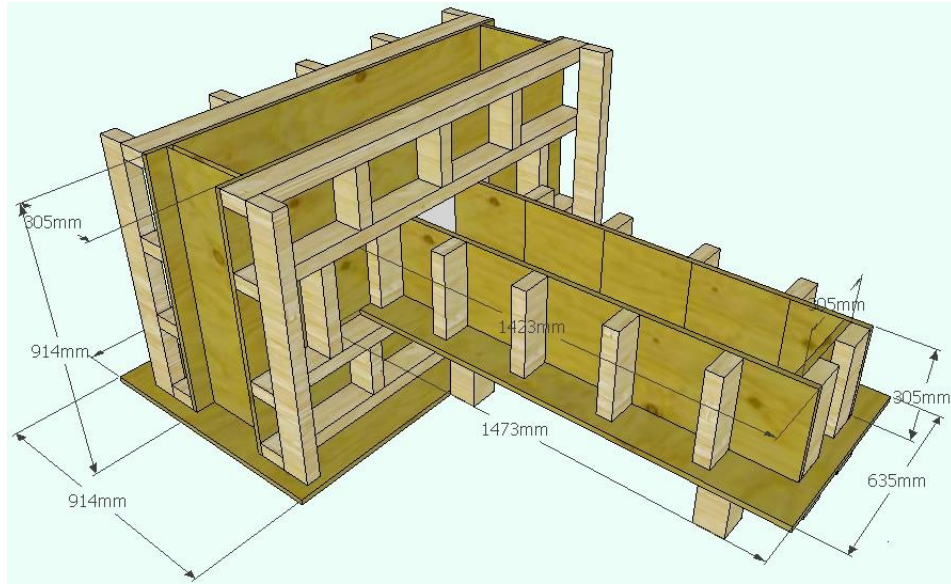
Fig. 5.28 Formwork design

Table 5.9 Reinforcement ratio of 3D periodic foundation specimens

	Reinforcement Ratio in Longitudinal Direction ρ_l	Reinforcement Ratio in Transverse Direction ρ_t
3D periodic foundation	0.00409	0.0025
RC footing	0.00359	0.0034

Section 4.3.1.2 shows the analysis of the geometric properties, listed in Table 5.7, of one unit cell of the 3D periodic foundation. The filling ratio, $f = \frac{b^3}{a^3}$, of the 3D periodic foundation was 0.296, and the ratio of the side length of the core cube to the thickness of polyurethane layer, $\beta = \frac{b}{t}$ is 2.

The yield strength of #2 rebar used in the periodic foundation was 60.8 ksi (419.2 MPa), the ultimate strength was 81.6 ksi (562.6 MPa), and the elastic modulus was 27,194 ksi (187,496 MPa).

Reinforcement concrete footing, #5 Grade 60 rebar, was used to resist soil reaction and punching shear during the field tests. The minimum yield strength of Grade 60 rebar is 60 ksi (413 MPa), and the minimum ultimate strength of Grade 60 rebar is 90 ksi (620 MPa).

The rebar arrangement in the specimen is shown in Fig. 5.29 to Fig. 5.31. The rebar in the periodic foundation was #2 (diameter of 0.25 in, 6.35 mm), and the rebar in the RC base was #5 Grade 60, (diameter of 0.625 in, 15.875 mm). Table 5.9 shows the reinforcement ratio in both 3D periodic foundation and RC footing. Four more #5 rebar with Grade 60 were installed to ensure the connection of the periodic foundation and the RC footing possessed adequate stiffness. The rebar was embedded in the footing to avoid premature cohesive failure under seismic loads. There were two layers of rebar designed in the RC footing.
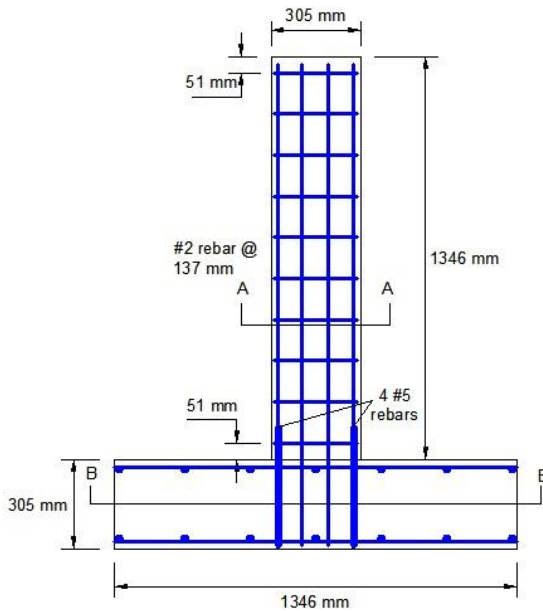
Fig. 5.29 Rebar design of the specimen   Fig. 5.30 Cross-section A-A of Specimen F
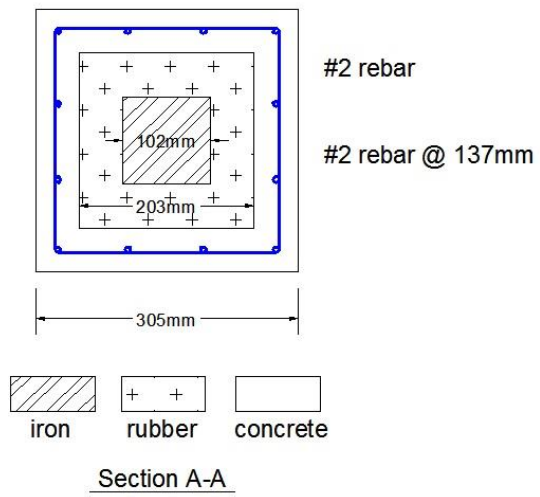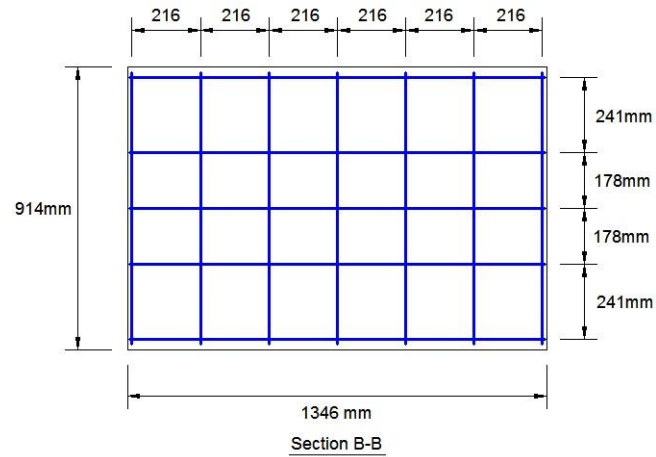
Fig. 5.31 Cross-section B-B of specimens E and F

5.3.4   Manufacture procedure

The detailed manufacture procedure is described in this section:

(1) Making formwork and rebar cages:

The rebar cages and formwork for the RC footing and the periodic foundation for specimens E and F were prepared in the Thomas T.C. Hsu Structural Research Laboratory at the University of Houston. Fig. 5.32 shows the completed formwork and rebar cages.

Fig. 5.32 Formwork and cages

(2) Assembly and level formwork:

The formwork was assembled on the test field before the concrete was cast. To ensure the footing and periodic foundation were perpendicular to each other, the two parts of the formwork were leveled while they were assembled, as shown in Fig. 5.33.

(3) Apply form release oil:

Before the rebar cages and the unit cell components were in place, the form release oil was applied inside the formwork so the formwork could be removed easily after the concrete of the specimens hardened. Fig. 5.34 shows the application of the form release oil.

Fig. 5.33 Level formworks

Fig. 5.34 Apply form release oil

(4) Arrange the unit cell components and rebar cages:

Fig. 5.35 shows the formwork and rebar cages of the control specimen (Specimen E) in the field. Fig. 5.36 shows that four coupling nuts were embedded in the control specimen to connect the control specimen and the steel column. The upper steel column was the same size as that of Specimen F.

Fig. 5.37 shows the formwork and rebar cages and the core cubes with polyurethane wrapping in the field. The steel column welded in the middle of the half core iron was fixed at the top of the 3D periodic foundation.

Fig. 5.35 Formwork and rebar cages for Specimen E

Fig. 5.36 Coupling nuts in control specimen

Fig. 5.37 Formwork and rebar cages for Specimen F

(5) Cast concrete:

The ready-mix concrete with compressive strength of 6 ksi (41.4 MPa), which has an 8 in. (203 mm) slump, was used in the specimens. After proper vibration, the top surfaces of the specimens were made smooth and even. Fig. 5.38 shows the procedure for casting the concrete.

Fig. 5.38 Casting specimens

(6) Curing the concrete:

The specimens were covered by burlap and plastic sheets after casting to maintain humidity, as shown in Fig. 5.39. After twelve hours of casting, the specimens were watered. Then in the next seven days, the specimens were watered every twelve hours.

Fig. 5.39 Curing of concrete

5.3.5   Test setup of 3D periodic foundations

5.3.5.1   S Wave Test Setup

5.3.5.1.1   Use of Rattler shaker

Three-dimensional accelerometers were mounted on 3D test specimens to obtain acceleration in two orthogonal directions, horizontal and vertical. The RC footing with an upper steel column is shown as Specimen E, and the periodic foundation with an upper steel column is shown as Specimen F in Fig. 5.40. The position and the directions of the accelerometers are specified in Fig. 5.40. The four digital numbers in the figure are the sensor number of the accelerometers, such as Sensor 1784. For Specimen F, Sensor 1463 was at the top surface of the RC footing, i.e., the bottom of the periodic foundation. Sensor 1779 was arranged on the concrete of the third row of unit cells from the bottom of the periodic foundation, and Sensor 1780 was at the top of the periodic foundation on the concrete. sensors 1783 and 1782 were arranged on the top and bottom of the steel column, respectively. The sensors in Specimen E were on the same levels as those of Specimen F. The positions of the specimens, the Rattler, and the trailer are shown in Fig. 5.41 and Fig. 5.42 and are described later in this section. Specimen F is located at the north of Specimen E. The input accelerations were provided by the Rattler,[102] as shown in Fig. 5.41, and is 8.7 m long and 2.6 m wide with a total weight of 24,176 kg. The Rattler provided shear waves with a peak force of 133 kN and a frequency of from 100 Hz to 5 Hz. The Rattler was parked with the driver facing east, on the west of the two specimens, with a distance of 6.4 m from the edge of the base plate to the edge of the specimens. The control room in the trailer was parked on the south of the two specimens. An I-beam and angle steel beam connected the two specimens to reduce the rocking and rotating of the two foundations when excitation acceleration were applied to them.
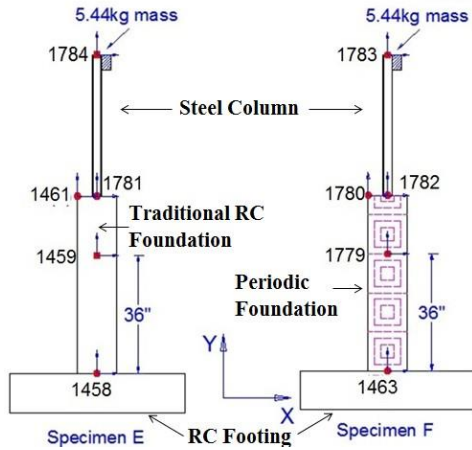
Fig. 5.40 Accelerometers arrangement of specimens E and F
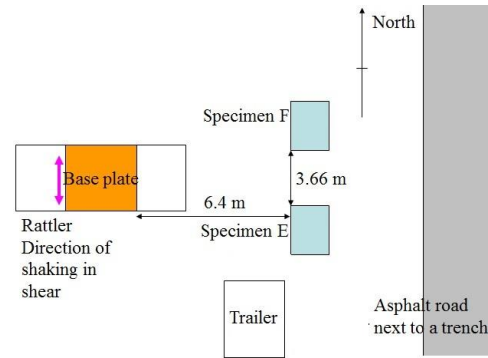
Fig. 5.41 Layout of test setup under S wave excitation

Fig. 5.42 Test setup for S wave excitation

5.3.5.1.2 Use of T-Rex shaker

A tri-axial shaker at the University of Texas at Austin named T-Rex[101] provided the input seismic motions for additional tests to be performed on the periodic foundations. T-Rex is capable of shaking in the three directions, i.e., vertical, horizontal in-line, and horizontal cross-line. The horizontal in-line shaking (S wave) was used to generate horizontal vibrations along the X direction, as shown in Fig. 5.43. Fig. 5.44 is the map of the test setup. The T-Rex was parked with the driver facing south, on the west

of the two specimens, with a distance of 7.9 m from the edge of the base plate to the edge of the specimens. The control room in the trailer was parked on the south of the two specimens. The two specimens were connected by an I-beam and an angle steel beam to reduce the rocking and rotating of the two foundations when excitation accelerations were applied; this is the same as the test setup in 5.3.5.1.1. The position and the directions of the accelerometers are specified in Fig. 5.40. Since T-Rex can provide both the S wave and P wave, the test setup of the P wave using T-Rex is the same as the setup described in this section.
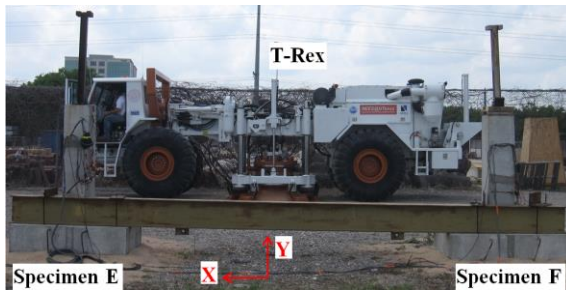
Fig. 5.43 Picture of field test setup using T-Rex
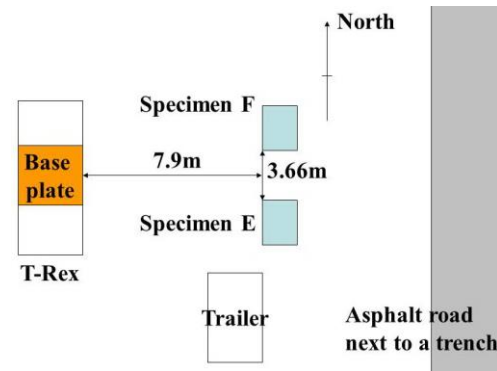
Fig. 5.44 Layout of test setup

5.3.5.2 P Wave Test Setup

5.3.5.2.1 Use of Raptor shaker

The accelerometer arrangement for the P wave test was the same as shown in Fig. 5.40. Fig. 5.45 shows a plan of the test setup map for P mode tests. Unlike the test setup for S wave excitations, the shaker for the P wave excitation, called the Raptor, was parked with the driver side facing north, and the distance from the edge of the base plate to the two specimens was 9.1 m. Fig. 5.46 shows the test setup under P wave excitations. The conventional reinforced concrete foundation with a steel column, shown as specimen

E, is to the south of the periodic foundation with a steel column shown as Specimen F. The Raptor[104] shaker provides a vibration orientation in a vertical direction. It is 9.8 m long and 2.4 m wide with a total weight of 17,236 kg.
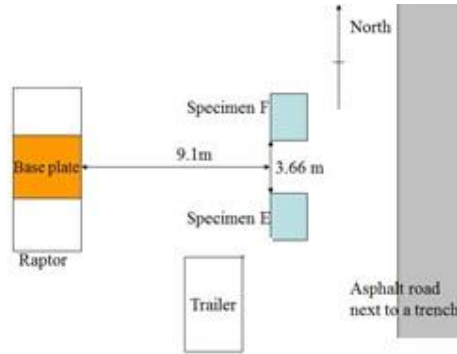
Fig. 5.45 Layout of test setup under P wave excitation

Fig. 5.46 Test setup for P wave excitation

5.3.6 Test procedure of 3D periodic foundations

The specimens were tested by different vibrators, i.e., Rattler, T-Rex, and Raptor. Rattler was used for the S wave test, and Raptor was used for P wave tests. T-Rex was used for both S and P wave input, and every test was conducted twice using different excitation voltages, i.e., 2V and 4.5V using T-Rex to find the effects of the amplitude of input waves.

For each vibrator and test mode, three different types of tests were conducted. Stepped sine tests were first conducted to determine the frequency band gaps of the periodic foundation. A stepped sine test is a test function provided by the Data Physics SignalCal 730 dynamic signal analyzer. Fixed frequency sine waves from 100 Hz down to 5 Hz were applied to the test specimens in one-hundred steps. Amplitudes of the accelerometers on top of the column at each frequency step were recorded. Next, based on the results of the stepped sine tests, harmonic excitations with a fixed frequency

within a frequency band gap were applied to the specimens. In the last step, a seismogram obtained from the Pacific Earthquake Engineering Research (PEER) Ground Database was used as the input motion for the seismic tests; in the last two tests, time histories of each sensor were recorded. Table 5.10 shows the test algorithm of the 3D periodic foundation.

Table 5.10 Experimental program of 3D periodic foundation

Test Mode	Vibrator	Test Name	Input Excitation	Control Algorithm
S wave	Rattler	Stepped sine test	100 Hz-5 Hz	Acceleration
		Fixed sine test	35.1 Hz with 40 cycles; 52 Hz with 40 cycles	Acceleration
		Seismic test	BORAH.AS/HAU090	Acceleration
S wave	T-Rex	Stepped sine test	100 Hz-5 Hz with 2V and 4.5V excitations	Acceleration
		Fixed sine test	40 cycles 43.7 Hz with 2V and 4.5V excitations	Acceleration
		Seismic test	BORAH.AS/HAU000 2V and 4.5V excitations	Acceleration
P wave	Raptor	Stepped sine test	100 Hz-5 Hz	Acceleration
		Fixed sine test	21.2 Hz with 40 cycles; 38.9 Hz with 40 cycles	Acceleration
		Seismic test	BORAH.AS/HAU090;	Acceleration
P wave	T-Rex	Stepped sine test	100 Hz-5 Hz with 2V and 4.5V excitations	Acceleration

		Fixed sine test	21.2 Hz with 40 cycles and 2V and 4.5V excitations	Acceleration
		Seismic test	BORAH.AS/HAU000 with 2V and 4.5V excitations	Acceleration

6 EXPERIMENTAL RESULTS

6.1 Experimental Results of 1D Layered Periodic Foundations

Test results for three test steps are illustrated in this section, i.e., ambient vibration, the seismic test, and the harmonic test. The shaking table that was used had six degree of freedom to simulate earthquake motion in three directions. The tested waves were applied in both horizontal and vertical directions for the seismic test.

6.1.1 Ambient vibration test results

Fig. 6.1 shows acceleration in the horizontal direction on top of the frame with ambient vibration, caused by the machine with a main frequency of 50 Hz, which is located in the third attenuation zone as shown in Fig. 4.18. The acceleration on top of the frame without a foundation (Specimen A) in the horizontal direction is shown as a dashed gray curve in Fig. 6.1. The red solid curve is the acceleration on top of the frame with a 1D layered periodic foundation in the horizontal direction. The peak acceleration on top of the frame with a 1D layered periodic foundation (Specimen B) is reduced significantly compared to that of the frame without the foundation (Specimen A).
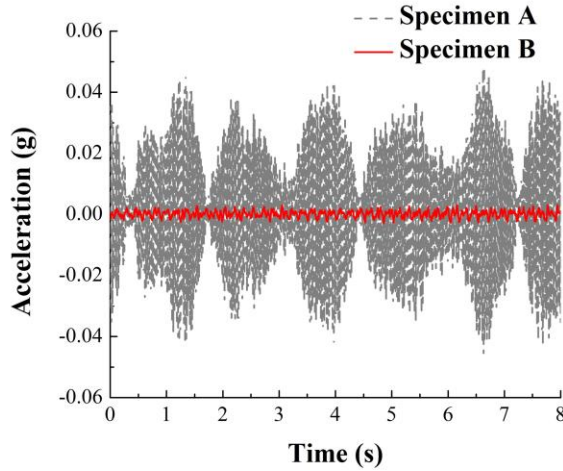
Fig. 6.1 Dynamic responses induced by ambient vibration

6.1.2 Seismic test results

The 1975 Oroville seismogram obtained from the PEER Ground Database[97] was used as the input motion for the shaking table test. The OROVILLE/A-ORV037 from the 1051 Oroville Seismograph Station was first applied in the horizontal and vertical directions. The nominal peak ground acceleration (PGA) was scaled to 50% of the recorded PGA, 0.046g. Fig. 6.2 shows the original time history of OROVILLE/A-ORV037 and Fig. 6.3 shows the Fourier Transform of the frequency domain OROVILLE/A-ORV037. The main frequency of the OROVILLE/A-ORV037 is 18.1 Hz, which is located in the first attenuation zone of the S wave input. Fig. 6.4 shows vertical relative displacement at the top of the frames under OROVILLE/A-ORV037. The dashed gray curve is the relative vertical displacement on top of the frame of Specimen A of the shake table. The peak relative displacement is 0.433 mm. The solid red curve shows the relative vertical displacement on top of the frame of the Specimen B shake table. The peak relative displacement is 0.266 mm. The peak relative vertical displacement of

110

Specimen B is reduced by as much as 43.3%, compared to that of the frame without the periodic foundation of Specimen A.
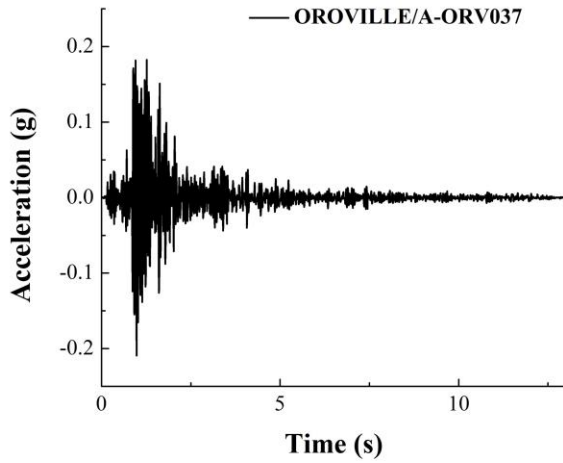
Fig. 6.2 OROVILLE/A-ORV037 in time domain
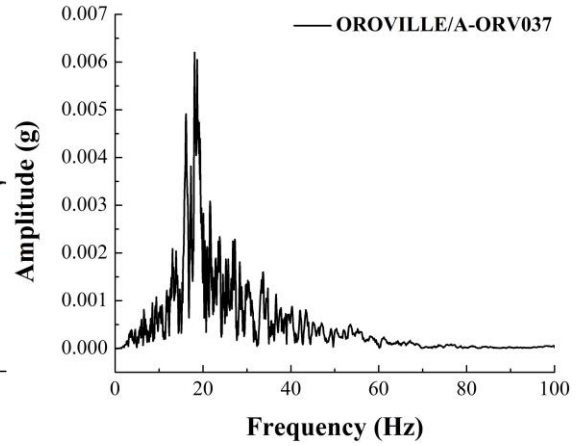
Fig. 6.3 OROVILLE/A-ORV037 in frequency domain
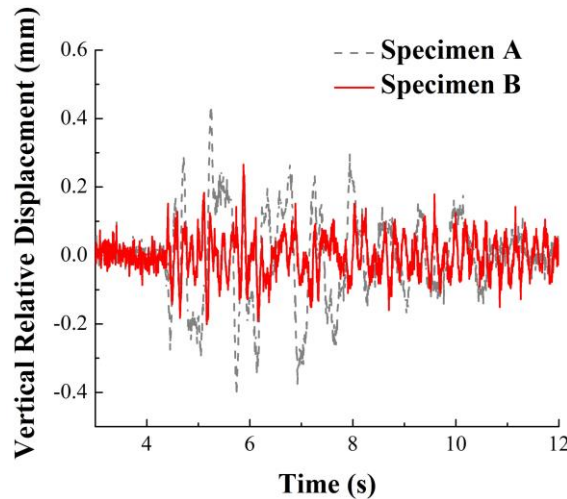
Fig. 6.4 Vertical relative displacement at the top of the frames under OROVILLE/A-ORV037

The 1975 Oroville seismogram record, i.e., OROVILLE/D-DWR180 and OROVILLE/D-DWRDWN from the DWR garage station were applied to the specimen in the horizontal and vertical directions. The main frequency of the seismogram was 18.1 Hz, and the PGA was scale to 200% of the original PGA. Fig. 6.5 shows the acceleration on top of the frame in the horizontal direction. The dashed gray curve is the acceleration

111

on top of the frame without a foundation, and the solid red curve is the horizontal acceleration on top of the frame with a 1D layered periodic foundation. The peak acceleration of Specimen A is 1.11g, and the peak acceleration of Specimen B is 0.48g. The peak acceleration of Specimen B is 43.2% that of Specimen A.

Transverse and longitudinal band gaps are present in the periodic foundation, as was discussed previously, so the vertical displacement responses of the specimens emphasizes that the periodic foundation also has the potential to isolate the vertical vibration. Fig. 6.6 shows in Specimen B the reduction of the vertical displacement in the frame on the periodic foundation. The gray dashed curve is the vertical displacement on top of the frame of Specimen A, and the red solid curve is that of Specimen B. The peak red displacement of Specimen B is 1.05 mm, which is smaller than that of Specimen A. These test results are promising and support the theory that the periodic foundation can serve as a multi-dimensional base isolation.
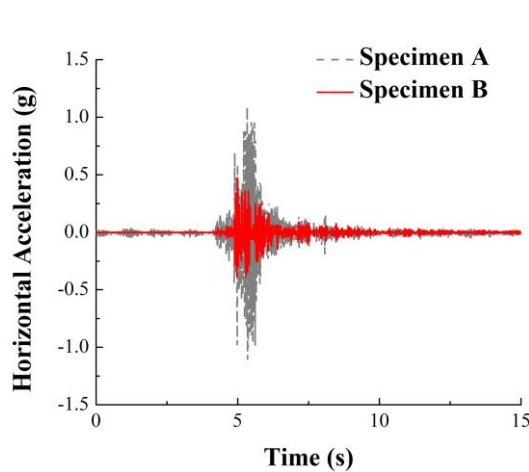
Fig. 6.5 Horizontal acceleration responses at the top of the frames under 1975 Oroville earthquake
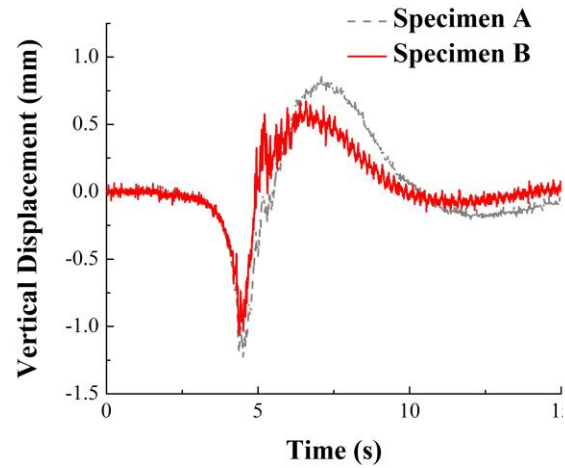
Fig. 6.6 Vertical displacement time history at the top of the frames under 1975 Oroville earthquake

The test result indicates that the periodic foundation is capable of being an effective filter for isolating the ambient vibration in which the frequency contents fall into the desired band gap.

6.1.3 Harmonic test results

The 7 Hz sine wave displacements were applied to the two specimens to test the response of the peridoic foundation with an excitation frequency falling out of the attenuation zone. The horizontal accelerations of the two specimens are shown in Fig. 6.7. The dashed gray curve represents the accelerations on top of the steel frame without the foundation of Specimen A with a peak acceleration of 0.46g. The solid red curve represents accelerations on top of the steel frame of Specimen B with an amplitude of 0.53g. The dashed gray curve has an amplitude of 0.46g, which is the accelerations on top of the steel frame of Specimen A. This result indicates that, although the periodic foundation is not effective in attenuating vibrations when the excitation frequency is outside the band gaps, which coincides with the numerical prediction, it does not lead to a significantly worse response compared to the fixed foundation.
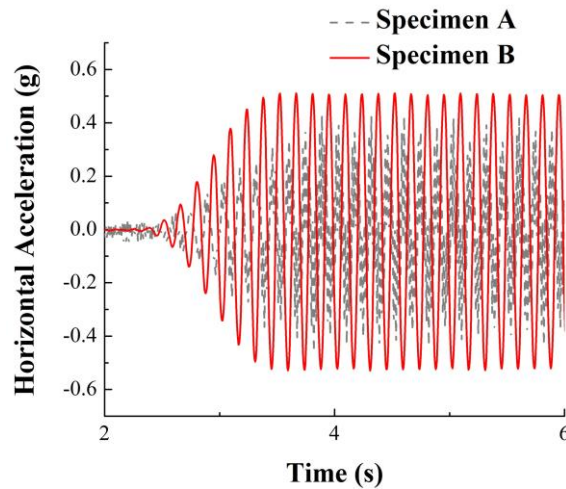
Fig. 6.7 Horizontal acceleration on top of the frame with harmonic excitation

6.2   Experimental Results of 2D Periodic Foundations

The dynamic responses of the 2D periodic foundation tests are covered in this section. The test results with S wave excitations are presented first. Two vibrators, T-Rex and Rattler, were used to input S waves. Then, the vibrator called Thumper, was used to apply the P wave to the specimens; the test results are illustrated. For each vibrator, stepped sine wave, fixed sine wave, and seismic wave, tests were performed.

6.2.1   S wave test results of 2D periodic foundations

6.2.1.1   Use of T-Rex Shaker

6.2.1.1.1 Stepped sine S wave results

Specimen C is the steel frame with RC footing, and Specimen D is the steel frame with 2D periodic foundations, as was introduced in Section 5.2.4.1.1. Fig. 6.8 shows acceleration in the X direction measured on top of the two steel frames from the stepped sine wave tests. The steel frame on Specimen C, shown in the figure, experienced a higher level of acceleration at most frequencies, especially at 50 Hz. Although not shown here, both foundations were subjected to a similar level of shaking. To eliminate possible differences of shaking levels between the two foundations, the acceleration was normalized on top of the steel frame by the acceleration measured on the foundations for both specimens C and D. Fig. 6.9 shows the amplitudes of the transfer functions for both specimens; the transfer function is the ratio between the acceleration measured on the top of the frame to that measured on the concrete foundation. When the amplitudes of the transfer functions of Specimen D are less than those of Specimen C, seismic motions are attenuated by the periodic foundation. Fig. 6.9 shows that the band gaps are in the

frequency ranges of 40 Hz-84 Hz and 86 Hz-93 Hz. The ratio of the transfer function from Specimen D to the transfer function from Specimen C are plotted in Fig. 6.10 to illustrate the test results The band gaps occur where the ratio is less than 1, i.e., below the black dashed line shown in Fig. 6.10.
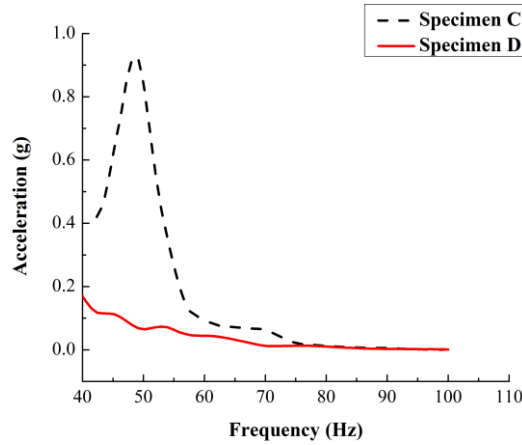
Fig. 6.8 Accelerations at the top of specimens C and D

Fig. 6.9 Transfer function for specimens C and D

6.2.1.1.2 Fixed sine S wave results

The frequency band gaps of the periodic foundation with a steel frame were found to be 40 Hz-84 Hz and 86 Hz-93 Hz, as can be seen from the stepped sine wave tests. A single frequency sinusoidal wave was applied to the specimens within the range of the band gaps, i.e., 50 Hz to verify the effects of the frequency band gaps. Fig. 6.11 shows the accelerations in the X direction on the top of the frame under a sine wave with a frequency of 50 Hz. The dashed black curve shows the acceleration response on top of the steel frame on a concrete foundation, Specimen C, while the red curve is the acceleration at the top of the frame on a periodic foundation, Specimen D. The peak acceleration of Specimen C is 0.91g, and the peak acceleration of Specimen D is 0.26g. The frame on the periodic foundation shows that the peak acceleration was reduced to 28.6% of the peak acceleration on the frame without the periodic foundation.

115
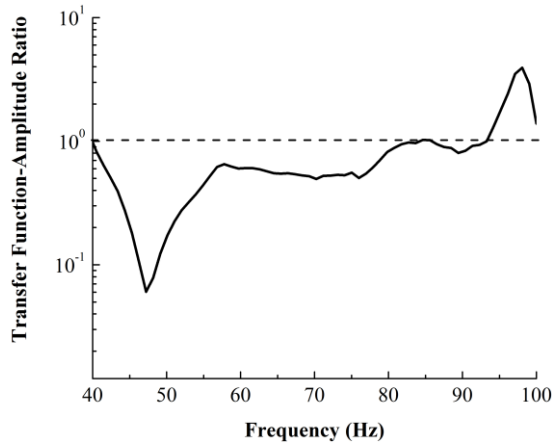
Fig. 6.10 Ratio of transfer function
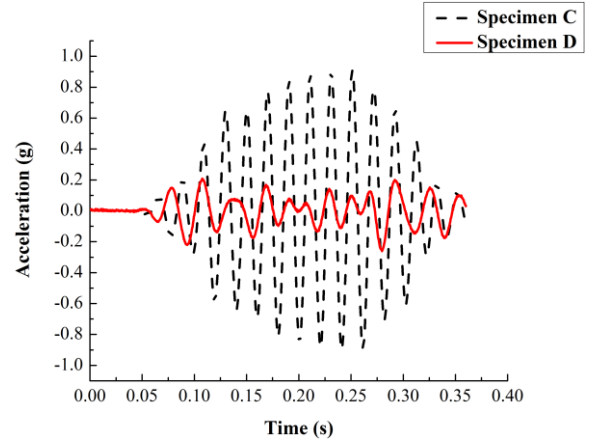
Fig. 6.11 Acceleration in X direction on the top of the frame under a sine wave of 50Hz

6.2.1.1.3 Seismic S wave results

Modified seismograms were used to verify the effects of the frequency band gap. Two seismic records from the PEER Ground Database[97] were used in the field tests. Both seismic records were modified so that main frequency and band gaps matched at 50 Hz.

Fig. 6.12 shows the horizontal acceleration time-based histories of both specimens at the top of the steel frames under the excitation of the modified Bishop (Rnd Val) P0486/MCG-UP (1984/11/23). The gray dashed curve shows the acceleration on top of of the Specimen C frame, with a peak acceleration of 0.73g, and the red solid curve shows acceleration in the horizontal direction of Specimen D, with peak acceleration of 0.3g. The peak acceleration in the X direction for the frame on the periodic foundation, Specimen D, was found to be reduced by as much as 58.9% as compared to that of the frame without the periodic foundation, Specimen C. The responses of the two specimens under the modified seismogram, Bishop (Rnd Val) P0486/MCG-360 (1984/11/23), are shown in Fig. 6.13. The peak acceleration of Specimen C, shown as a gray dashed curve,

is 0.63, and the peak acceleration of Specimen D is 0.43g, shown as a red solid curve. The peak acceleration on the top of the frame was reduced by 31.7%, as compared to the specimen without the periodic foundation.

The reduction in Fig. 6.13 is seen to be less than that in Fig. 6.12; the cause of this phenomenon owes to the frequency of the seismogram. Fig. 6.14 and Fig. 6.15 represent the input seismogram in the frequency domain; although the main frequency of the two seismograms was 50 Hz, when Fig. 6.14 and Fig. 6.15 are compared, the seismogram in Fig. 6.15 shows it to have more waves, and with frequencies that do not fall in the band gaps, than does Fig. 6.14. Overall, the test results indicate that the periodic foundation is capable of providing effective isolations for the vibrations falling into the designed band gap.
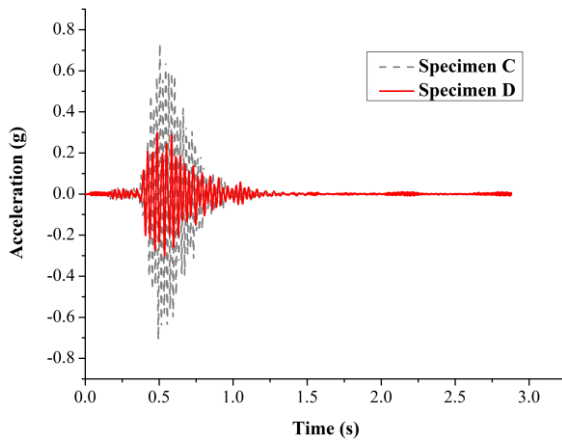
Fig. 6.12 Acceleration in X direction on the top of the frame under modified Bishop (Rnd Val) P0486/MCG-UP with the main frequency of 50Hz
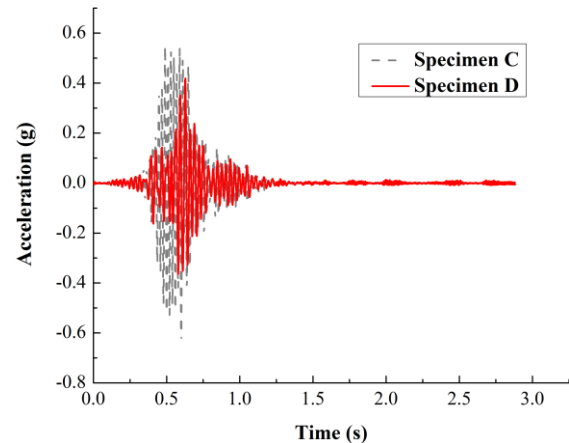
Fig. 6.13 Acceleration in X direction on the top of the frame under modified Bishop (Rnd Val) P0486/MCG-360 with the main frequency of 50Hz
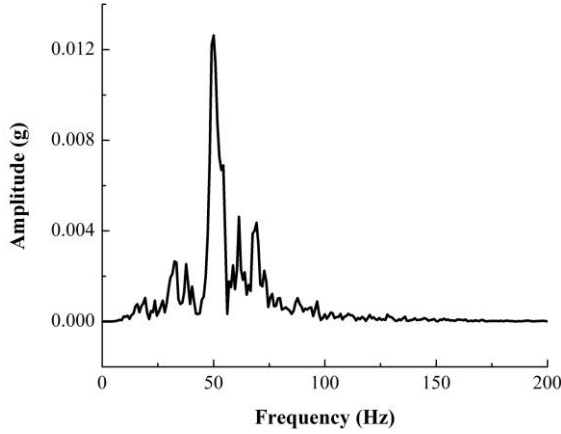
Fig. 6.14 Modified Bishop (Rnd Val)
P0486/MCG-UP in frequency domain
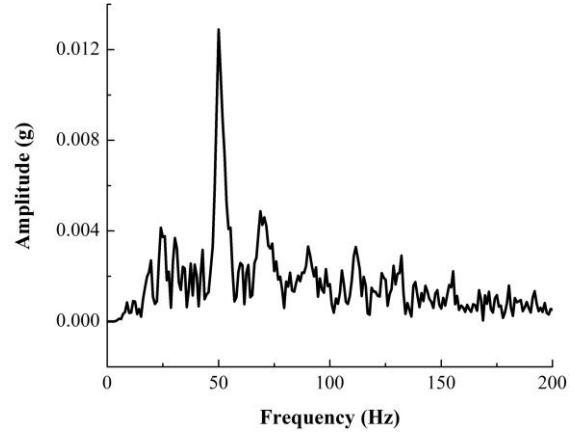
Fig. 6.15 Modified Bishop (Rnd Val)
P0486/MCG-360 in frequency domain

6.2.1.2   Use of Rattler Shaker

6.2.1.2.1   Stepped sine S wave results
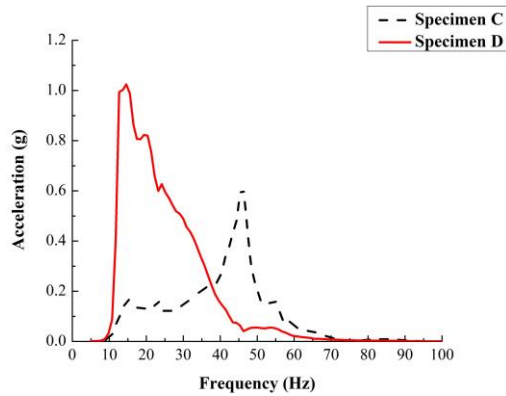
Fig. 6.16 Accelerations in X direction at
the top of each of both specimens C and D
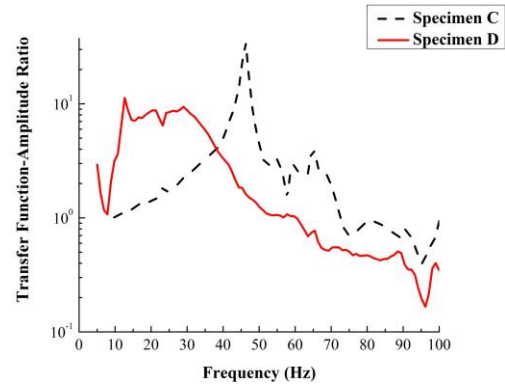
Fig. 6.17 Transfer function for both
specimens C and D

Fig. 6.16 shows acceleration in the X direction measured at the top of each of the

two steel frames, and it shows further that the steel frame on Specimen C experienced a

greater level of acceleration frequency, higher than 38 Hz, especially at 46 Hz. The

acceleration at the top of each of the two steel frames was normalized by the acceleration

measured on the corresponding foundations to eliminate possible differences of shaking

118

levels between the two foundations. Fig. 6.17 shows the amplitude of the transfer functions of both specimens. When the amplitude of the transfer functions of Specimen D was less than those of Specimen C, seismic motions were mitigated by the periodic foundation. Fig. 6.17 shows that the band gaps were in the frequency range of 38 Hz to 100 Hz. The ratio of the transfer function of Specimen D to Specimen C is plotted in Fig. 6.18. The frequency band gaps occur where the ratio is smaller than 1, which is below the black dash line, as shown in Fig. 6.18.

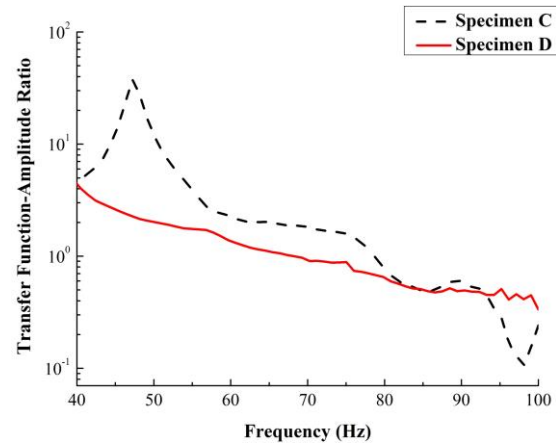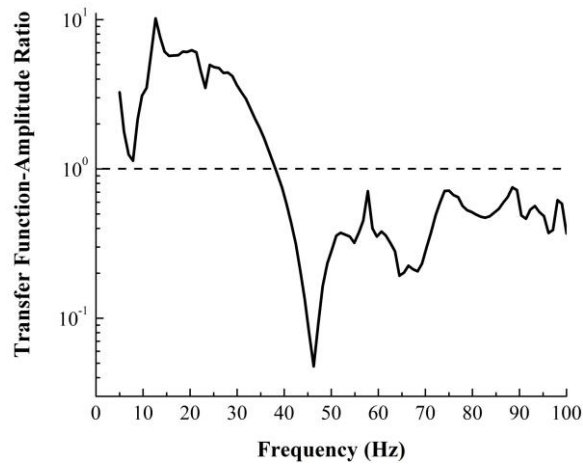Fig. 6.18 Ratio of transfer function

6.2.1.2.2 Fixed sine S wave results

The frequency band gaps of the periodic foundation with a steel frame were found to be in the range of 38 Hz to 100 Hz, as shown in results of the stepped sine wave tests. A fixed-frequency sinusoidal wave was applied to the specimens within the range of the band gaps, 46 Hz with 40 cycles, to verify the effects of the frequency band gaps. Fig. 6.19 shows acceleration in the X direction on the top of the frame under the sine wave with a frequency of 46 Hz. The dashed curve is the acceleration response on the top of the steel frame on a concrete foundation, Specimen C, while the red curve is the

119

acceleration response at the top of the frame on a periodic foundation, Specimen D. At the beginning of acceleration input, both specimens C and D were subjected to the transient effect until they reached the steady state; the same effect happened when the input excitations stopped. The frame on the periodic foundation receiving the transient effect at the beginning of the tests had peak acceleration reduced to 71.5% of peak acceleration on the frame without the periodic foundation. In the steady state, however, the peak acceleration of Specimen C in steady state was 0.6g and that of Specimen D was 0.1g. The peak acceleration of Specimen D was reduced to 17% of peak acceleration on the steel frame in Specimen C.
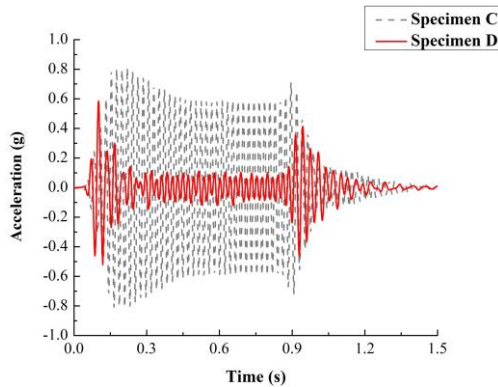
Fig. 6.19 Acceleration in X direction on the top of the frame under sine wave of 46 Hz
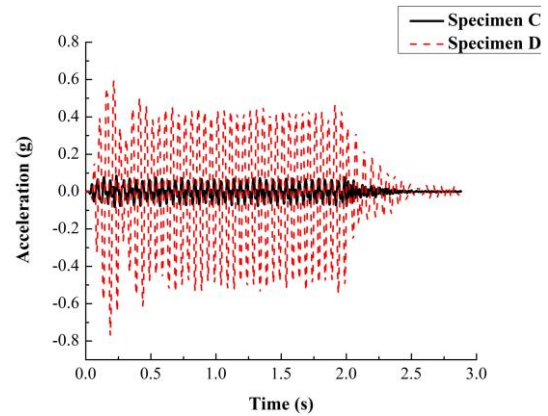
Fig. 6.20 Accelerations in X direction on the top of the frame under sine wave of 20Hz

Then tests of excitations with a frequency falling out of the band gaps, i.e., 20 Hz were conducted, and the results are shown in Fig. 6.20. Fig. 6.20 shows that the response of Specimen D is greater than that of Specimen C. The peak acceleration of Specimen C is less than that of Specimen D in the steady state.

6.2.1.2.3 Seismic S wave results

Modified seismograms were used to verify the effects of the application of frequency band gaps. Acceleration stayed the same, and the vibration period changed to modify the seismogram so that a main frequency of 46 Hz was achieved. Three seismic records from the PEER Ground Database[97] were used in the field tests, i.e., BORAH.AS/HAU000 (1983/10/29) with the main frequency of 18.0 Hz, BORAH.AS/HAU090 (1983/10/29) with the main frequency of 18.1 Hz, and LANDERS/LCN-UP (1992/06/28) with the main frequency of 12.8 Hz. All seismic records were modified to make the main frequency match the band gaps, i.e., 46 Hz.

Horizontal acceleration time-histories on the top of the steel frames of both specimens under excitation of modified BORAH.AS/HAU000 (1983/10/29) are shown in Fig. 6.21. The peak acceleration of Specimen C was 1.34g and that of Specimen D was 0.64g. Fig. 6.21 shows that Specimen D at peak acceleration in the X direction was reduced to 47.7% as compared to the steel frame without the periodic foundation, Specimen C. The responses of the two specimens under the modified seismogram, BORAH.AS/HAU090 (1983/10/29), are shown in Fig. 6.22. The peak acceleration on top of the frame of Specimen C was 1.08g and that of the Specimen D was 0.65g. The peak acceleration on the top of the steel frame was reduced to 60.6% as compared to the specimen without the periodic foundation. Fig. 6.23 shows similar responses for both specimens C and D under the modified seismogram, LANDERS/LCN-UP. The peak acceleration of Specimen C was 1.11g, and the peak acceleration of Specimen D was 0.58g. The peak acceleration at the top of the steel frame in Specimen D was 52.6% that of Specimen C.
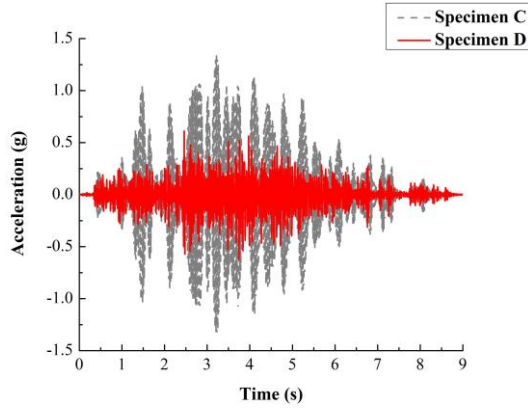
Fig. 6.21 Acceleration in X direction on the top of the frame under modified BORAH.AS/HAU000 with a main frequency of 46Hz
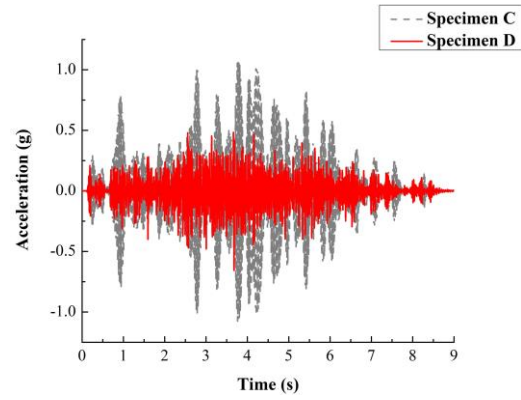
Fig. 6.22 Acceleration in X direction on the top of the frame under modified BORAH.AS/HAU090 with a main frequency of 46Hz
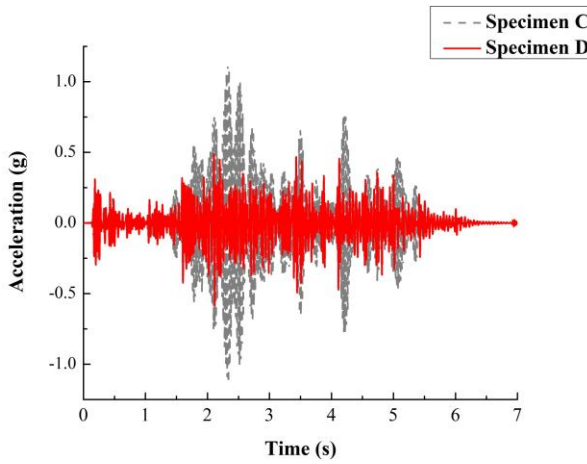
Fig. 6.23 Acceleration in X direction on the top of the frame under modified LANDERS/LCN-UP with a main frequency of 46Hz

The test results indicate overall that the periodic foundation is capable of providing effective isolations for the S wave vibrations falling into the designed band gap.

6.2.2 P wave test results of 2D periodic foundations

6.2.2.1 Use of Thumper Shaker

6.2.2.1.1 Stepped sine P wave results

Fig. 6.24 and Fig. 6.25 show the test results of the stepped sine wave tests. In Fig. 6.24, accelerations in the Y direction on concrete on top of the periodic foundation, sensor serial number 1783 in Fig. 5.19 in the frequency domain, are shown in the red curve, and the black dashed curve in the figure is the acceleration in the Y direction, at the bottom of the periodic foundation, sensor serial number 1781 in Fig. 5.19. When the acceleration on the top concrete of the periodic foundation is larger than that on the bottom of the periodic foundation, the excitation frequencies are outside the band gaps. The acceleration of Sensor 1783 clearly is smaller than that of Sensor 1781, i.e., from 23.62 Hz-54.97 Hz and 69.67 Hz-85.35 Hz. The test results of these two band gaps are discussed in the following sections:

Fig. 6.25 shows the ratio of accelerations on the top of the periodic foundation concrete to accelerations on the bottom of the periodic foundation concrete; the purpose of this figure is to illustrate the effects of band gaps once more. The frequency band gaps, therefore, appear when the value of the Y-axis is smaller than 1 (10^0 in Fig. 6.25), i.e., 23.6 Hz-55.0 Hz; 69.7 Hz-85.4 Hz, as shown in the figure. Fig. 6.26, shows the phase difference between the point on the core iron cylinder, Sensor 1461, and the point on the concrete, Sensor 1782. Note that the phase difference becomes larger when the frequency falls within 58 Hz-82 Hz, which is near the second attenuation zone, 69.7 Hz-85.4 Hz. The vibration phase of the cylinder and the concrete are different when the excitation frequency is within the band gaps.
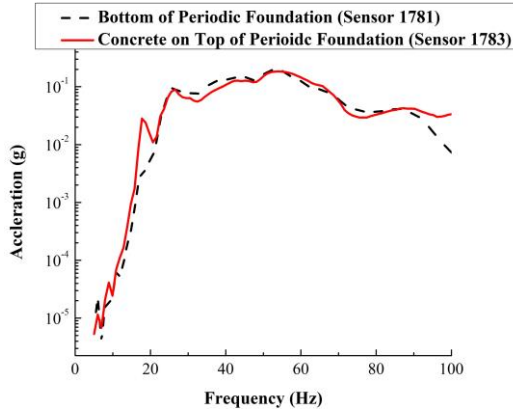
Fig. 6.24 Acceleration in Y direction
on the top and bottom of Specimen D
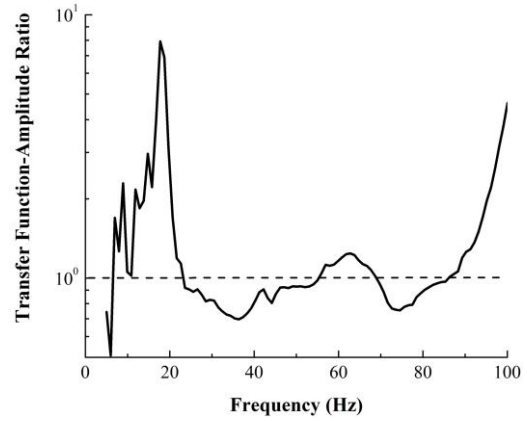
Fig. 6.25 Transfer function of Specimen D
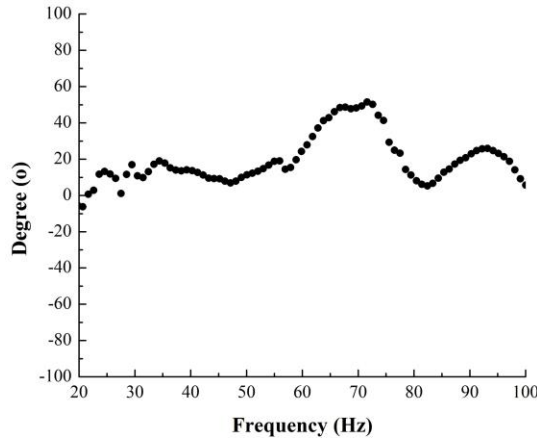
Fig. 6.26 Phase differences of P wave excitation

6.2.2.1.2 Fixed sine P wave results

Harmonic P wave excitations were applied to the specimens with frequency in the range of the band gaps, i.e., 36 Hz and 72.6 Hz, according to the results of the stepped sine wave tests. Fig. 6.27 shows acceleration in the Y direction on concrete on top of the periodic foundation, Sensor 1783, under a sine wave of 72.6 Hz. The dashed gray curve represents acceleration response on the bottom of the periodic foundation, Sensor 1781. Fig. 6.27 shows that, at the beginning of the harmonic motion, the two curves have nearly the same peak acceleration owing to the transient effect. When the specimen was in the

steady state, the peak acceleration on top of the periodic foundation was 0.04g, and on the bottom of the periodic foundation it was 0.052g. The peak acceleration of the top periodic foundation, Sensor 1783, was 80% that of the bottom periodic foundation, Sensor 1781. Fig. 6.28 shows the response of specimen D under harmonic P waves under 36 Hz. When the specimen was in steady state, the peak acceleration on top of the periodic foundation was 0.092g, and on the bottom of the periodic foundation it was 0.123g. The peak acceleration of concrete on top of the periodic foundation, Sensor 1783, was 75% that of periodic foundation on the bottom, Sensor 1781.
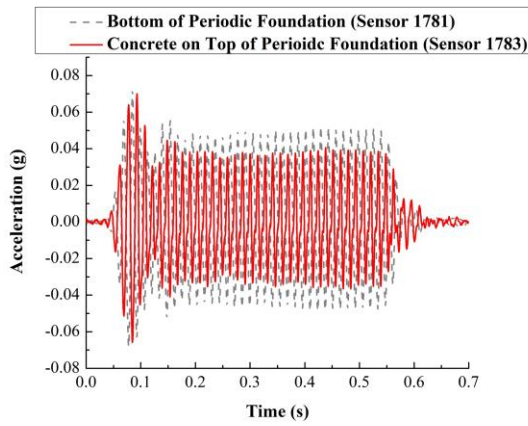
Fig. 6.27 Acceleration in Y direction under a sine wave of 72.6Hz
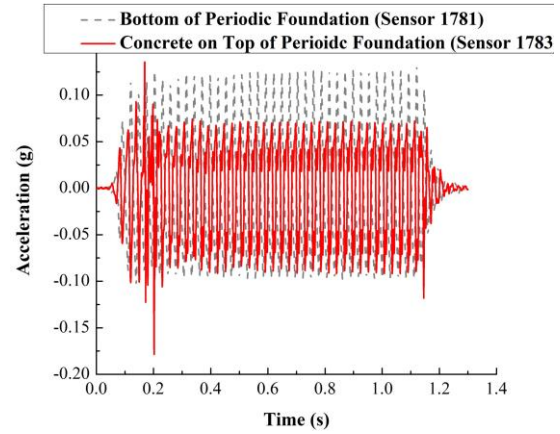
Fig. 6.28 Acceleration in Y direction under a sine wave of 36Hz

The wave was blocked from passing through the unit cell rows when the estimated frequency excitation was applied to the FE model. Fig. 6.29 shows the accelerations of the core cylinders in rows 2 and 7. The dashed gray curve is the acceleration of Sensor 1784, which is located in the 7th row from the top of the periodic foundation. The red curve is the acceleration of Sensor 1461, which is located in the 2nd row from the top of the periodic foundation. The accelerations are reduced.
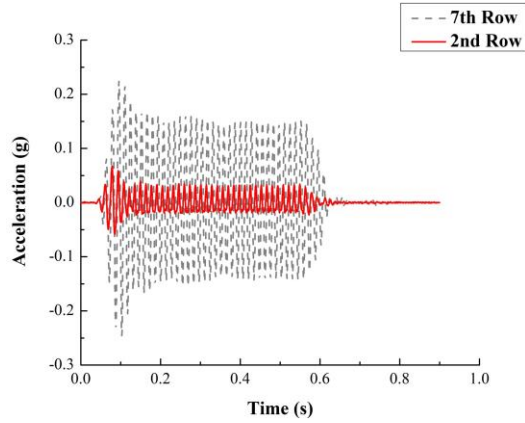
Fig. 6.29 Accelerations of core cylinders in different positions under 72.6Hz

6.2.2.1.3 Seismic P wave results
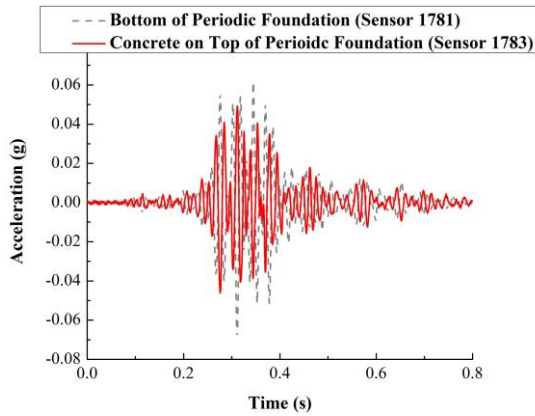
Fig. 6.30 Acceleration in Y direction under modified Bishop (Rnd Val) P0486/MCG-UP
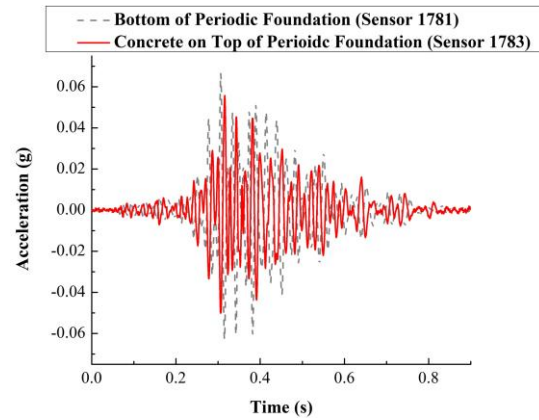
Fig. 6.31 Acceleration in Y direction under modified Bishop (Rnd Val) P0486/MCG-360

The modified seismograms also were used to verify the band gap effect. The two seismograms, i.e., Bishop (Rnd Val) P0486/MCG-UP (1984/11/23) with a main frequency of 8.3 Hz and Bishop (Rnd Val) P0486/MCG-360 (1984/11/23) with a main frequency of 8.16 Hz were modified so that the main frequency fell into the band gaps, i.e., 72.6 Hz. The horizontal acceleration time histories of concrete at the top and bottom of the periodic foundation are shown in Fig. 6.30 under the modified seismogram, Bishop (Rnd Val) P0486/MCG-UP with the main frequency of 72.6 Hz. Fig. 6.30 shows that the

126

peak vertical acceleration of concrete at the top of the periodic foundation, Sensor 1783, is 0.049g and was reduced by 27.9% as compared to the sensor at the bottom of the periodic foundation, Sensor 1781, which was 0.068g. The responses of the specimens under the seismogram, modified Bishop (Rnd Val) P0486/MCG-360 (1984/11/23) with the main frequency of 72.6 Hz, are shown in Fig. 6.31. The peak acceleration in the vertical direction at the top of the concrete of the periodic foundation, Sensor 1783, was 0.055g and was reduced by 16.24%, as compared to the peak vertical acceleration at the bottom of the periodic foundation, Sensor 1781, which was 0.066g. The test results indicate that the periodic foundation was capable of providing an effective filter to isolate the vibration, and the frequency contents fell into the desired band gaps.

6.3   Experimental Results of 3D periodic foundations

6.3.1   Shear wave tests

6.3.1.1   Use of Rattler shaker

6.3.1.1.1   Stepped sine S wave results

Fig. 6.32 shows the amplitudes of the transfer functions of both specimens; the transfer function is the ratio between the acceleration measured on the top of the steel column and that measured on the RC footing of the individual specimen. The transfer function for Specimen E is the acceleration ratio of sensors 1784 to 1458 in the frequency domain, and for Specimen F, the transfer function is the ratio of sensors 1783 to 1463 in the frequency domain. The ratio of the transfer function of Specimen F to the transfer function of Specimen E is plotted in Fig. 6.33 to better illustrate the test results. The frequency band gaps occur where the ratio is less than 1, which is below the black dashed

127

line, as shown in Fig. 6.33. Fig. 6.33 shows that the steel column on Specimen F experienced a lower level of acceleration ratio than Specimen E in frequency ranges 10.3 Hz to 44.1 Hz, 45.6 Hz to 50.4 Hz, 53.2 Hz to 88.1 Hz, and 90.0 Hz to 100 Hz, especially at 35.1Hz. When amplitudes of the transfer functions of Specimen F were less than those of Specimen E, seismic motions were mitigated by the periodic foundation.
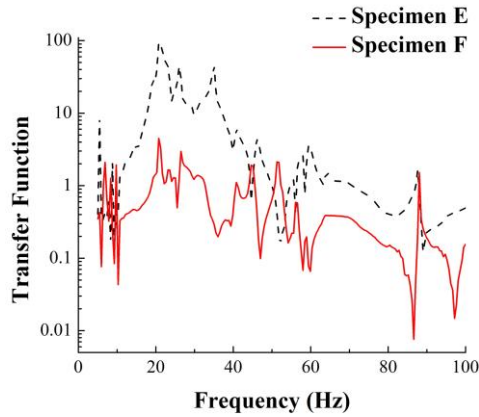
Fig. 6.32 Transfer function between the top of the steel column and RC footing
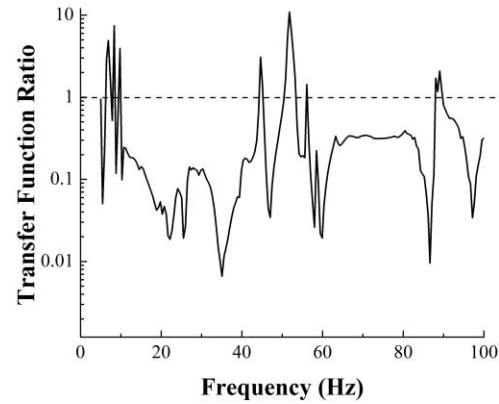
Fig. 6.33 Transfer function ratio of the steel column for the specimens

Fig. 6.34 shows the amplitudes of the transfer functions from both specimens, where the transfer function is the ratio between the acceleration measured on the top of the concrete of the periodic foundation to that measured on the RC footing. For Specimen E, the transfer function of concrete was the acceleration ratio of sensors 1461 to 1458 in the frequency domain, and for Specimen F the transfer function of concrete was the ratio of sensors 1780 to 1463. Fig. 6.34 shows that the response of top concrete in Specimen F was smaller than in Specimen E in frequency ranges 31.3 Hz to 39.4 Hz, 46.1 Hz to 47.5 Hz, and 56.6 Hz to 87.6 Hz. The ratio of transfer function of Specimen E to transfer function of Specimen F is shown in Fig. 6.35. When the values were lower than 1, the response on top of the concrete of Specimen F was smaller than of Specimen E.
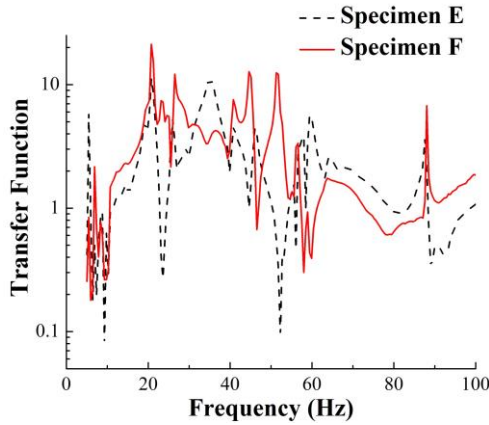
Fig. 6.34 Transfer function between the top of concrete of periodic foundation and RC footing
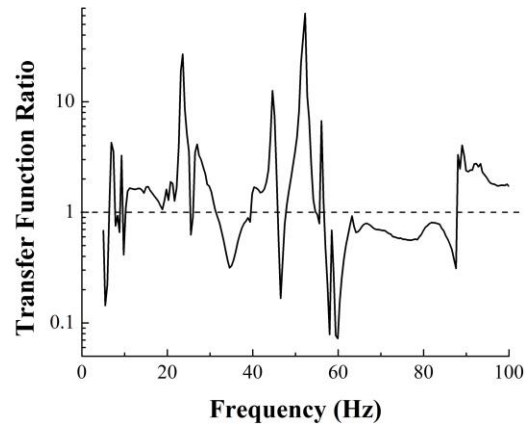
Fig. 6.35 Transfer function ratio of the top of concrete for the specimens

Curves in Fig. 6.33 and Fig. 6.35 are plotted together in Fig. 6.36. When the red solid curve and dashed black curve are under the blue dashed line, the periodic foundation mitigates the input S wave. According to Fig. 6.36, the trend of the attenuation from both the top of the steel column and the top of the concrete on the periodic foundation match, especially in the range of 31.3 Hz to 39.4 Hz. Fig. 6.37 shows the acceleration of Sensor 1780 on top of the concrete of the periodic foundation, and 1463, on top of the RC footing. The acceleration on top of the periodic foundation concrete is less than on top of the RC footing in most excitation frequency ranges.
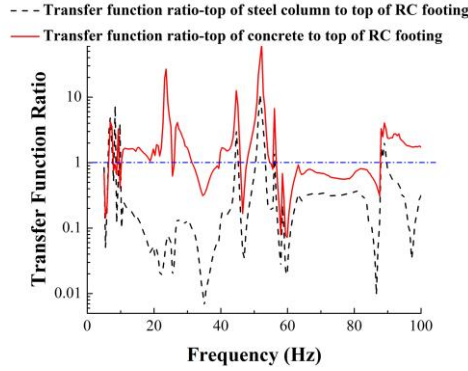
Fig. 6.36 Comparison of ratio of transfer function
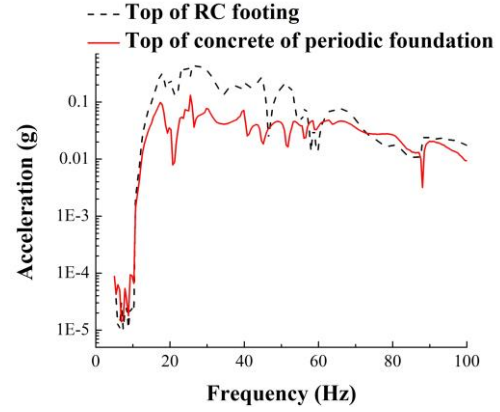
Fig. 6.37 Acceleration at the top and bottom of concrete of the periodic foundation

6.3.1.1.2 Fixed sine S wave results

Single-frequency sinusoidal waves were applied to the specimens within the range of the band gaps, i.e. 35.1 Hz with 40 cycles, to verify the effects of the frequency band gaps. Fig. 6.38 shows the accelerations in the X direction on the top of the steel column under a sine wave with a frequency of 35.1 Hz. The dashed gray curve shows the acceleration response at the top of the steel column on a conventional RC foundation, i.e., Sensor 1784 of Specimen E, while the red curve is the acceleration response at the top of the steel column on a periodic foundation, i.e., Sensor 1783 of Specimen F. The response of Specimen F was much less that of Specimen E. Fig. 6.39 shows the acceleration of the top concrete, Sensor 1461 of Specimen E and Sensor 1780 of Specimen F. At the beginning of acceleration input, both specimens E and F were subjected to the transient effect until the specimens reached the steady state. When the input excitations stopped, the specimens started free vibration, and the input frequency was no longer equal to the excitation frequency. The accelerations of the specimens, therefore, were amplified before and after the steady states. At the top of the concrete in the periodic foundation the

130

peak acceleration of Sensor 1461 on Specimen E was 0.78g, and the peak acceleration of Sensor 1780 on Specimen F was 0.58g. The peak acceleration in Specimen F was reduced to 74.8% of the peak acceleration as compared to the traditional foundation. In the steady state, however, the peak acceleration of Sensor 1461 on Specimen E was 0.67g, and the peak acceleration of Sensor 1780 on Specimen F was 0.25g. The peak acceleration in Specimen F was reduced to 37.5% that of Specimen E. Fig. 6.40 shows acceleration on the concrete of the third row of unit cells from the bottom of the periodic foundation, i.e., Sensor 1459 of Specimen E and Sensor 1779 of Specimen F. In the steady state, the peak acceleration of Sensor 1459 on Specimen E was 0.36g, and the peak acceleration of Sensor 1779 on Specimen F was 0.16g. The reduction of the peak acceleration at this location was about 56%.
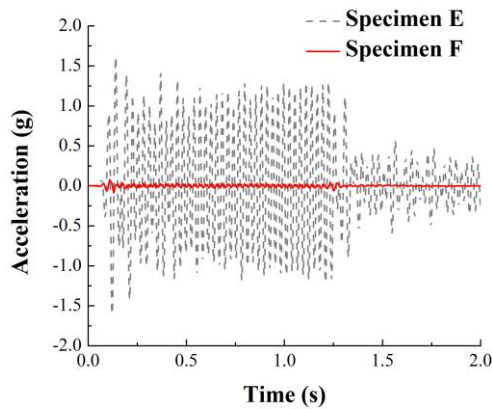
Fig. 6.38 Acceleration at the top of the steel column under a sine wave 35.1Hz
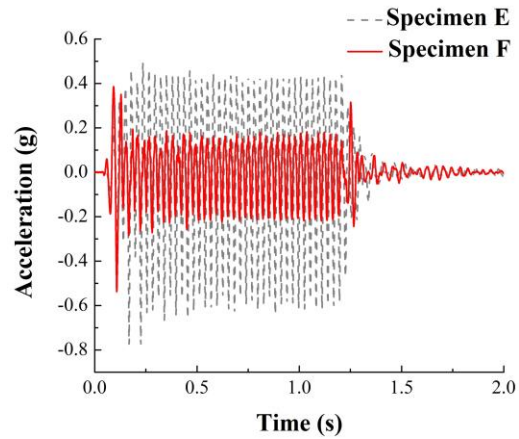
Fig. 6.39 Acceleration at the top of the concrete under a sine wave 35.1Hz
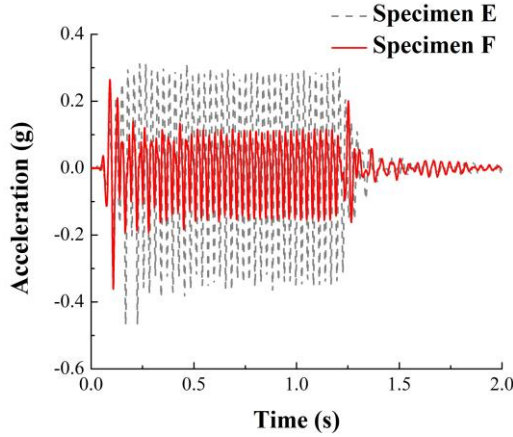
Fig. 6.40 Acceleration in middle of the concrete under a sine wave 35.1Hz
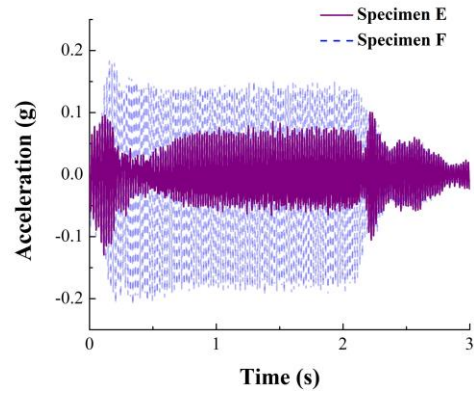
Fig. 6.41 Acceleration at the top of the concrete under a sine wave 52Hz

Excitation tests with a frequency falling out of the band gaps, i.e. 52 Hz, were conducted after the test with a frequency falling within the band gaps. The accelerations on top of the concrete in both the traditional RC foundation and the periodic foundation are plotted in Fig. 6.41, i.e., Sensor 1461 of Specimen E and Sensor 1780 of Specimen F. Fig. 6.41 shows that the response of Specimen F was greater than Specimen E in the steady state.

6.3.1.1.3 Seismic S wave results

Modified seismograms were used to verify the effects of the frequency band gap. The Fourier transformations were used to determine the corresponding frequency spectrum of each seismic record. The frequency at which the amplitude reaches its maximum value was considered to be the main frequency. To modify the seismogram, the accelerations were kept the same, and the period was modified to set the main frequency at 35.1 Hz. A seismic record from the PEER Ground Database[97] was used in the field tests, i.e., BORAH.AS/HAU090 (1983/10/29), with a main frequency of 18.1

Hz. The seismic record was modified so that the main frequency matched the band gap frequency, i.e., 35.1 Hz.

The acceleration in the X direction of each sensor was recorded in the time domain. Fig. 6.42 shows the horizontal acceleration time-histories on the top of the steel column from both specimens under the excitations of the modified BORAH.AS/HAU090 (1983/10/29), Fig. 6.42 shows that, for the steel column on the periodic foundation, i.e., with a peak acceleration of 0.14g from Sensor 1783, the peak acceleration in the X direction was reduced to 8.08% as compared to that of the steel column with the conventional foundation, i.e., with a peak acceleration of 1.73g from Sensor 1784. The responses at the top of the concrete of the two specimens, i.e., sensors 1461 and 1780, are shown in Fig. 6.43. The peak acceleration on the top of the concrete of Specimen F, with a peak acceleration of 0.55g from Sensor 1780, was reduced to 76.76%, as compared to Specimen E, with a peak acceleration of 0.72g from Sensor 1461, with the conventional foundation. Fig. 6.44 shows similar responses for the two specimens, E and F. The red curve is the acceleration of the concrete in the middle of the periodic foundation, with a peak acceleration of 0.34g from Sensor 1779, and the gray curve is the acceleration of the concrete in the middle of the conventional foundation, with a peak acceleration of 0.45g from Sensor 1459. The peak acceleration at the top of the concrete in Specimen F was 75.2% that of Specimen E.

Overall, the test results indicate that the periodic foundation is capable of providing effective isolation for the S wave vibrations falling into the designed band gap.
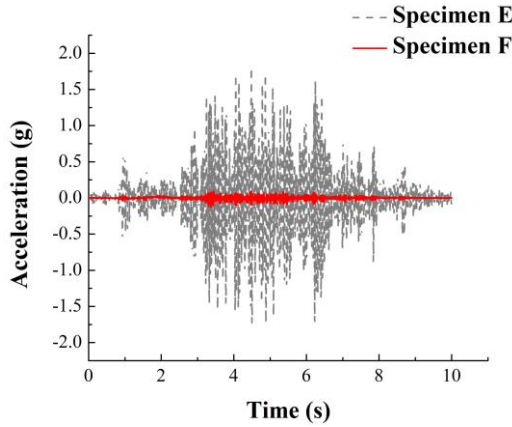
Fig. 6.42 Acceleration in X direction at the top of the column under modified BORAH.AS/HAU090 with a main frequency of 35.1Hz
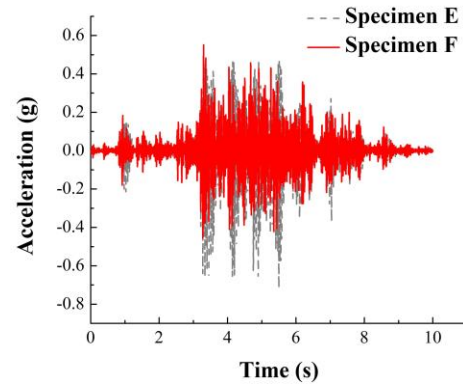
Fig. 6.43 Acceleration in X direction at the top of concrete under modified BORAH.AS/HAU090 with a main frequency of 35.1Hz
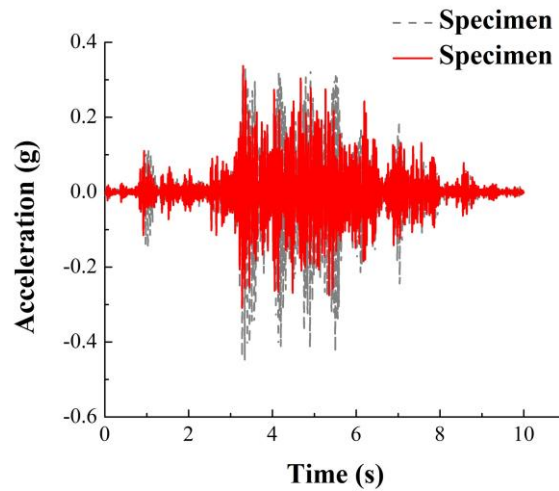
Fig. 6.44 Acceleration in X direction in the middle of the concrete under modified BORAH.AS/HAU090 with a main frequency of 35.1Hz

6.3.1.2   *Use of T-Rex shaker*

6.3.1.2.1   *Stepped sine S wave results*

Fig. 6.45 shows the transfer functions of Specimen F under 2V and 4.5V excitations, where the transfer function is the ratio of the acceleration measured on the top of the steel column relative to the acceleration measured on the RC footing of the

individual specimen. The transfer function of Specimen F is the ratio of sensors 1783 to 1463 in the frequency domain. The transfer function of Specimen E is the acceleration ratio of sensors 1784 to 1458 in the frequency domain. The attenuation zones of Fig. 6.45 occur where the ratio is smaller than 1. The output value of Specimen F was smaller than the input when the acceleration on top of the column was smaller than on top of the RC footing. The attenuation zones under 2V excitation are 40.8 Hz-46.5 Hz and 56 Hz-100 Hz, and the attenuation zones under 4.5V excitation are 37.5 Hz-46.6 Hz and 59.4 Hz-100 Hz. The results from the gray dashed curve and the red solid curve were in agreement.

To better illustrate the test results, the ratio of the transfer function of Specimen F to the transfer function of Specimen E (transfer function amplitude ratio) is plotted in Fig. 6.46. When the values are lower than 1, the transfer function of Specimen F is smaller than that of Specimen E. Fig. 6.46 shows that, with 4.5V excitation, the steel column on Specimen F experienced a lower level of accelerations ratio than Specimen E in frequency ranges 5 Hz-48.4 Hz, 53.7 Hz-58 Hz, and 59.4 Hz-88.1 Hz, especially at 43.7 Hz. Fig. 6.47 shows the transfer function amplitude ratio on the concrete of the two specimens. The transfer function on top of the concrete for Specimen E is the ratio of sensors 1461 to 1458, and the transfer function on top of the concrete for Specimen F is the ratio of sensors 1780 to 1463. The transfer function amplitude ratio in Fig. 6.47 is the ratio of the transfer function on top of the concrete of Specimen F to that of Specimen E. Fig. 6.47 shows that with 4.5V excitation, the concrete on top of Specimen F experienced a lower level of acceleration ratio than Specimen E in frequency ranges 36.5 Hz-46.5 Hz, 54.4 Hz-57.9 Hz, and 59.9 Hz-89 Hz, especially at 43.7 Hz.

When amplitudes of the transfer functions of Specimen F were less than those of Specimen E, seismic motions were mitigated by the periodic foundation. Although under large, dissimilar excitation levels, the three figures show that the difference of the attenuation zones was small.
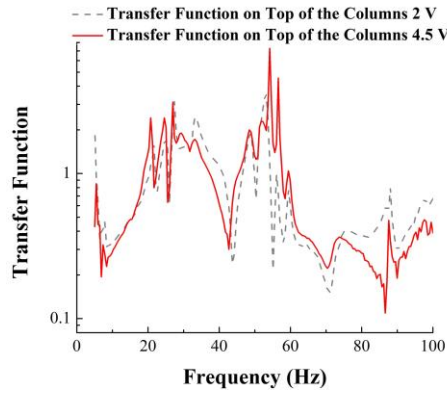
Fig. 6.45 Transfer function on top of the column of Specimen F under 2V and 4.5V excitation
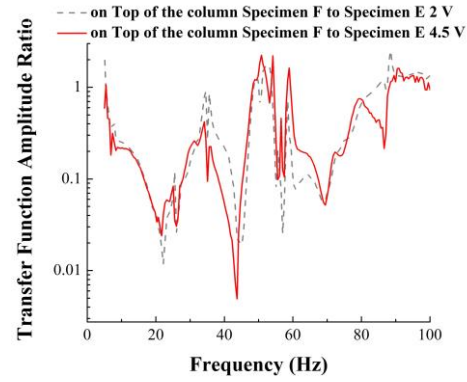
Fig. 6.46 Transfer function amplitude ratio on top of the column under 2V and 4.5V excitation
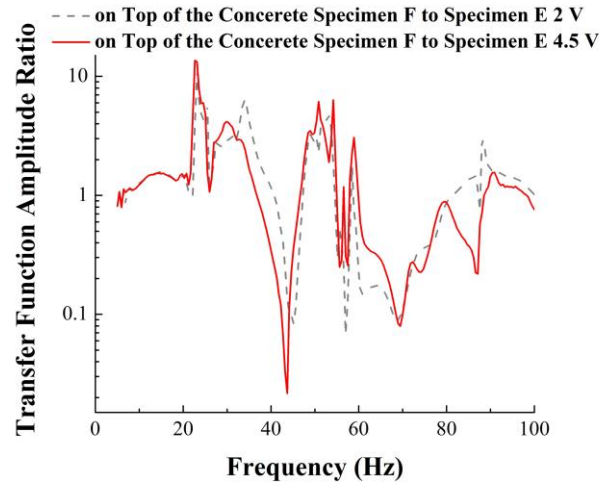
Fig. 6.47 Transfer function amplitude ratio on top of the concrete under 2V and 4.5V excitation

6.3.1.2.2 *Fixed Sine S wave results*

Single frequency sinusoidal waves were applied to the specimens within the range of the band gaps, i.e. 43.7Hz with 40 cycles to verify the effects of the frequency band

gaps. The input accelerations of the two specimens were first checked to eliminate the possible differences of shaking levels between the two foundations. The accelerations on the RC footing were considered to be the input accelerations, i.e., Sensor 1458 for Specimen E and Sensor 1463 for Specimen F. Fig. 6.48 shows the input of the two specimens under 43.7 Hz fixed sine wave with 2V excitation level. Specimen F experienced a higher excitation level than Specimen E. The Fourier transform was conducted for the input accelerations; the results are shown in Fig. 6.49. The peak amplitude of Specimen F is 1.43 times that of Specimen E; Specimen F accelerations were divided by 1.43 to make the input and output of the two specimens comparable. Fig. 6.50 shows the input accelerations of the two specimens after modification. For every test and result, the input accelerations of the two specimens were checked and modified, and the resulting figures were plotted.
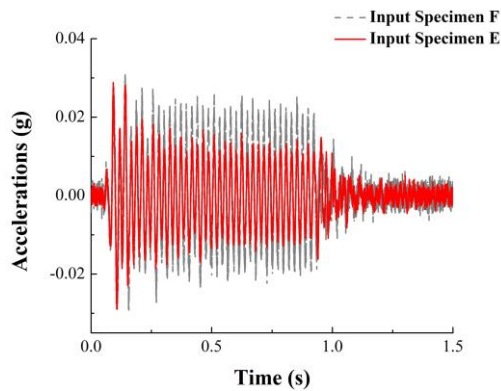
Fig. 6.48 Input acceleration of the two specimens
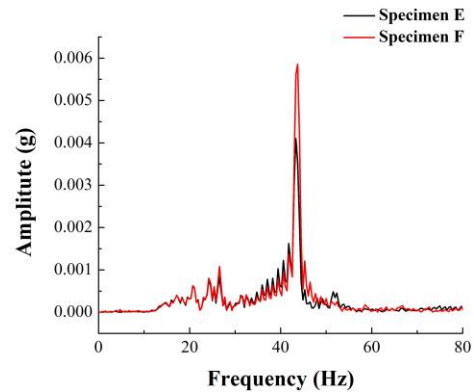
Fig. 6.49 Input acceleration in the frequency domain
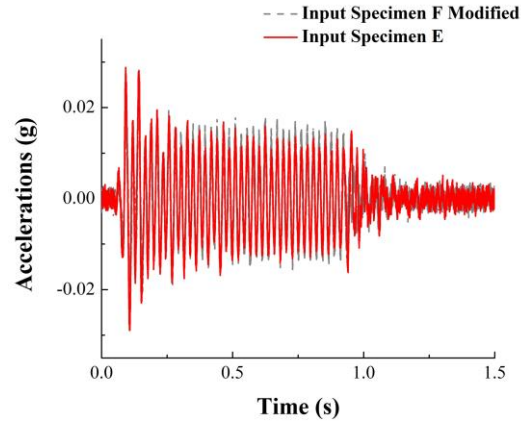
Fig. 6.50 Input acceleration after modification

Fig. 6.51 shows accelerations in the X direction on the top of the steel column under a sine wave with a frequency of 43.7 Hz. The dashed gray curve is acceleration response at the top of the steel column on a conventional RC foundation, i.e., Sensor 1784 of Specimen E, while the red curve is the acceleration response at the top of the steel column on a periodic foundation, i.e., Sensor 1783 of Specimen F. The response of Specimen F is much smaller than Specimen E. The peak acceleration of Sensor 1784 on Specimen E is 0.35g, and the peak acceleration of Sensor 1783 on Specimen F is 0.02g. The peak acceleration in Specimen F is reduced to 5.7% that of Specimen E. Fig. 6.52 shows the acceleration of the top concrete, Sensor 1461 of Specimen E and Sensor 1780 of Specimen F. At the beginning of acceleration input, both Specimens E and F were subjected to transient effect until the specimens reached the steady state. When the input excitations stopped, the specimens started free vibration, and the input frequency was no longer equal to the excitation frequency. The accelerations of the specimens, therefore, were amplified before and after the steady states. At the top of the concrete in the periodic foundation, the peak acceleration of Sensor 1461 on Specimen E was 0.106g, and the peak acceleration of Sensor 1780 on Specimen F was 0.028g. The peak

acceleration in Specimen F was reduced to 26.4% that of Specimen E. Fig. 6.53 shows acceleration on the concrete of the third row of unit cells from the bottom of the periodic foundation, i.e., Sensor 1459 of Specimen E and Sensor 1779 of Specimen F. The peak acceleration of Sensor 1459 on Specimen E was 0.075g in the steady state, and the peak acceleration of Sensor 1779 on Specimen F was 0.0185g. The reduction of the peak acceleration at this location, therefore, was about 75.3%. Fig. 6.54 shows the acceleration on top of the column and the input acceleration of Specimen F under a 2V fixed sine S wave of 43.7 Hz. In the steady state, the peak response on top of the column was 0.0113g, which was 43.5% of the peak input acceleration, 0.026g.
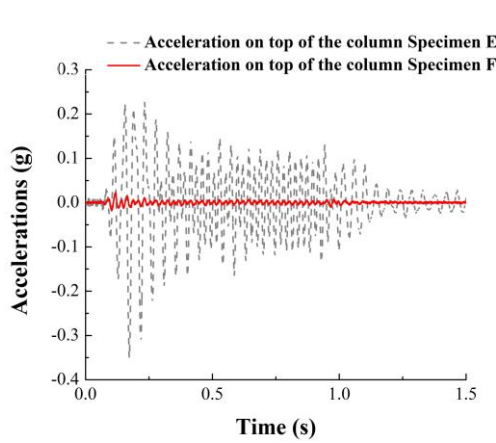
Fig. 6.51 Acceleration on top of the column under 2V fixed sine S wave 43.7 Hz
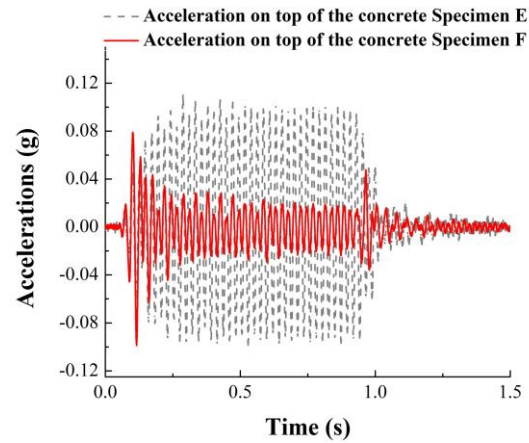
Fig. 6.52 Acceleration on top of the concrete under 2V fixed sine S wave 43.7 Hz
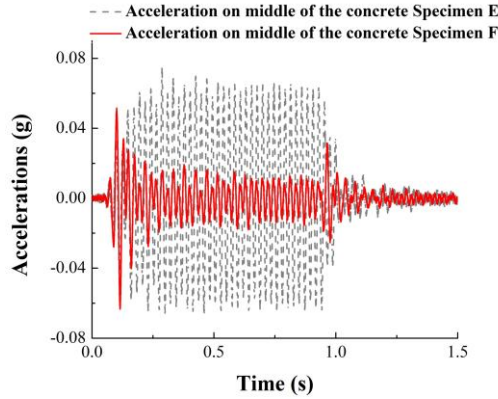
Fig. 6.53 Acceleration on middle of the concrete under 2V fixed sine S wave 43.7 Hz
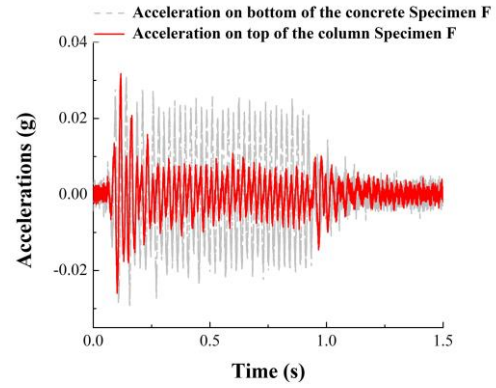
Fig. 6.54 Acceleration on top and bottom of the column under 2V fixed sine S wave 43.7 Hz

Fig. 6.55 to Fig. 6.58 show results of the two specimens under a 4.5V fixed sine S wave of 43.7 Hz. The dashed gray curve in Fig. 6.55 shows the acceleration response at the top of the steel column on a conventional RC foundation, i.e., Sensor 1784 of Specimen E, while the red curve is the acceleration response at the top of the steel column on a periodic foundation, i.e., Sensor 1783 of Specimen F. Sensor 1784 on Specimen E was 0.594g, and the peak acceleration of Sensor 1783 on Specimen F was 0.0195g. The peak acceleration in Specimen F was reduced to 3.3% of Specimen E. Fig. 6.56 shows the acceleration of the top concrete, Sensor 1461 of Specimen E and Sensor 1780 of Specimen F. The peak acceleration of Sensor 1461 on Specimen E was 0.1244g at the top of the concrete, and the peak acceleration of Sensor 1780 on Specimen F was 0.0326g. The peak acceleration in Specimen F was reduced to 26.2% of Specimen E. Fig. 6.57 shows the acceleration on the concrete of the third row of unit cells from the bottom of the periodic foundation, i.e., Sensor 1459 of Specimen E and Sensor 1779 of Specimen F. In the steady state, the peak acceleration of Sensor 1459 on Specimen E was 0.081g, and the peak acceleration of Sensor 1779 on Specimen F was 0.023g. The reduction of the peak acceleration at this location, therefore, was about 71.6%. Fig. 6.58 shows the

140

acceleration on top of the column and the input acceleration of Specimen F under a 4.5V fixed sine S wave of 43.7 Hz. In the steady state, the peak response on top of the column was 0.0169g, which was 53% of the peak input acceleration, 0.0319g.

After a comparison of the two tests using the S wave frequency, but different excitation levels, was completed, reductions of the periodic foundation were obtained and are shown in Table 6.1. Note that the reduction of the column under the 4.5V excitation level was close to that under the 2V excitation level.

Table 6.1 Comparison of the specimens under different excitation level S waves

Excitation Level	Peak Acceleration of Specimen F to Specimen E		
	Top Of the Column	Top Of the Concrete	Middle Of the Concrete
2V	5.7%	26.4%	24.7%
4.5V	3.3%	26.2%	28.4%
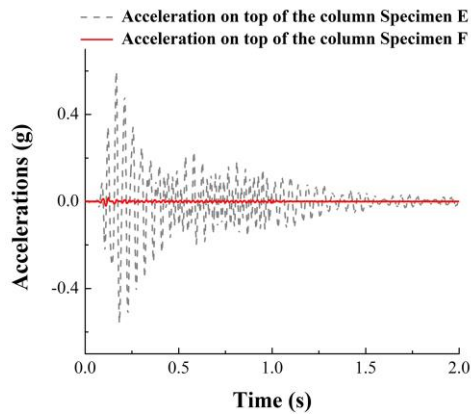
Fig. 6.55 Acceleration on top of the column under 4.5V fixed sine S wave of 43.7 Hz
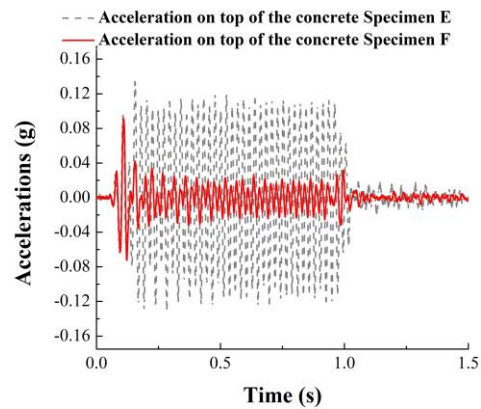
Fig. 6.56 Acceleration on top of the concrete under 4.5V fixed sine S wave of 43.7 Hz
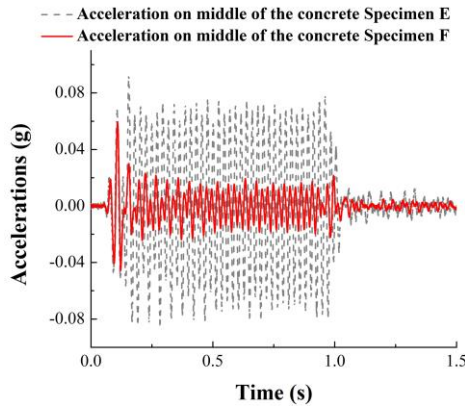
Fig. 6.57 Acceleration on middle of the concrete under 4.5V fixed sine S wave of 43.7 Hz
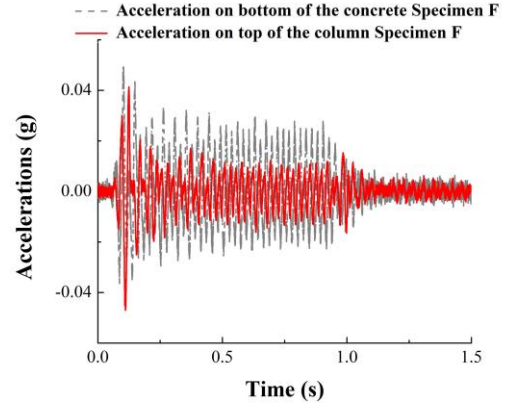
Fig. 6.58 Acceleration on top of the concrete under 4.5V fixed sine S wave of 43.7 Hz

6.3.1.2.3 Seismic S wave results

Modified seismograms were used to verify the effects of the frequency band gap. To find the main frequency of each seismic record, the Fourier transformations were used to determine the corresponding frequency spectrum. The frequency at which the amplitude reaches its maximum value was considered the main frequency. Acceleration was kept the same to modify the seismogram, and the period was revised to obtain the main frequency of 43.7 Hz. A seismic record from the PEER Ground Database[97] was used in the field tests, i.e., BORAH.AS/HAU000 (1983/10/29) with a main frequency of 17.3 Hz. The seismic record was modified to make the main frequency match the band gap frequency, i.e., 43.7 Hz, the same frequency as for the S wave fixed sine tests. There were two excitation levels for the seismic S wave tests, i.e., 2V and 4.5V.

The acceleration in the X direction of each sensor was recorded in the time domain. The horizontal acceleration time-histories on the top of the steel column of both specimens under 2V excitation of the modified BORAH.AS/HAU000 (1983/10/29) are shown in Fig. 6.59. Fig. 6.59 shows that, for the steel column on the periodic foundation,

142

i.e., with a peak acceleration of 0.0274g from Sensor 1783, the peak acceleration in the X direction was reduced to 6.66%, as compared to that of the steel column with the conventional foundation, i.e., with a peak acceleration of 0.412g from Sensor 1784. The responses at the top of the column and on the top of the RC footing of Specimen F, i.e., sensors 1783 and 1463, are shown in Fig. 6.60. The peak acceleration on the top of the column of Specimen F, with a peak acceleration of 0.0274g from Sensor 1783, was reduced to 78.96%, as compared to the input accelerations, with a peak acceleration of 0.0347g from Sensor 1463.

Fig. 6.61 shows similar responses for the two specimens, E and F, under 4.5V modified BORAH.AS/HAU000 (1983/10/29) with a main frequency of 43.7 Hz. The red curve is the acceleration on top of the column of Specimen F, with a peak acceleration of 0.042g from Sensor 1783, and the gray curve is the acceleration on top of the column of Specimen E, with a peak acceleration of 1.11g from Sensor 1784. The peak acceleration at the top of the column in Specimen F is 3.78% that of Specimen E. Fig. 6.62 shows the input at the RC footing and the output acceleration on top of the column of Specimen F. The red curve shows the peak acceleration on top of the column, Sensor 1783, to be 0.042g, and the gray dashed curve shows the peak input acceleration on top of the RC footing of Specimen F, Sensor 1463, was 0.064g. The output peak acceleration of Specimen F was 65.6% of the input peak acceleration.

The response of the column on a periodic foundation was reduced under both 2V and 4.5V excitation levels. Overall, the test results indicate that the periodic foundation was capable of providing effective isolations for the S wave vibrations falling into the designed band gap.
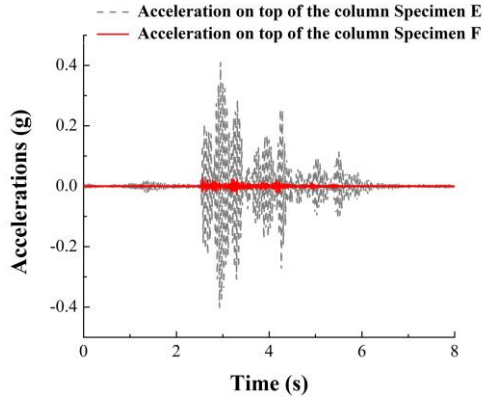
Fig. 6.59 Acceleration on top of the column of the two specimens under 2V modified BORAH.AS/HAU000
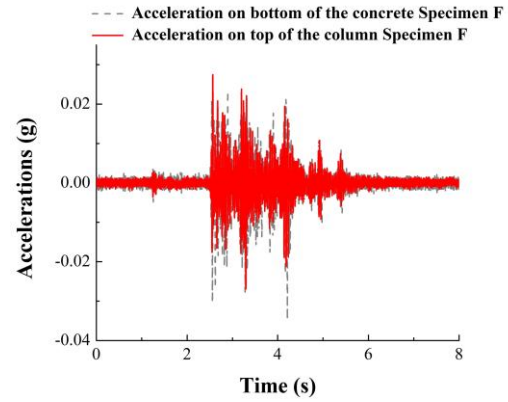
Fig. 6.60 Acceleration on top of the column and input of Specimen F under 2V modified BORAH.AS/HAU000
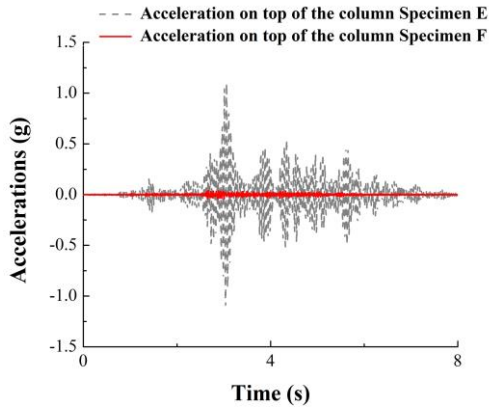
Fig. 6.61 Acceleration on top of the column of the two specimens under 4.5V modified BORAH.AS/HAU000
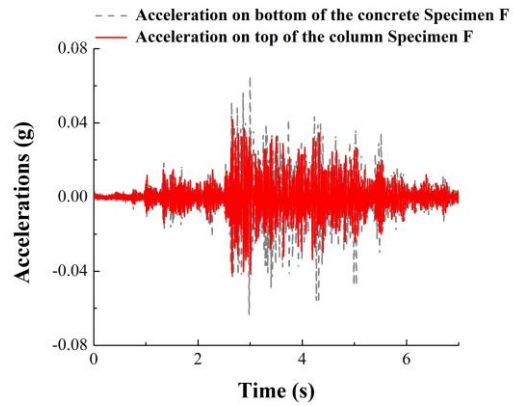
Fig. 6.62 Acceleration on top of the column and input of Specimen F under 4.5V modified BORAH.AS/HAU000

6.3.2 Primary wave tests

6.3.2.1 Use of Raptor shaker

There are three types of tests for P wave excitation; as with tests for the S wave, they include stepped sine P wave, fixed sine P wave, and seismic P wave tests. The first type of test involved the application of a stepped sine wave to find the frequency band gaps of the periodic foundation with a steel column for the P wave excitations. Fixed frequency sine waves from 100 Hz down to 5 Hz were applied to the test specimens. The

144

amplitude of each sensor at each frequency step was recorded. The results of the stepped sine tests that showed fixed sine waves with frequencies falling within the band gaps were then applied to the specimens. Finally, the modified seismograms were used to verify the band gap effect. The time history of each sensor was recorded during the last two test procedures.

6.3.2.1.1 Stepped sine P wave results

The series of figures, Fig. 6.63 to Fig. 6.67, show the test results of the P wave stepped sine tests. Fig. 6.63 shows a ratio of acceleration in the Y direction at the top of the steel column. Sensor 1783 in Fig. 5.40, to the acceleration at the bottom of the periodic foundation, and Sensor 1463 in the frequency domain, are shown in the red curve, and the black dashed curve in the figure is the ratio of acceleration in the Y direction at the top of the steel column, Sensor 1784 in Fig. 5.40, to the acceleration at the bottom of the conventional foundation, Sensor 1458. The excitation frequencies were outside the band gaps when the acceleration at the top of the steel column on the periodic foundation was greater than at the top of the steel column of the conventional foundation. The acceleration ratio of the periodic foundation was less than the conventional foundation from 9.9 Hz-23.62 Hz, 43.21 Hz-48.12 Hz, and 77.51 Hz-99 Hz. (These band gaps are employed for tests and discussed in the following sections.) Again, Fig. 6.64 shows the ratio of the two acceleration ratios. The frequency band gaps appear when the value of the Y axis is less than 1.
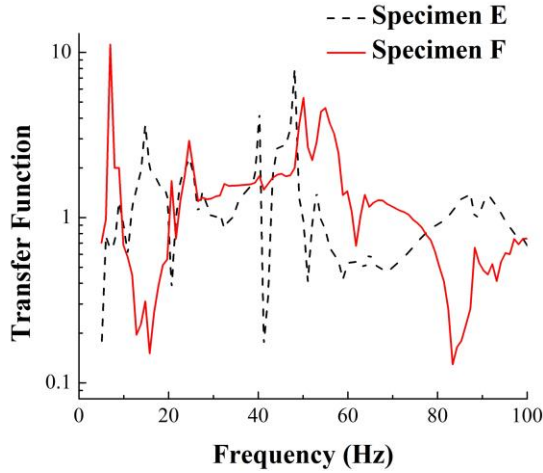
Fig. 6.63 Transfer function between the top of the steel column and RC footing
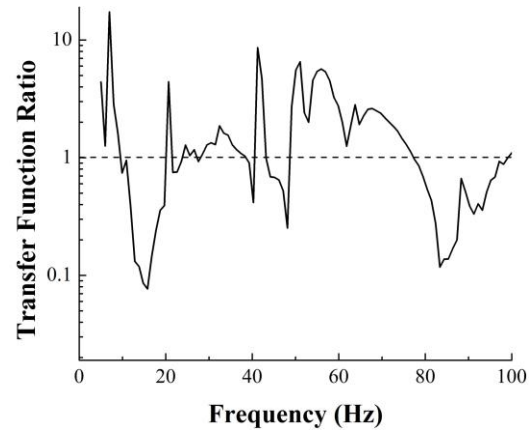
Fig. 6.64 Transfer function ratio of the top of the steel column of the specimens
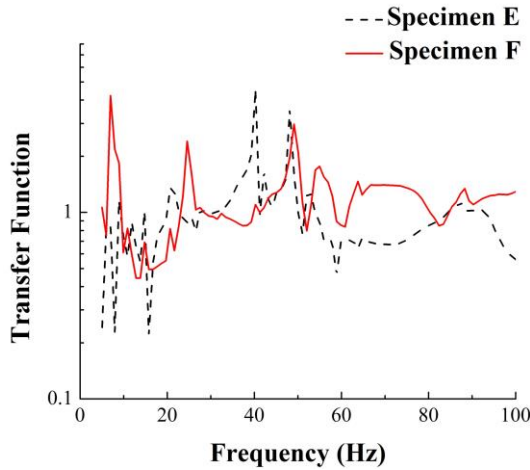
Fig. 6.65 Transfer function between the top of the concrete of periodic foundation and RC footing
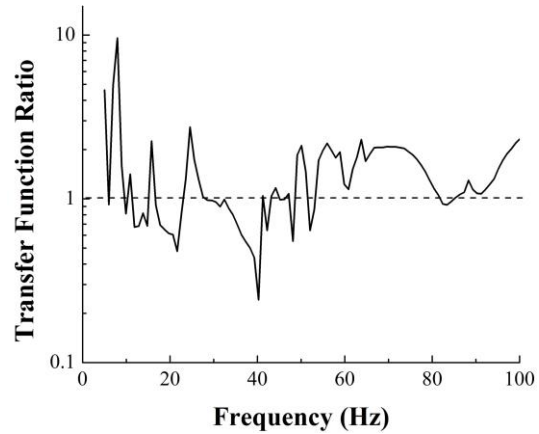
Fig. 6.66 Transfer function ratio of the top of concrete of the specimens

Fig. 6.65 and Fig. 6.66 show the ratio of the acceleration of the concrete at the top and bottom of both specimens E and F. The red curve is the acceleration ratio of concrete between the top, Sensor 1780, and the bottom, Sensor 1463, of the periodic foundation. The black dashed curve shows the acceleration ratio of concrete between the top, Sensor 1461, and the bottom, Sensor 1458, of the conventional founation   in the frequency domain. When the value of the red curve was less than the black dashed curve, the input

146

P wave was mitigated. The ranges of the band gap are 11.86 Hz-14.8 Hz, 16.76 Hz-23.61 Hz, 27.54 Hz-43.21 Hz, 47.13 Hz-48 Hz, 51.5 Hz-53 Hz, and 81.43 Hz-86.33 Hz. Fig. 6.66 shows the ratio of the transfer function of the two specimens.

6.3.2.1.2   Fixed sine P wave results

Harmonic P wave excitation was applied to the specimens, and their frequencies were found to be in the range of the band gaps, i.e., 21.2 Hz, according to the results of the stepped sine tests in Section 6.3.2.1.1. The range of figures, Fig. 6.67 to Fig. 6.69, shows acceleration in the Y direction under a sine P wave of 21.2 Hz. The red curve in Fig. 6.67 is the acceleration at the top of the steel column with the periodic foundation, Sensor 1783. The dashed gray curve is the acceleration response at the top of the steel column with the conventional foundation, Sensor 1784. Fig. 6.67 shows that, at the beginning of the harmonic motion, the two curves have nearly the same peak acceleration owing to the transient effect; when the specimen was in the steady state, the peak acceleration, 0.0479 from Sensor 1783, at the top of the steel column on the periodic foundation, was 63.9% that of the conventional foundation, 0.073g from Sensor 1784. Fig. 6.68 shows the acceleration at the top of the concrete in specimens E and F. The acceleration at the top of the concrete of Specimen F, 0.029g from Sensor 1780, was 51.8% that of Specimen E, 0.056g from Sensor 1461. Fig. 6.69 shows the acceleration in concrete located in the 3rd row from the bottom of the periodic foundation under the harmonic P waves of 21.2 Hz. When the specimen was in the steady state, the peak acceleration, 0.03g from Sensor 1779 at the intersection between the third and fourth unit cells in the periodic foundation, to be 60% of the conventional foundation, 0.05g from Sensor 1459.

147
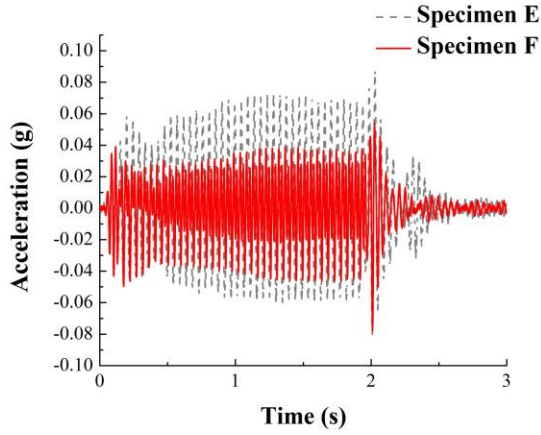
Fig. 6.67 Acceleration at the top of the steel
column in specimens E and F
at the frequency of 21.2Hz
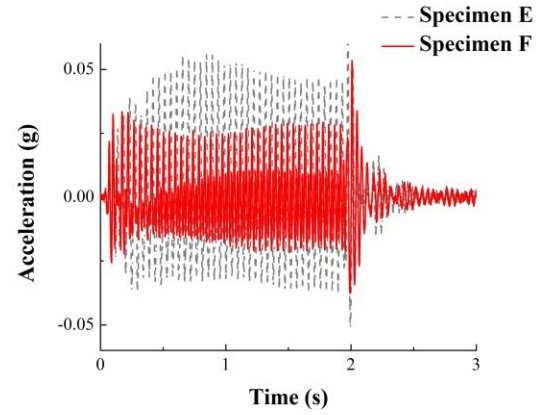
Fig. 6.68 Acceleration at the top of concrete
in specimens E and F
at the frequency of 21.2Hz
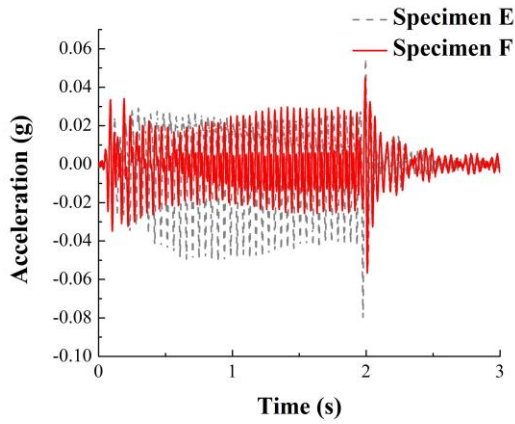
Fig. 6.69 Acceleration in middle of
concrete in specimens E and F at the
frequency of 21.2Hz
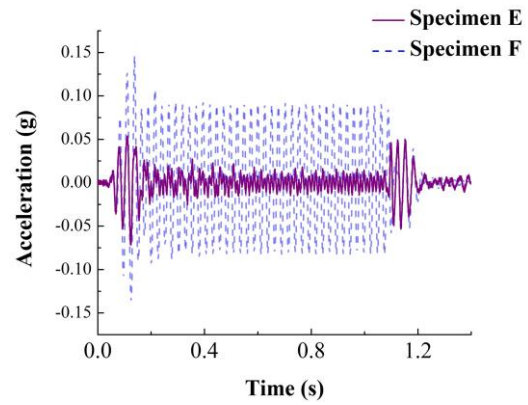
Fig. 6.70 Acceleration at the top of the
steel column in specimens E and F at the
frequency of 38.9Hz

Fig. 6.70 shows the acceleration at the top of the steel column under a harmonic P wave with a frequency of 38.9 Hz, which is located outside the band gaps. The acceleration at the top of the steel column with a periodic foundation was amplified.

6.3.2.1.3 Seismic P wave results
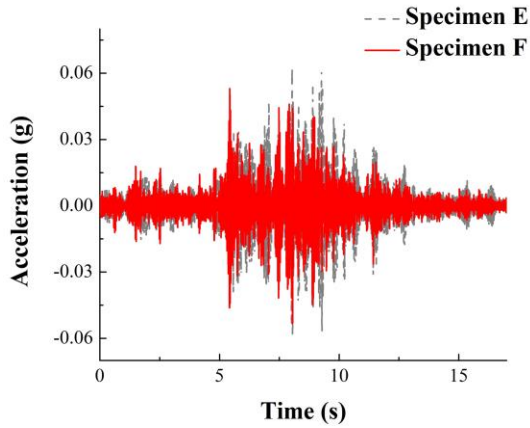
Fig. 6.71 Acceleration at the top of the steel column in specimens E and F at Borapeak090 with a main frequency of 21.2Hz
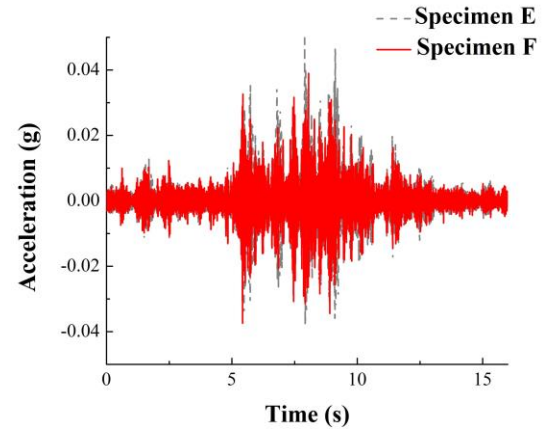
Fig. 6.72 Acceleration at the top of the concrete in specimens E and F at Borapeak090 with a main frequency of 21.2Hz

Modified seismograms were also used to verify the band gap effect. The seismogram, BORAH.AS/HAU090 (1983/10/29) with a main frequency of 18.1 Hz was modified to cause the main frequency to fall into the band gaps, i.e., 21.2 Hz. The vertical acceleration at the top of the steel column on both the periodic and conventional foundations are shown in Fig. 6.71 under the modified seismogram BORAH.AS/HAU090 with a main frequency of 21.2 Hz. Fig. 6.71 shows that the peak vertical acceleration at the top of the steel column on the periodic foundation, Sensor 1783, was reduced by 14.8% as compared to the conventional foundation, Sensor 1784. The peak acceleration of Sensor 1783 on Specimen F was 0.053g, and the peak acceleration of Sensor 1784 on Specimen E was 0.062g. Fig. 6.72 shows the responses at the top of the concrete for both specimens E and F under the same seismogram; the peak acceleration in the vertical direction at the top of the concrete of the periodic foundation, Sensor 1780, was reduced by 22%, as compared to the conventional foundation, Sensor 1461. The peak acceleration of Sensor 1780 on Specimen F was 0.039g, and the peak

149

acceleration of Sensor 1461 on Specimen E was 0.05g. The test results indicate that the periodic foundation was also capable of providing an effective filter to mitigate the vibration in the vertical direction, having frequency contents within the desired band gaps.

6.3.2.2   Use of T-Rex shaker

6.3.2.2.1   Stepped sine P wave results

Fig. 6.73 to Fig. 6.75 show the test results of the stepped sine P wave tests under two different excitation levels. Fig. 6.73 shows the transfer function ratio of the two specimens under 2V and 4.5V excitation levels. The transfer function of Specimen F is the ratio of acceleration in the Y direction at the top of the steel column, Sensor 1783, to the acceleration in the Y direction at the bottom of the periodic foundation, Sensor 1463, in the frequency domain. The transfer function of Specimen E is the ratio of acceleration in Y direction of Sensor 1784 to the acceleration in the Y direction of Sensor 1458. The transfer function amplitude ratio is the ratio of the transfer function of Specimen F to that of Specimen E. The red curve of Fig. 6.73 is the transfer function amplitude ratio on top of the column under 4.5V excitation, and the dashed gray curve represents the transfer function amplitude ratio on top of the column under 2V excitation. The attenuation zones of the red curve under 4.5V excitation range from 14.2 Hz-23.1 Hz, 72.8 Hz-82.8 Hz, and 88.1 Hz-100 Hz. The attenuation zones of the gray curve under 2V excitation range from 15.3 Hz-23.1 Hz and 72.3 Hz-91.9 Hz. The two results were very close.

Fig. 6.74 shows the transfer function on top of the concrete of Specimen F under different excitation levels. The transfer function is the acceleration ratio on top of the concrete, Sensor 1780, to the acceleration on top of the RC footing, Sensor 1463. The

output on top of the concrete was smaller than the input when the transfer function was less than 1. Under 4.5V excitation, the output on the concrete was less than the input in the frequency ranges 9.8 Hz-21.2 Hz, 26.5 Hz-38.9 Hz, 48 Hz-60.5 Hz, and 89.5 Hz-100 Hz. Under 2V excitation, the ranges are 9.8 Hz-21.23 Hz, 26.5 Hz-39.8 Hz, and 55.6 Hz-79.5 Hz. Fig. 6.75 is the transfer function amplitude ratio on top of the concrete of the two specimens under 2V and 4.5V excitation levels. Specimen E experienced a higher level in the frequency ranges of 16.5 Hz-23.1 Hz and 48.4 Hz-60 Hz.
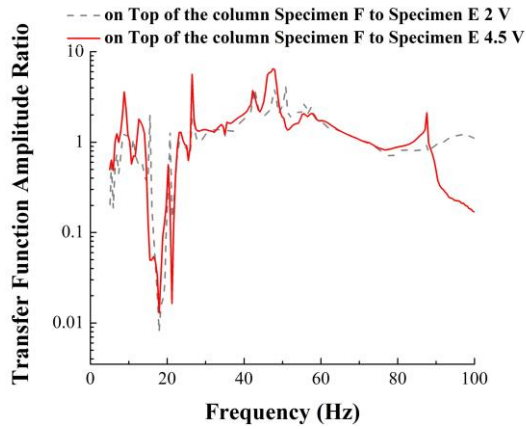
Fig. 6.73 Transfer function amplitude ratio on top of the column under 2V and 4.5V excitation
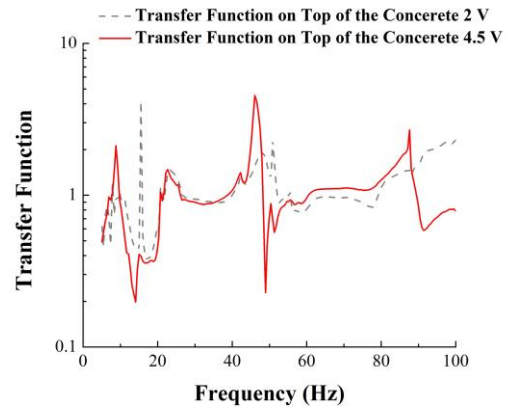
Fig. 6.74 Transfer function on top of the concrete of Specimen F under 2V and 4.5V excitation
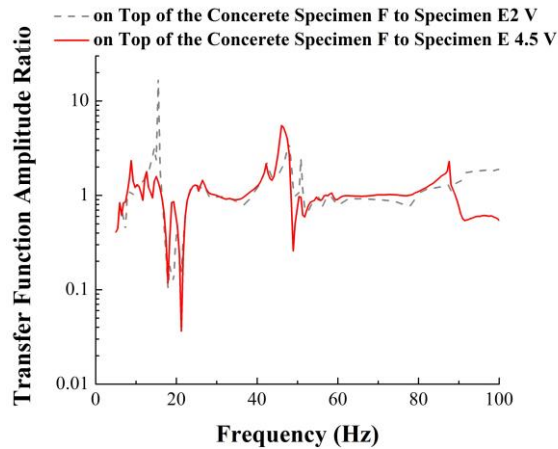
Fig. 6.75 Transfer function amplitude ratio on top of the concrete under 2V and 4.5V excitation

The test results show that, although they are under different excitation levels, the attenuation zones under the P waves were basically the same. Attenuation zones are affected by properties defined by material and geometric attributes rather than the magnitude of input excitation.

6.3.2.2.2 *Fixed Sine P wave results*

The harmonic P wave excitation was applied to the specimens; their frequencies were found to be in the range of the band gaps, i.e., 21.2 Hz, according to the results of the stepped sine tests described in Section 6.3.2.2.1. Fig. 6.76 to Fig. 6.78 show the accelerations in the Y direction under a fixed sine P wave of 21.2 Hz under 2V excitation. The red curve in Fig. 6.76 is the acceleration at the top of the steel column on the periodic foundation, Sensor 1783. The dashed gray curve is the acceleration response at the top of the steel column on the conventional foundation, Sensor 1784. Fig. 6.76 shows that, at the beginning of the harmonic motion, the two curves have nearly the same peak acceleration owing to the transient effect. When the specimen was in the steady state, the peak acceleration at the top of the steel column on the periodic foundation, Sensor 1783, was 0.034g, and the peak acceleration at the top of the column on the conventional foundation, Sensor 1784, was 0.051g. The peak acceleration in Fig. 6.76 of Specimen F was 66.7% that of Specimen E. Fig. 6.77 shows the acceleration at the top of the concrete in specimens E and F. The peak acceleration, 0.014g from Sensor 1780 at the top of the concrete of Specimen F, was 31.8% that of Specimen E, 0.044g from Sensor 1461. Fig. 6.78 shows the acceleration in concrete located in the 3rd row from the bottom of the periodic foundation under the harmonic P waves with 21.2 Hz under 2V excitation level. When the specimen was in the steady state, the peak acceleration, 0.031g from Sensor

1779, at the intersection of the third and fourth unit cells in the periodic foundation, was
83.8% that of the conventional foundation, 0.037g from Sensor 1459.
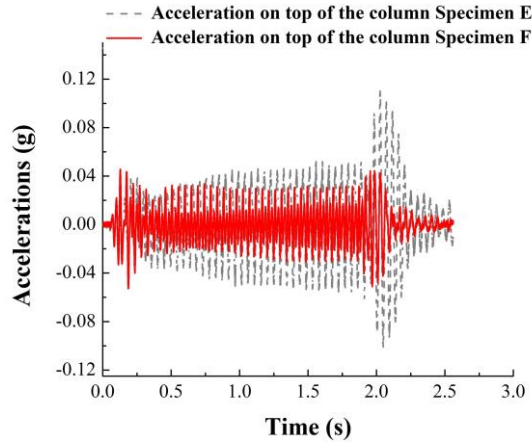
Fig. 6.76 Acceleration on top of the column under 2V fixed sine P wave 21.2 Hz
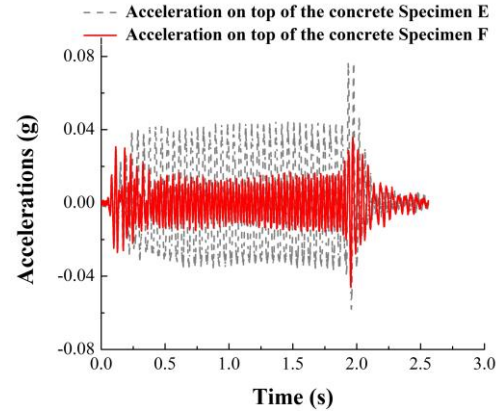
Fig. 6.77 Acceleration on top of the concrete under 2V fixed sine P wave 21.2 Hz
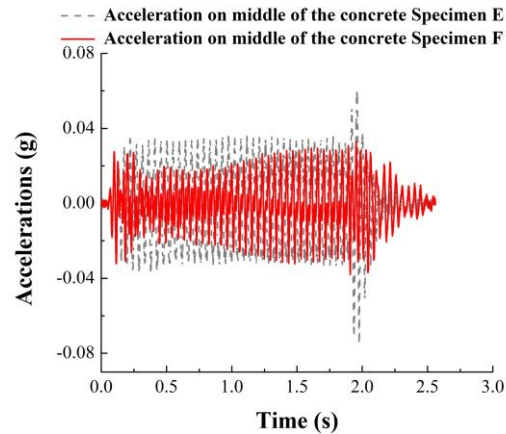
Fig. 6.78 Acceleration on middle of the concrete under 2V fixed sine P wave 21.2 Hz

Another harmonic P wave test with a frequency of 21.2 Hz under 4.5V excitation level was conducted, like the previous P wave tests having a frequency of 21.2 Hz under 2V excitation level. Fig. 6.79 shows acceleration at the tops of the steel columns of both specimens. The red curve is the acceleration at the top of the steel column on the periodic foundation, and the dashed curve is the acceleration at the top of the steel column with

153

the conventional foundation. The peak acceleration of Specimen F was 0.14g in the steady state, and the peak acceleration of Specimen E was 0.22g. The reduction of the peak acceleration was 36.4%. Fig. 6.80 shows acceleration at the top of the concrete; the red curve is the acceleration, with a peak acceleration of 0.11g from Sensor 1780, at the top of the concrete on the periodic foundation, and the gray dashed curve is the acceleration at the top of the concrete on the conventional foundation, with a peak acceleration of 0.13g from Sensor 1461. The acceleration of concrete at the top of the periodic foundation was 84.6% that of the conventional foundation. Fig. 6.81 shows the acceleration in the middle of the concrete, located on the 3rd row of the unit cells from the bottom of the periodic foundation. The peak acceleration of Sensor 1779 on Specimen F was 0.09g, and the peak acceleration of Sensor 1459 was 0.14g. The peak acceleration in the periodic foundation was reduced to 64.3% that of the conventional foundation.

The ratio of peak acceleration on top of the steel column of Specimen F to that of Specimen E under 2V excitation was 66.7%, and the ratio under 4.5V excitation was 63.6%. The comparison of the reduction under the P wave with different excitation levels indicated that the excitation levels had no significant effect on the reduction of acceleration at the top of the steel column.
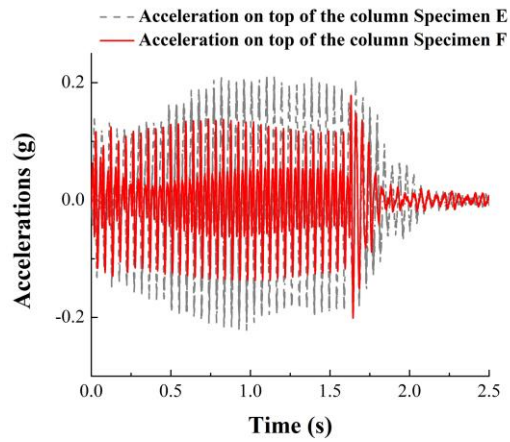
Fig. 6.79 Acceleration on top of the column under 4.5V fixed sine P wave 21.2 Hz
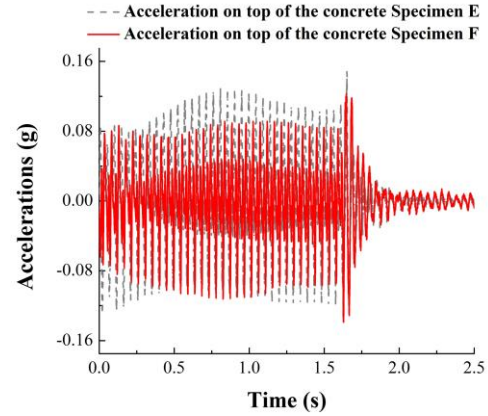
Fig. 6.80 Acceleration on top of the concrete under 4.5V fixed sine P wave 21.2 Hz
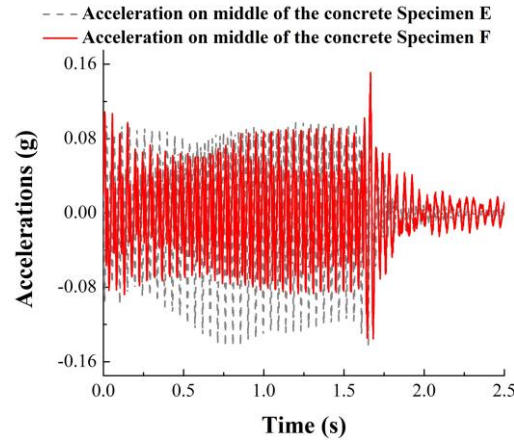
Fig. 6.81 Acceleration on middle of the concrete under 4.5 fixed sine P wave 21.2 Hz

6.3.2.2.3 Seismic P wave results

The modified seismograms were used to verify the band gap effect. The same seismogram, BORAH.AS/HAU000 (1983/10/29), which was used to test the specimens with a main frequency of 17.3 Hz, was modified to make the main frequency fall into the band gaps, i.e., 21.2 Hz. The results of the tests under 2V excitation level are discussed first: Fig. 6.82 shows the vertical accelerations at the top of the steel column on both the periodic and conventional foundations. The peak acceleration of Sensor 1783 on

Specimen F was 0.054g, and the peak acceleration of Sensor 1784 on Specimen E was 0.057g. Fig. 6.82 shows that the peak vertical acceleration at the top of the steel column on the periodic foundation, Sensor 1783, was 95% that of the peak vertical acceleration on the conventional foundation, Sensor 1784. Fig. 6.83 shows the responses at the top of the concrete for both specimens E and F under the same seismogram. The peak acceleration of Sensor 1780 on Specimen F is 0.036g, and the peak acceleration of Sensor 1461 on Specimen E is 0.045g. The peak acceleration in the vertical direction at the top of the concrete for the periodic foundation, Sensor 1780, was 80% that of the peak vertical acceleration of the conventional foundation, Sensor 1461. Fig. 6.84 shows the acceleration on the middle of the concrete under 2V modified BORAH.AS/HAU000 P wave. The peak acceleration on the concrete in the middle of Specimen F, Sensor 1779, is 0.037g, and the peak acceleration of Specimen E is 0.046g. The peak acceleration in the periodic foundation was 80.4% that of the peak acceleration in the conventional foundation.
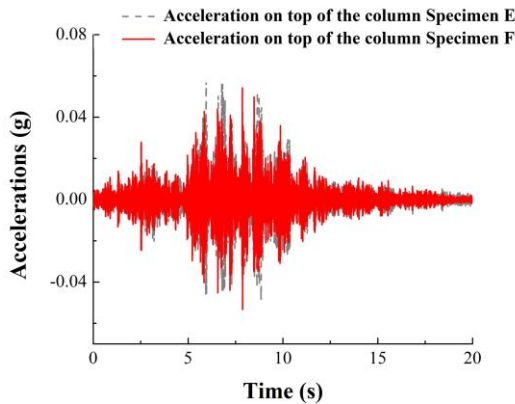
Fig. 6.82 Acceleration on top of the column of the two specimens under 2V modified BORAH.AS/HAU000 P wave
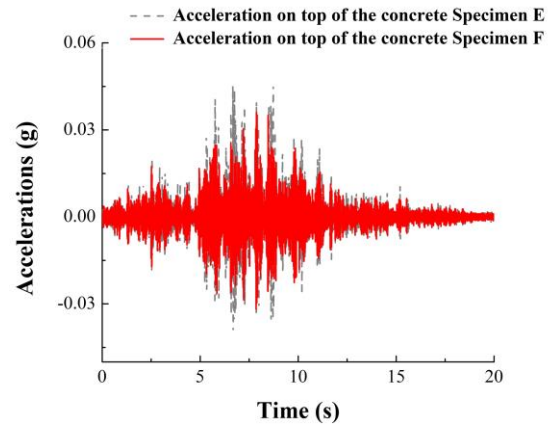
Fig. 6.83 Acceleration on top of the concrete of the two specimens under 2V modified BORAH.AS/HAU000 P wave
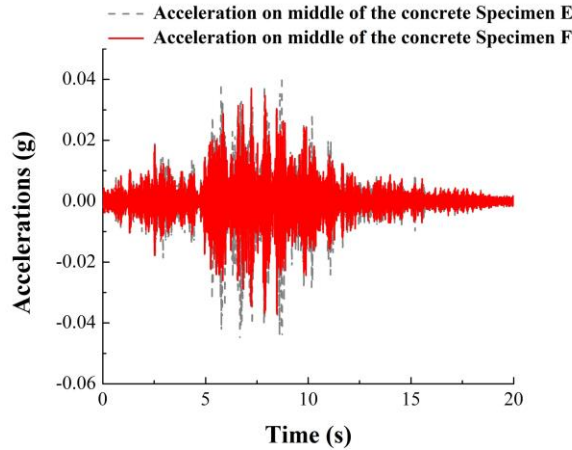
Fig. 6.84 Acceleration on middle of the concrete of the two
specimens under 2V modified BORAH.AS/HAU000 P wave

The test results under 4.5V excitation level of modified BORAH.AS/HAU000 P
wave are discussed next: Fig. 6.85 to Fig. 6.87 show the test results. Fig. 6.85 shows a
comparison of acceleration on top of the steel column of specimens E and F. The gray
dashed curve is the response of Sensor 1784; the peak acceleration of Sensor 1784 is
0.17g. The red curve is the acceleration of Sensor 1783 on top of the steel column of
Specimen F; the peak acceleration of Sensor 1783 is 0.14g, which is 82.3% that of
Specimen E. Fig. 6.86 shows the acceleration on top of the concrete under 4.5V
excitation of modified BORAH.AS/HAU000 P wave. The peak acceleration of Sensor
1461 on top of the concrete in Specimen E was 0.123g. The peak acceleration on top of
the concrete in Specimen F, Sensor 1780, was 0.077g. The peak acceleration of the
periodic foundation was 62.5% of the peak acceleration of the conventional foundation.
Fig. 6.87 shows the acceleration in the middle of the concrete of the two specimens. The
red curve shows that the peak acceleration in the middle of the concrete, Sensor 1779, of
Specimen F was 0.088g, and the gray dashed curve shows the peak acceleration in the
middle of the conventional foundation, Sensor 1459, was 0.12g. The peak acceleration of

157

Specimen F was 73% that of Specimen E. The test results indicate that the periodic foundation was capable of providing an effective filter to mitigate the vibration, having frequency contents within the desired band gaps, irrespective of the excitation levels.
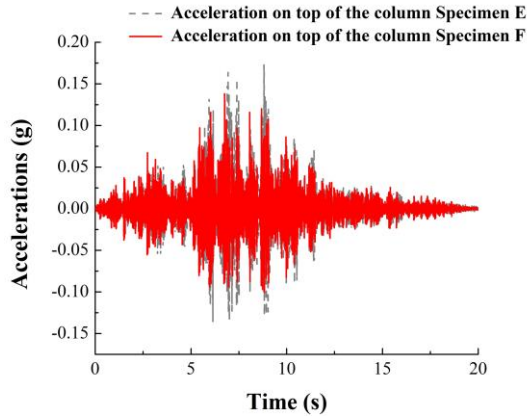
Fig. 6.85 Acceleration on top of the column of the two specimens under 4.5V modified BORAH.AS/HAU000 P wave
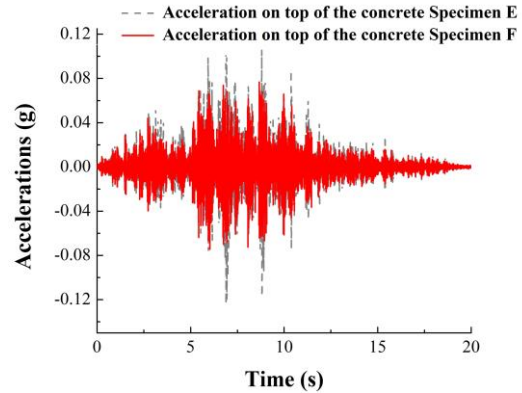
Fig. 6.86 Acceleration on top of the concrete of the two specimens under 4.5V modified BORAH.AS/HAU000 P wave
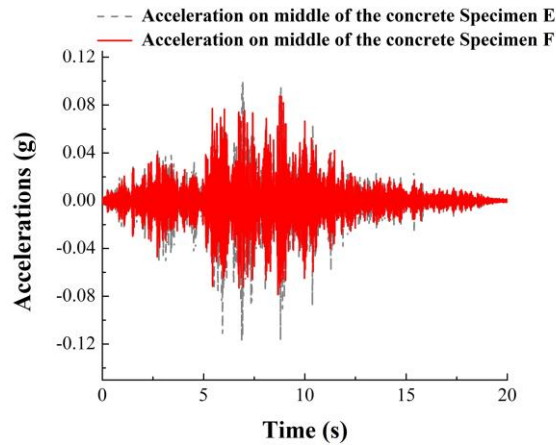
Fig. 6.87 Acceleration on middle of the concrete of the two specimens under 4.5V modified BORAH.AS/HAU000 P wave

7 COMPARISON OF TEST RESULTS AND ANALYTICAL OUTCOMES

The results of basic theory calculation, FEM analysis, and the experimental program are analyzed and compared in this chapter to verify the band gap effects of periodic foundations. The band gaps from basic theory are compared with the attenuation zones from the scanning frequency analysis using ABAQUS for 1D, 2D, and 3D periodic foundations. The scanning frequency analysis outcomes of 2D and 3D periodic foundation are compared with stepped sine test results to verify the attenuation zones of 2D and 3D periodic foundations. Finally, the time history analysis results from FEM are compared with test results of fixed sine tests.

7.1 Comparison of 1D Layered Periodic Foundations

7.1.1 Comparison of theoretical band gaps and attenuation zones for 1D periodic foundations

The band gaps of the 1D layered periodic foundation in both S and P wave excitations were solved based on the theory of solid-state physics. The theoretical solution was based on the assumption that the periodic structures were composed of infinite unit cells. When the periodic structures were applied to the real project, however, the periodic foundation could not be composed of infinite unit cells. The attenuation zones described the band gap effects of the periodic foundation, which were composed of finite unit cells. When the FRF was smaller than zero, the output response of the upper structure was smaller than then input excitation. Theoretically, the band gaps can block the input waves, and attenuation zones cover the frequency ranges of band gaps. Fig. 7.1

shows the attenuation zones of the 1D periodic foundation and the band gaps in S wave excitations. The red curve is the FRF of the node on the top of the frame with the 1D layered periodic foundation in S wave excitation, and the shaded areas are the theoretical band gaps of 1D layered periodic foundation with transverse wave input, as Section 3.1 shows. Fig. 7.2 shows the attenuation zones of the 1D periodic foundation and band gaps in P wave excitation. The red curve is the FRF of the node on the top of the frame with the 1D layered periodic foundation in P wave excitation, and the shaded area is the band gap solved in Section 3.1 with longitudinal wave input. The theoretical band gaps fall into the frequency ranges of attenuation zones.
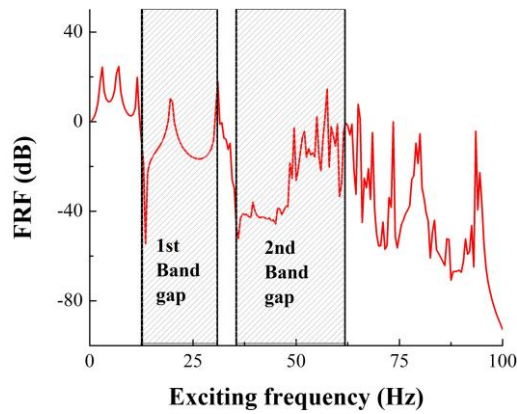
Fig. 7.1 Attenuation zones of 1D periodic foundation and band gaps in S wave excitations
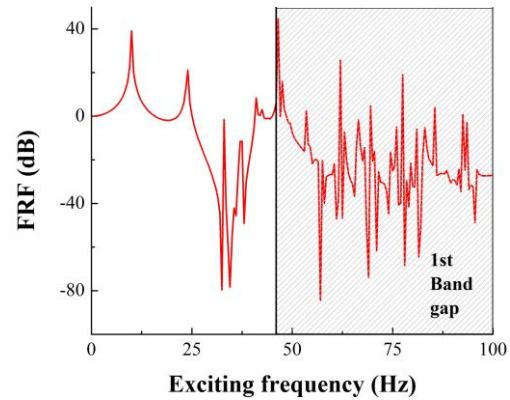
Fig. 7.2 Attenuation zones of 1D periodic foundation and band gaps in P wave excitations

7.1.2 Comparison of time history analysis and test results for the 1D periodic foundations

ABAQUS was used to conduce the time history analysis to simulate the response of the test specimen with seismic wave input. The geometric and material properties were the same as for specimen B in Section 5.1.1.The element types and constraints of the model were the same as described in Section 4.1.2. Three steps were required to perform

the time history analysis: In the first step, the frequency analysis was conducted to find the natural frequency of the model. The first two natural frequencies of the model were 2.836 Hz and 3.614 Hz. Next, the gravity force was applied to the model in a vertical direction. The displacements in the X, Y, and Z directions, and the rotations with respect to the X, Y, and Z axes, were fixed. Finally, the fixed displacement in a horizontal direction was set free, and the 1975 Oroville earthquake records OROVILLE/D-DWR180 with 200% scaled PGA was applied in the horizontal direction. The acceleration of the node on top of the frame was recorded.

Rayleigh damping was applied in analysis to the material properties: α is mass proportional damping; β is stiffness proportional damping. Mass proportional damping dominates when the frequency is low, and stiffness proportional damping dominates when the frequency is high. Eqs. (7-1) and (7-2) show how to find α and β.

$$\alpha = \varsigma \frac{2w_i w_j}{w_i + w_j} \tag{7-1}$$

$$\beta = \varsigma \frac{2}{w_i + w_j} \tag{7-2}$$

Where ζ is the damping factor defined by material and w_i and w_j are the frequency. In the analysis, w_i and w_j are equal to 2.836 Hz and 3.614 Hz, respectively. The damping factors are shown in Table 7.1.

Table 7.1 Damping factors of 1D periodic foundation analysis

Material	ζ	α	β
Concrete	0.05	0.16	0.0155
Steel	0.02	0.064	0.0062
Rubber	3	9.53	0.93
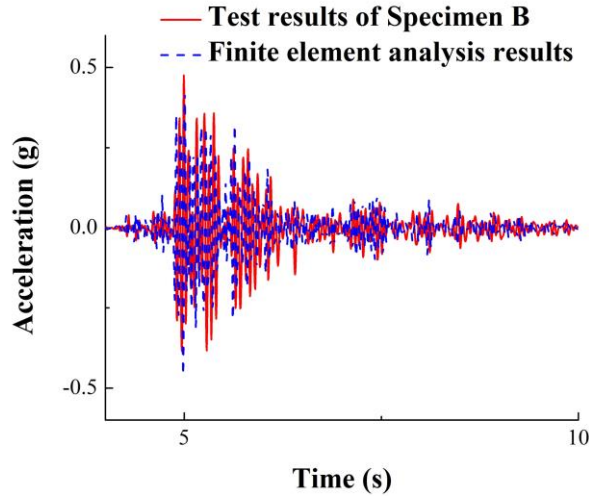
Fig. 7.3 Comparison of test results and FEM
simulation outcomes under 1975 Oroville earthquake

Fig. 7.3 shows acceleration on top of the frame with 1D layered periodic foundation in a horizontal direction. The red solid curve shows the test results of Specimen B under 1975 Oroville earthquake excitation. The dashed blue curve shows the ABAQUS simulation outcomes. The solid and dashed curves are very close. The response of 1D layered periodic foundation can be predicted using FEM, and the analysis verifies that the 1D periodic foundation is an effective way to reduce seismic waves.

7.2 Comparison of 2D Periodic Foundations

7.2.1 Comparison of theoretical band gaps and attenuation zones for the 2D periodic foundations

Fig. 7.4 shows the comparison of attenuation zones and the first band gap of the 2D periodic foundation in S wave excitation. The red curve is the FRF of the node on top of the frame with 2D periodic foundation, which is the same as the FRF in Fig. 4.26. The first band gap shows the same solution as Fig. 3.6. Fig. 7.5 shows the comparison of the attenuation zones and the first band gap of the 2D periodic foundation in P wave

162

excitation. The FRF in Fig. 4.28 is the same as that in Fig. 7.5. The frequency ranges of the first band gap are shown as attenuation zones in both Fig. 7.4 and Fig. 7.5.

The attenuation zones of the 2D periodic foundation with S wave excitation are different from those with P wave excitation. The theoretical solution of band gaps, however, is the same in both S and P wave excitation, which means both S and P waves can be blocked when the wave frequency falls in the frequency ranges of band gaps.

Fig. 7.4 Attenuation zones of 2D periodic foundation and band gaps in S wave excitations

Fig. 7.5 Attenuation zones of 2D periodic foundation and band gaps in P wave excitations

7.2.2 Comparison of scanning frequency analysis and the test results for 2D periodic foundations

The results from the fixed sine wave tests and the seismic tests show that the periodic foundation can reduce the response of the steel frame significantly when the frequencies of excitation S wave frequency fall into the band gaps. The stepped sine wave tests show that the frequency band gaps are in the ranges of 40 Hz-84 Hz and 86 Hz-93 Hz, as shown in Fig. 6.8 to Fig. 6.10. The analytical results in Fig. 4.26 shows the band gaps of the periodic foundation under the S wave are in the ranges of 40 Hz-42.5

Hz, 43 Hz-84.5 Hz, and 86 Hz-100 Hz. The experimental results agree largely with the FEA results.

According to the FEM analysis, the band gaps of the periodic foundation fall within the fundamental frequency of the upper steel frame; therefore, they will avoid resonance at the fundamental frequency. The harmonic tests show that the periodic foundation can block the S wave in a specified frequency. The band gaps of the periodic foundation, therefore, can be designed to match the fundamental frequency of the upper structure.
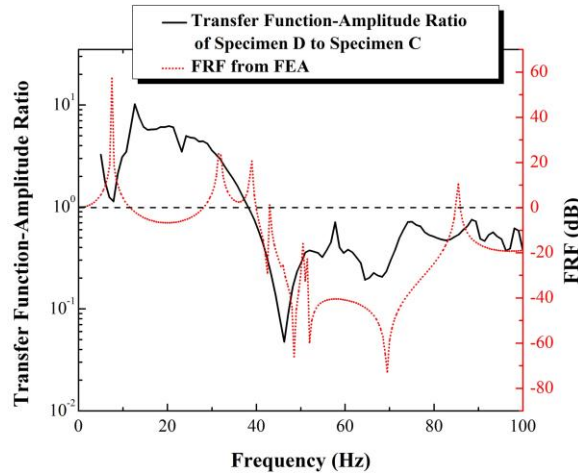
Fig. 7.6 Comparison of test results and FEA
outcomes in S wave excitations

According to the FEA, the attenuation zones of P wave excitations are 30 Hz-50 Hz and 52 Hz-100 Hz, while the results from the field tests are 23.6 Hz-55.0 Hz and 69.7 Hz-85.4 Hz; the comparison is shown in Fig. 7.7. There are several reasons to cause the discrepancies. First, the constitutive model of rubber is not linear, and it is a very sensitive parameter for the band gaps. When the P wave is applied to the specimens, the self-weight and the vibration of the core cylinders affect the strain of the rubber, which

will lead to different Young's modulus of the rubber. According to the compression tests of rubber, with an increase of the deformation, the Young's modulus of the rubber increases. Second, the specimen was rocking during the vibration. Although an I-beam and an angle steel beam connected the two specimens, rocking still existed. The accelerations in the Y direction were affected.

Fig. 7.7 Comparison of test results and FEA
outcomes in P wave excitations

7.2.3 Comparison of time history analysis and test results for the 2D periodic foundations

The time history analysis of the 2D periodic foundation with upper structure was performed to compare with test results of the fixed sine and seismic tests. Fig. 7.8 shows the comparison of test results and FEA outcomes in S wave with the 46 Hz S wave. The red line shows the acceleration on top of Specimen D in S wave with 46 Hz excitation in the steady state, which is the same red curve as in Fig. 6.19. The blue curve shows the FEA results using ABAQUS. The first two natural frequencies of the 2D periodic foundation with upper structure are 0.911 Hz and 5.297 Hz. Rayleigh damping factors

were applied to the materials, the same as was done in Section 7.1.2. Fig. 7.9 shows the comparison of test results and FEA outcomes in S wave with BORAH.AS/HAU000. The red solid curve is acceleration in the horizontal direction with modified BORAH.AS/HAU000, which is the same as the red curve in Fig. 6.21. The blue dashed curve is the acceleration from FEA using ABAQUS. Fig. 7.8 and Fig. 7.9 show that the FEA results are consistent with the test results.

Fig. 7.8 Comparison of test results and FEA outcomes in S wave with 46Hz excitation
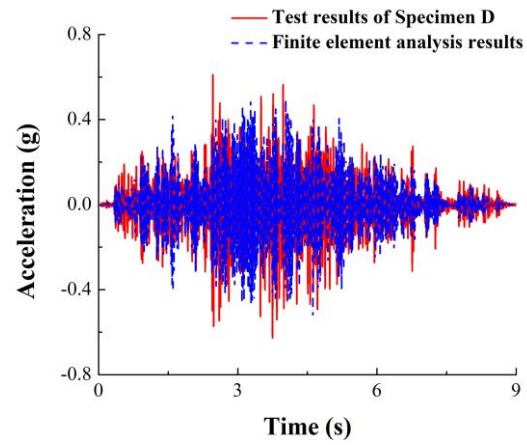
Fig. 7.9 Comparison of test results and FEA outcomes in S wave with BORAH.AS/HAU000

7.3   Comparison of the 3D Periodic Foundations

7.3.1   Comparison of theoretical band gaps and attenuation zones for the 3D periodic foundations

Fig. 7.10 and Fig. 7.11 show the comparison of theoretical band gaps and attenuation zones of the 3D periodic foundation. The shaded areas in the two figures are the theoretical band gaps, which are the same as seen in Fig. 3.8. The theory is based on the assumption that the unit cells are infinite in three directions; therefore, both S and P

166

waves falling into theoretical band gaps can be blocked in three directions. Fig. 7.10 and Fig. 7.11 show that the conclusion reached is that the attenuation zones have greater frequency ranges than theoretical band gaps.
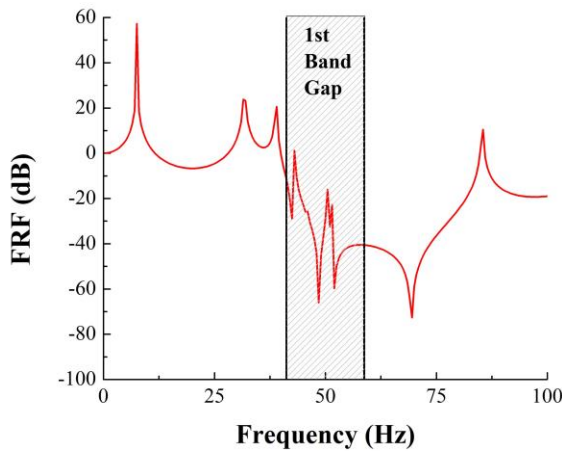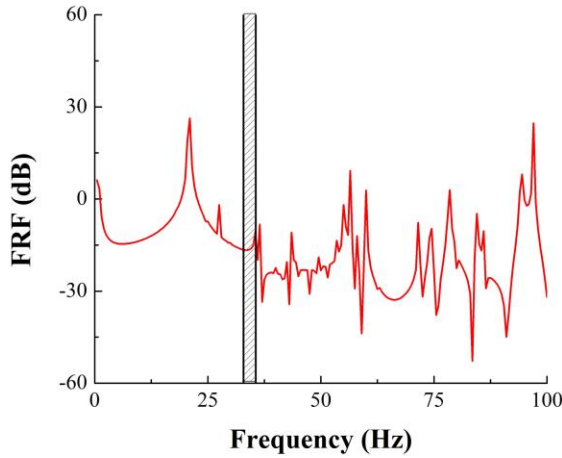

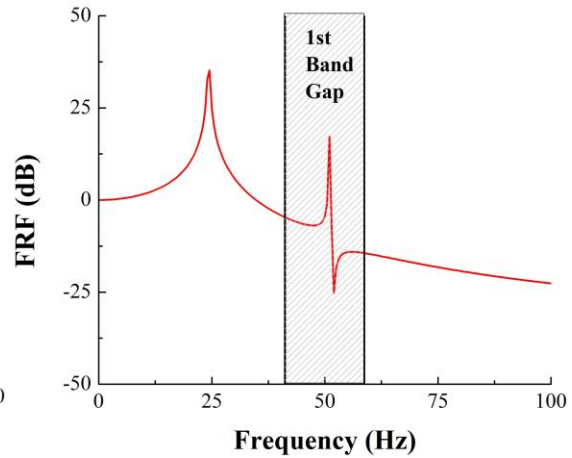Fig. 7.10 Attenuation zones of 3D periodic foundation and band gaps in S wave excitation
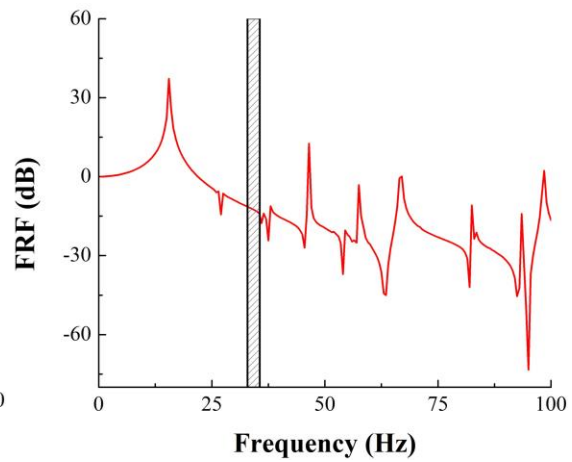
Fig. 7.11 Attenuation zones of 3D periodic foundation and band gaps in P wave excitation

7.3.2 Comparison of scanning frequency analysis and test results for the 3D periodic foundations

Fig. 7.12 shows the experimental amplitude ratio of the transfer functions and the results of the finite element simulation. The red curve in Fig. 7.12 represents the experimental transfer function between the top of the steel column and RC footing of Specimen F. The black dashed curve shows the acceleration ratio between the top of the steel column and the bottom of the periodic foundation in the scanning frequency analysis using ABAQUS. The stepped sine wave test in Section 6.3.1.1.1 shows that the acceleration on the top of the steel column on Specimen F was reduced owing to the periodic foundation when the excitation frequencies were in the ranges of 5 Hz-6.43 Hz, 7.39 Hz-7.86 Hz, 8.82 Hz-9.29 Hz, 10.25 Hz-18.84 Hz, 33.17 Hz-40.33 Hz, 41.28 Hz-

167

43.67 Hz, 45.56 Hz-50.35 Hz, 52.74 Hz-87.59 Hz, and 88.54 Hz-100 Hz. The analytical

results in Section 4.2.2 show the attenuation zones of the periodic foundation were in the

ranges of 1.5 Hz-19 Hz, 23 Hz-56 Hz, 57 Hz-59.5 Hz, 60.5 Hz-78 Hz, 79 Hz-93.5 Hz, 95

Hz-96 Hz, and 97.5 Hz-100 Hz. When the curves were under the blue dashed line, the S

wave was mitigated owing to the periodic foundation. The trends of the two results agree

reasonably well.
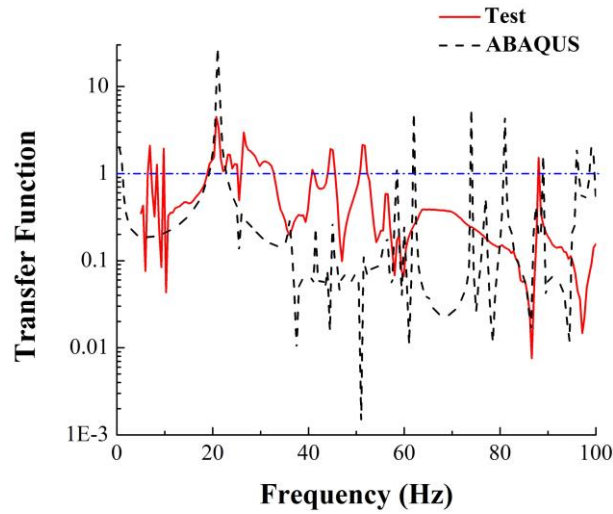
Fig. 7.12 Comparison of test results and FEM
simulation outcomes in S wave excitation

According to finite element analysis, the attenuation zones of P wave excitation

were 22 Hz-46 Hz, 47 Hz-66.5 Hz, 67.5 Hz-98 Hz, and 99 Hz-100 Hz, while the

experimental results from the field tests were 9.9 Hz-23.62 Hz, 43.21 Hz-48.12 Hz, and

77.51 Hz-99 Hz. This comparison is shown in Fig. 7.13. Several reasons may account for

the discrepancies; the most important one is Young's modulus of rubber. The constitutive

model of rubber is not linear, and it is a very sensitive parameter for the band gaps. When

the P wave is applied to the specimens, the self-weight and the vibration of the core cubes

affect the strain of the rubber, which will lead to a different Young's modulus of the

rubber. Compression test results on rubber show that Young's modulus of rubber increases with increasing deformation.
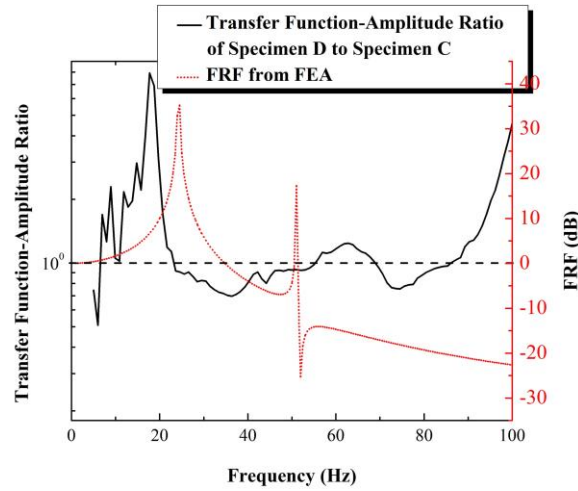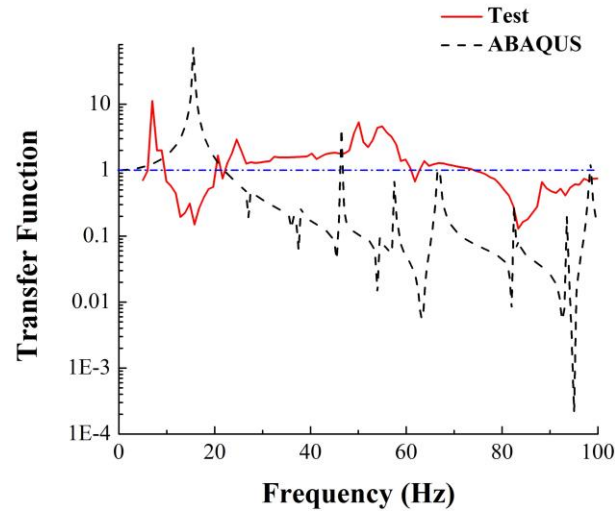

Fig. 7.13 Comparison of test results and FEM
simulation outcomes in P wave excitation

7.3.3 Comparison of time history analysis and test results for the 3D periodic foundations

The time history analysis of the 3D periodic foundation was conducted to compare it with the fixed sine and seismic wave tests. Fig. 7.14 shows the comparison of test results and FEM simulation outcomes in the S wave with 35.1 Hz excitation. The red curve is the acceleration on the top of the frame with the 3D periodic foundation, which is the red curve in Fig. 6.38. The blue curve shows the FEM results. Fig. 7.15 is the comparison of test results and FEM simulation outcomes with modified BORAH.AS/HAU090 excitation. The red curve is the test results shown in Fig. 6.42, and the blue dashed curve is the FEM results. The FEM analysis outcomes are very close to the test results.
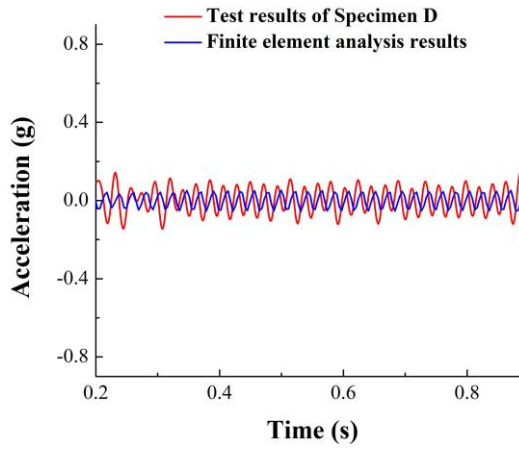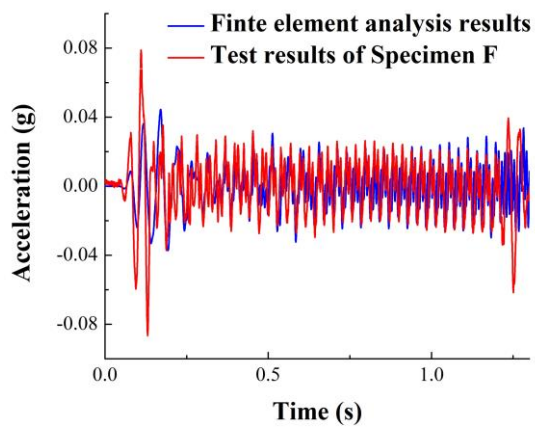
Fig. 7.14 Comparison of test results and FEM simulation outcomes in S wave with 35.1Hz excitation
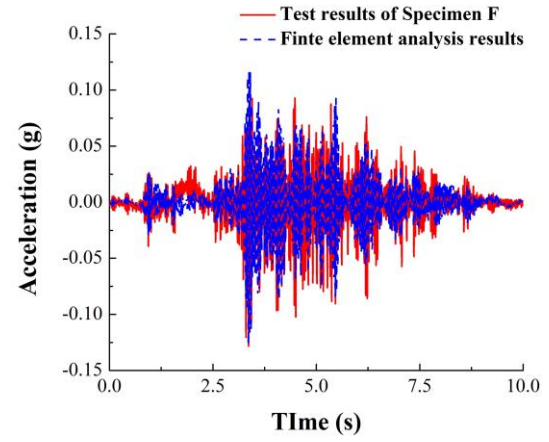
Fig. 7.15 Comparison of test results and FEM simulation outcomes with modified BORAH.AS/HAU090 excitation

8 CONCLUSIONS AND SUGGESTIONS

8.1 Conclusions

The purpose of this research was to develop periodic foundations that mitigate or change the pattern of earthquake energy before it reaches the foundation of structural systems. The experimental programs were conducted to verify the band gap effects of 1D, 2D, and 3D periodic foundations. The following conclusions can be established from this research:

(1) The solutions of frequency band gaps for 1D, 2D, and 3D periodic foundations were obtained based on the theory of solid-state physics. The transfer matrix method, plan wave equation method, and finite domain method can be used to solve the equation of motion to find the theoretical band gaps of periodic foundations.

(2) FEM is an easy way to conduct the parametric studies and design the test specimens for experimental programs on 1D, 2D, and 3D periodic foundations. Both geometric and material properties were found to affect the band gaps of periodic materials. Attenuation zones of the periodic foundation with the upper structure can be found using scanning frequency analysis in ABAQUS.

(3) The feasibility of 1D, 2D, and 3D periodic foundations for structural vibration isolation was verified experimentally. Shake table tests on the 1D periodic foundation were conducted, including ambient vibration, seismogram tests, and harmonic tests. Field tests were performed on the 2D and 3D periodic foundations. The stepped sine, fixed sine, and seismic tests were performed to prove band gap effects.

(4) The test data showed that, when the main frequency of input wave falls into the attenuation zones, the response of the upper structure can be reduced as compared to the same structure without the periodic foundation. With different excitation levels, the reductions of response on top of the column with the 3D periodic foundation are close.

(5) The FEA was conducted to compare with the test results in both the frequency and time domains. The scanning frequency analysis was compared to the stepped sine tests to find the attenuation zones; the time history analysis was compared to the fixed sine and seismic tests. The FEA outcomes were close to the test results. FEM is an effective way to predict the responses of periodic foundations.

8.2 Suggestions

The seismic isolation system based on periodic material is a new idea. Future research in this area is suggested:

(1) Find wider and lower band gaps for seismic resistance; more factors need to be considered, including topology of the unit cells, shape of core density, different types of coating layer.

(2) Suggest nonlinear material properties of periodic foundations be studied. Until now, only linear material properties have been considered based on the theory of periodic structures, but the materials used for periodic foundations, i.e., rubber and reinforced concrete, may have nonlinear behavior during earthquakes.

(3) A procedure is suggested as a way of studying design band gaps and bearing capacity of periodic foundations that could lead to their design for different structures.

(4) An easy and cost-effective manufacturing procedure needs to be developed for further application in construction projects.

9 REFERENCES

[1]   Thomas, E. L., Gorishnyy, T., & Maldovan, M. (2006). Phononics: Colloidal crystals go hypersonic. *Nature Materials*, *5*(10), 773-774.

[2]   Kelly, J. M. (1991). Base Isolation: Origins and Development. *EERC News*, 12(1), 1-3.

[3]   See http://nees.buffalo.edu/seesl/a17.html for testing of elastomeric bearings.

[4]   Kelly, J. M., & Naeim, F. (1999). Design of seismic isolated structures: From theory to practice. *Nueva York, John Wiley & Sons*.

[5]   Sayani, P. J., & Ryan, K. L. (2009). Evaluation of approaches to characterize seismic isolation systems for design. *Journal of Earthquake Engineering*, *13*(6), 835-851.

[6]   Fulin, Z., Ping, Y., Qiaolin, X., Xiangyun, H., & Zhen, Y. (2006). Research and application of seismic isolation system for building structures. *Journal of Architecture and Civil Engineering*, *23*(2), 1-8.

[7]   Wilde, K., Gardoni, P., & Fujino, Y. (2000). Base isolation system with shape memory alloy device for elevated highway bridges. *Engineering Structures*, *22*(3), 222-229.

[8]   Kelly, J. M. (1986). Aseismic base isolation: review and bibliography. *Soil Dynamics and Earthquake Engineering*, *5*(4), 202-216.

[9]   Zhou, F. L., Yang, Z., Liu, W. G., & Tan, P. (2004). New seismic isolation system for irregular structure with the largest isolation building area in the world. In *13th World Conference on Earthquake Engineering*.

[10]   Yang, Y.B., Lee, T.Y., Tsai, L.C. (1990). Response of multi-degree-of-freedom structures with sliding supports. *Earthquake Engineering and Structural Dynamics*, 19(5) 739-752.

[11]   Nanda, R. P., Agarwal, P., & Shrikhande, M. (2012). Base isolation system suitable for masonry buildings. *Asian Journal of Civil Engineering (Building and Housing)*, *13*(2), 195-202.

[12]   Su, L., Ahmadi, G., & Tadjbakhsh, I. G. (1991). Performance of sliding resilient-friction base-isolation system. *Journal of Structural Engineering*, *117*(1), 165-181.

[13]   Mostaghel, N., & Khodaverdian, M. (1987). Dynamics of resilient-friction base isolator (R-FBI). *Earthquake Engineering & Structural Dynamics*, *15*(3), 379-390.

[14]   Su, L., Ahmadi, G., & Tadjbakhsh, I. G. (1991). Performance of sliding resilient-friction base-isolation system. *Journal of Structural Engineering*, *117*(1), 165-181.

[15]   Kawamura, S., Kitazawa, K., Hisano, M., & Nagashima, I. (1988). Study of a sliding-type base isolation system. System composition and element properties. In *9th. WCEE*. Japan.

[16]   Komuro, T., Nishikawa, Y., Kimura, Y., & Isshiki, Y. (2005). Development and realization of base isolation system for high-rise buildings. *Journal of Advanced Concrete Technology*, *3*(2), 233-239.

[17]   Mokha, A., Constantinou, M. C., Reinhorn, A. M., & Zayas, V. A. (1991). Experimental study of friction-pendulum isolation system. *Journal of Structural Engineering*, *117*(4), 1201-1217.

[18]   See   http://www.earthquakeprotection.com/benicia_martinez_bridge.html   for Benicia-Martinez Bridge Retrofit, California.

[19]   Jangid, R. S., & Londhe, Y. B. (1998). Effectiveness of elliptical rolling rods for base isolation. *Journal of Structural Engineering*, *124*(4), 469-472.

[20]   Nagarajaiah, S., Riley, M. A., & Reinhorn, A. (1993). Control of sliding-isolated bridge with absolute acceleration feedback. *Journal of Engineering Mechanics*, *119*(11), 2317-2332.

[21]   Schmitendorf, W. E., Jabbari, F., & Yang, J. N. (1994). Robust control techniques for buildings under earthquake excitation. *Earthquake Engineering & Structural Dynamics*, *23*(5), 539-552.

[22]   Yang, J. N., Wu, J. C., Reinhorn, A. M., & Riley, M. (1996). Control of sliding-isolated buildings using sliding-mode control. *Journal of Structural Engineering*, *122*(2), 179-186.

[23]   Chang, C. M., & Spencer, B. F. (2010). Active base isolation of buildings subjected to seismic excitations. *Earthquake Engineering & Structural Dynamics*, *39*(13), 1493-1512.

[24]   Mehrparvar, B., & Khoshnoudian, T. (2012). Performance-based semi-active control algorithm for protecting base isolated buildings from near-fault earthquakes. *Earthquake Engineering and Engineering Vibration*, *11*(1), 43-55.

[25]   Chu, S.Y., Soong, T.T. and Reinhorn, A.M. (2005). *Active, Hybrid, and Semi-active Structural Control, A Design and Implementation Handbook*, John Wiley & Sons: New York, USA.

[26]   Kittel, C. (2005). *Introduction to solid state physics* (8th edition). New York: Wiley.

[27]   Liu, Z., Zhang, X., Mao, Y., Zhu, Y. Y., Yang, Z., Chan, C. T., & Sheng, P. (2000). Locally resonant sonic materials. *Science*, *289*(5485), 1734-1736.

[28]   Xiao, W., Zeng, G. W., & Cheng, Y. S. (2008). Flexural vibration band gaps in a thin plate containing a periodic array of hemmed discs. *Applied Acoustics*, *69*(3), 255-261.

[29]   Maldovan, M. (2013). Sound and heat revolutions in phononics. *Nature*, *503*(7475), 209-217.

[30]   Thomas, E. L., Gorishnyy, T., & Maldovan, M. (2006). Phononics: Colloidal crystals go hypersonic. *Nature Materials*, *5*(10), 773-774.

[31]   Torres, M., & Montero de Espinosa, F. R. (2004). Ultrasonic band gaps and negative refraction. *Ultrasonics*, *42*(1), 787-790.

[32]   Sigalas, M. M., & Economou, E. N. (1992). Elastic and acoustic wave band structure. *Journal of Sound and Vibration*, *158*(2), 377-382.

[33]   Kushwaha, M. S., Halevi, P., Dobrzynski, L., & Djafari-Rouhani, B. (1993). Acoustic band structure of periodic elastic composites. *Physical Review Letters*, *71*(13), 2022-2025.

[34]   Kushwaha, M. S., Halevi, P., Martinez, G., Dobrzynski, L., & Djafari-Rouhani, B. (1994). Theory of acoustic band structure of periodic elastic composites. *Physical Review B*, *49*(4), 2313.

[35]   Gorishnyy, T., Maldovan, M., Ullal, C., & Thomas, E. (2005). Sound ideas. *Phys. World*, *18*(12), 24-29.

[36]   Liu, Z., Chan, C. T., & Sheng, P. (2002). Three-component elastic wave band-gap material. *Physical Review B*, *65*(16), 165116.

[37]   Zhang, X., Liu, Y., Wu, F., & Liu, Z. (2003). Large two-dimensional band gaps in three-component phononic crystals. *Physics Letters A*, *317*(1), 144-149.

[38]   Liu, Z., Chan, C. T., & Sheng, P. (2005). Analytic model of phononic crystals with local resonances. *Physical Review B*, *71*(1), 014103.

[39]   Goffaux, C., & Sánchez-Dehesa, J. (2003). Two-dimensional phononic crystals studied using a variational method: Application to lattices of locally resonant materials. *Physical Review B*, *67*(14), 144301.

[40]   Goffaux, C., Sánchez-Dehesa, J., Yeyati, A. L., Lambin, P., Khelif, A., Vasseur, J. O., & Djafari-Rouhani, B. (2002). Evidence of fano-like interference phenomena in locally resonant materials. *Physical Review Ltters*, *88*(22), 225502.

[41]   Goffaux, C., Sánchez-Dehesa, J., & Lambin, P. (2004). Comparison of the sound attenuation efficiency of locally resonant materials and elastic band-gap structures. *Physical Review B*, *70*(18), 184302.

[42]   Ho, K. M., Cheng, C. K., Yang, Z., Zhang, X. X., & Sheng, P. (2003). Broadband locally resonant sonic shields. *Applied Physics Letters*, *83*(26), 5566-5568.

[43]   Zhang, S., Hua, J., & Cheng, Jian-Chun. (2003). Experimental and theoretical evidence for the existence of broad forbidden gaps in the three-component composite. *Chinese Physics Letters*, *20*(8), 1303.

[44]   Zhang, S., & Cheng, J. (2003). Existence of broad acoustic band gaps in three-component composite. *Physical Review B*, *68*(24), 245101.

[45]   Hirsekorn, M. (2004). Small-size sonic crystals with strong attenuation bands in the audible frequency range. *Applied Physics Letters*, *84*(17), 3364-3366.

[46]   Hirsekorn, M., Delsanto, P. P., Batra, N. K., & Matic, P. (2004). Modelling and simulation of acoustic wave propagation in locally resonant sonic materials. *Ultrasonics*, *42*(1), 231-235.

[47]   Wang, G., Wen, X., Wen, J., Shao, L., & Liu, Y. (2004). Two-dimensional locally resonant phononic crystals with binary structures. *Physical Review Letters*, *93*(15), 154302.

[48]   Gang, W., Yao-Zong, L., Ji-Hong, W., & Dian-Long, Y. (2006). Formation mechanism of the low-frequency locally resonant band gap in the two-dimensional ternary phononic crystals. *Chinese Physics*, *15*(2), 407.

[49]   Hsu, J. C., & Wu, T. T. (2007). Lamb waves in binary locally resonant phononic plates with two-dimensional lattices. *Applied Physics Letters*, *90*(20), 201904.

[50]   Oudich, M., Li, Y., Assouar, B. M., & Hou, Z. (2010). A sonic band gap based on the locally resonant phononic plates with stubs. *New Journal of Physics*, *12*(8), 083049.

[51]   Oudich, M., Assouar, M. B., & Hou, Z. (2010). Propagation of acoustic waves and wave-guiding in a two-dimensional locally resonant phononic crystal plate. *Applied Physics Letters*, *97*(19), 193503.

[52]   Oudich, M., Senesi, M., Assouar, M. B., Ruzenne, M., Sun, J. H., Vincent, B., Hou, Z. & Wu, T. T. (2011). Experimental evidence of locally resonant sonic band gap in two-dimensional phononic stubbed plates. *Physical Review B*, *84*(16), 165136.

[53]   Sigalas, M. M., & Soukoulis, C. M. (1995). Elastic-wave propagation through disordered and/or absorptive-layered systems. *Physical Review B*, *51*(5), 2780.

[54]   Munjal, M. L. (1993). Response of a multi-layered infinite plate to an oblique plane wave by means of transfer matrices. *Journal of Sound and Vibration*, *162*(2), 333-343.

[55]   Wang, G., Yu, D., Wen, J., Liu, Y., & Wen, X. (2004). One-dimensional phononic crystals with locally resonant structures. *Physics Letters A*, *327*(5), 512-521.

[56]   Chen, A., & Wang, Y. S. (2007). Study on band gaps of elastic waves propagating in one-dimensional disordered phononic crystals. *Physica B: Condensed Matter*, *392*(1), 369-378.

[57]   Han, L., Zhang, Y., Ni, Z. Q., Zhang, Z. M., & Jiang, L. H. (2012). A modified transfer matrix method for the study of the bending vibration band structure in phononic crystal Euler beams. *Physica B: Condensed Matter*, *407*(23), 4579-4583.

[58]   Vasseur, J. O., Djafari-Rouhani, B., Dobrzynski, L., Kushwaha, M. S., & Halevi, P. (1994). Complete acoustic band gaps in periodic fibre reinforced composite materials: the carbon/epoxy composite and some metallic systems. *Journal of Physics: Condensed Matter*, *6*(42), 8759.

[59]   Goffaux, C., & Vigneron, J. P. (2001). Theoretical study of a tunable phononic band gap system. *Physical Review B*, *64*(7), 075118.

[60]   Wu, F., Liu, Z., & Liu, Y. (2002). Acoustic band gaps created by rotating square rods in a two-dimensional lattice. *Physical Review E*, *66*(4), 046628.

[61]   Li, X., Wu, F., Hu, H., Zhong, S., & Liu, Y. (2003). Large acoustic band gaps created by rotating square rods in two-dimensional periodic composites. *Journal of Physics D: Applied Physics*, *36*(1), L15.

[62]   Tanaka, Y., Tomoyasu, Y., & Tamura, S. I. (2000). Band structure of acoustic waves in phononic lattices: Two-dimensional composites with large acoustic mismatch. *Physical Review B*, *62*(11), 7387.

[63]   Hsieh, P. F., Wu, T. T., & Sun, J. H. (2006). Three-dimensional phononic band gap calculations using the FDTD method and a PC cluster system. *Ultrasonics, Ferroelectrics and Frequency Control, IEEE Transactions On*, *53*(1), 148-158.

[64]   Yasumoto, K. (2010). *Electromagnetic theory and applications for photonic crystals*. CRC Press.

[65]   Kurose, T., Tsuruta, K., TOTSUJI, C., & TOTSUJI, H. (2009). FDTD simulations of acoustic waves in two-dimensional phononic crystals using parallel computer. *Memoirs of the Faculty of Engineering, Okayama University*, *43*, 16-21.

[66]   Mei, J., Liu, Z., Shi, J., & Tian, D. (2003). Theory for elastic wave scattering by a two-dimensional periodical array of cylinders: An ideal approach for band-structure calculations. *Physical Review B*, *67*(24), 245107.

[67]   Kafesaki, M., & Economou, E. N. (1999). Multiple-scattering theory for three-dimensional periodic acoustic composites. *Physical Review B*, *60*(17), 11993.

[68]   Psarobas, I. E., Stefanou, N., & Modinos, A. (2000). Scattering of elastic waves by periodic arrays of spherical bodies. *Physical Review B*, *62*(1), 278.

[69]   Liu, Z., Chan, C. T., Sheng, P., Goertzen, A. L., & Page, J. H. (2000). Elastic wave scattering by periodic structures of spherical objects: Theory and experiment. *Physical Review B*, *62*(4), 2446.

[70]   Pennec, Y., Vasseur, J. O., Djafari-Rouhani, B., Dobrzyński, L., & Deymier, P. A. (2010). Two-dimensional phononic crystals: Examples and applications. *Surface Science Reports*, *65*(8), 229-291.

[71]   Wen, J., Wang, G., Yu, D., Zhao, H., & Liu, Y. (2005). Theoretical and experimental investigation of flexural wave propagation in straight beams with periodic structures: Application to a vibration isolation structure. *Journal of Applied Physics*, 97(11), 114907.

[72]   Hussein, M. I., Hulbert, G. M., & Scott, R. A. (2007). Dispersive elastodynamics of 1D banded materials and structures: design. *Journal of Sound and Vibration*, *307*(3), 865-893.

[73]   Xiang, H. J., & Shi, Z. F. (2009). Analysis of flexural vibration band gaps in periodic beams using differential quadrature method. *Computers & Structures*, 87(23), 1559-1566.

[74]   Xiang, H. J., & Shi, Z. F. (2011). Vibration attenuation in periodic composite Timoshenko beams on Pasternak foundation. *Structural Engineering and Mechanics*, *40*(3), 373-392.

[75]   Yu, D., Wen, J., Shen, H., Xiao, Y., & Wen, X. (2012). Propagation of flexural wave in periodic beam on elastic foundations. *Physics Letters A*, *376*(4), 626-630.

[76]   Asiri, S. A., Mohammad, A. S., & Al-Ghamdi, A. S. (2009). Dynamic response of an experimental model for offshore platforms with periodic legs. *Journal of King Abdulaziz University Engineering Sciences*, 20(1), 93-121.

[77]   Asiri, S. A., & AL-Zahrani, Y. Z. (2014). Theoretical analysis of mechanical vibration for offshore platform structures. *World Journal of Mechanics*, *4*, 1.

[78]   Bao, J., Shi, Z., & Xiang, H. (2011). Dynamic responses of a structure with periodic foundations. *Journal of Engineering Mechanics*, *138*(7), 761-769.

[79]   Shi, Z., Cheng, Z., & Xiang, H. (2014). Seismic isolation foundations with effective attenuation zones. *Soil Dynamics and Earthquake Engineering*, *57*, 143-151.

[80]   Cheng, Z. B., & Shi, Z. F. (2014). Multi-mass-spring model and energy transmission of one-dimensional periodic structures. *Ultrasonics, Ferroelectrics and Frequency Control, IEEE Transactions On*, *61*(5), 739-746.

[81]   Jia, G., & Shi, Z. (2010). A new seismic isolation system and its feasibility study. *Earthquake Engineering and Engineering Vibration*, *9*(1), 75-82.

[82]   Xiong, C., Shi, Z., & Xiang, H. (2012). Attenuation of Building Vibration Using Periodic Foundations. *Advances in Structural Engineering*, *15*(8), 1375-1388.

[83]   Cheng, Z., & Shi, Z. (2013). Novel composite periodic structures with attenuation zones. *Engineering Structures*, *56*, 1271-1282.

[84]   Cheng, Z., & Shi, Z. (2014). Vibration attenuation properties of periodic rubber concrete panels. *Construction and Building Materials*, *50*, 257-265.

[85]   Huang, J., & Shi, Z. (2011). Application of periodic theory to rows of piles for horizontal vibration attenuation. *International Journal of Geomechanics*, *13*(2), 132-142.

[86]   Brûlé, S., Javelaud, E. H., Enoch, S., & Guenneau, S. (2014). Experiments on Seismic Metamaterials: Molding Surface Waves. *Physical Review Letters*, *112*(13), 133901.

[87]   Shi, Z., & Huang, J. (2013). Feasibility of reducing three-dimensional wave energy by introducing periodic foundations. *Soil Dynamics and Earthquake Engineering*, *50*, 204-212.

[88]   Xiang, H. J., Shi, Z. F., Wang, S. J., & Mo, Y. L. (2012). Periodic materials-based vibration attenuation in layered foundations: experimental validation. *Smart Materials and Structures*, *21*(11), 112003.

[89]   Landau, L.D., Lifshitz, E.M. (1986). Theory of Elasticity (3rd Edition). *Pergamon Press*, Oxford.

[90]   Wen, X. S., Wen, J. H., Yu, D. L., Wang, G., Liu, Y., & Han, X. (2009). Phononic crystals. National Defense Industry Press, Beijing.

[91]   Kushwaha, M. S., & Djafari-Rouhani, B. (1996). Complete acoustic stop bands for cubic arrays of spherical liquid balloons. *Journal of Applied Physics*, 80(6), 3191-3195.

[92]   Psarobas, I. E., & Sigalas, M. M. (2002). Elastic band gaps in a FCC lattice of mercury spheres in aluminum. *Physical Review B*, 66(5), 052302.

[93]   Sainidou, R., Stefanou, N., & Modinos, A. (2002). Formation of absolute frequency gaps in three-dimensional solid phononic crystals. *Physical Review B*, *66*(21), 212301.

[94]   Zhang, X., Liu, Z., Liu, Y., & Wu, F. (2003). Elastic wave band gaps for three-dimensional phononic crystals with two structural units. *Physics Letters A*, 313(5), 455-460.

[95]   Xiang, H. J., Shi, Z. F., & Bao, J. (2010). Seismic isolation of buildings with a new type of periodic foundations. *ASCE Earth and Space 12th Conference,* Honolulu, HA, 15-17.

[96]   AISC, (2010), Steel Construction Manual, 14th Ed, American Institute of Steel Construction, Chicago, Illinois.

[97]   See <u>PEER Ground Motion Database</u>

[98]   ACI Committee, American Concrete Institute, & International Organization for Standardization. (2008). Building Code Requirements for Structural Concrete (ACI 318-08) and Commentary. American Concrete Institute.

[99]   ASTM Committee. ASTM D575-91 Standard Test Methods for Rubber Properties in Compression.

[100]   Ductile iron society, http://www.ductile.org/didata/Section3/3part1.htm#Modulus of Elasticity.

[101]   See <u>http://nees.utexas.edu/Equipment-T-Rex.shtml</u> for specifications of T-Rex.

[102]   See <u>http://nees.utexas.edu/Equipment-Rattler.shtml</u> for specifications of Rattler.

[103]   See <u>http://nees.utexas.edu/Equipment-Thumper.shtml</u> for specifications of Thumper.

[104]   See <u>http://nees.utexas.edu/Equipment-Raptor.shtml</u> for specifications of Raptor.

[105]   See <u>http://www.mcmaster.com/#standard-rubber-sheets/=og8cw1</u> for hardness of rubber

APPENDIX: DESIGN GUIDELINES FOR PERIODIC FOUNDATIONS

A.1 Design Procedures

The step-by-step procedure to design 2D and 3D periodic foundations is shown below.

Step 1: Assume a mid-gap frequency.

Step 2: Obtain the wave velocity of the matrix material.

Step 3: Calculate the wave length of the matrix material.

Step 4: Select a ratio of the wave length to the unit cell size that should be greater than 300.

Step 5: Calculate the unit cell size.

Step 6: Conduct the parametric study to obtain the dimensions of the core cube and rubber coating.

A.2 Design Example

It is assumed that a low mid-gap frequency in a band gap is 11.5 Hz. The P wave velocity in concrete is 4,500 m/s. The wave length and size of unit cell can be calculated.

$$\text{wave length} = \frac{\text{wave velocity}}{\text{mid-gap frequency}} = \frac{4500\text{m/s}}{11.5\text{Hz}} = 391.3\text{m} \qquad \text{(A-1)}$$

The ratio of the wave length to the size of unit cell is 354, and the reason for this value is shown in Section A.3 Back-up Information. The estimated unit cell size is

$$\text{unit cell size} = \frac{\text{wave length}}{\text{ratio}} = \frac{391.3\text{m}}{354} = 1.1\text{m} \qquad \text{(A- 2)}$$

In other words, when the size of unit cell is 1.1m, a mid-gap frequency of 11.5 Hz can be achieved. The core cube and rubber coating can be designed by a parametric study, as shown in Section 4.3.1.2 of this report.

Verification:

A 3D periodic foundation can be used to verify the design example by Cheng et al.[1] Fig. A.1 shows one unit cell of a 3D periodic foundation. Fig. A.2 shows the dispersion relationship of a coated cube included periodic foundation with a = 1m, b = 0.6m and t = 0.1m. a is the length of the unit cell; b is the size of the core cube and t is the thickness of the rubber wrapping. An absolute band gap is in the region between 9.10 Hz and 13.80 Hz and the mid-gap frequency is 11.45 Hz, which is very close to the above assumed result.
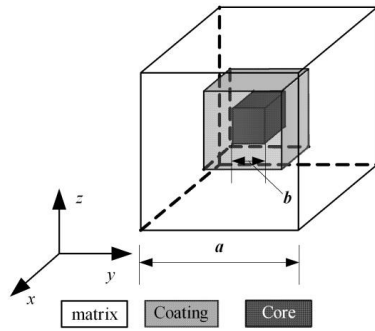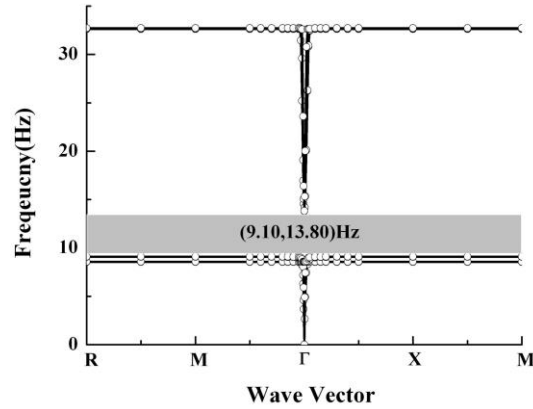

Fig. A.1 One unit cell of 2D periodic foundation[1]

Fig. A.2 Dispersion relationship of a coated cube inclusion periodic structure with a=1.0m b=0.6m, and t=0.1m[1]

A.3 Back-up Information

The band gaps of the periodic material are determined by the material and geometric properties, and the starting frequency of the first band gap are affected by the size of the unit cells. Therefore, the unit cell size of 2D and 3D periodic foundations can

be estimated from the mid-gap frequency, according to the theoretical solution and test results. The relationship of the wave length of input wave and the size of unit cell can be found as follows:

For 2D periodic foundations, concrete reinforcement is provided as matrix material. Fig. A.3 shows one unit cell of a 2D periodic foundation. To find out the wave length of the input wave that can be isolated by the periodic foundation, the wave velocity is calculated first.
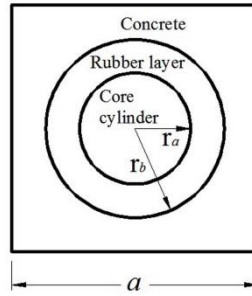

Fig. A.3 One unit cell of 2D periodic foundation

The wave velocity of P wave[2] in concrete is

$$c_p = \sqrt{\frac{\lambda_c + 2\mu_c}{\rho_c}} = \sqrt{\frac{(2.2944 + 2 \times 1.182) \times 10^{10}}{2300}} = 4500(m/s) \tag{A-3}$$

Where, c_p is the P wave velocity in concrete. λ_c and μ_c are Lame constants of concrete, ρ_c is the density of concrete. For concrete, $\lambda_c = 2.922 \times 10^{10}$ N/m^2, $\mu_c = 1.182 \times 10^{10}$ N/m^2, and $\rho_c = 2300$ kg/m^3.

With the case shown in Section 3.2 of this report as an example, the band gap is 41.2 Hz-58.7 Hz, and the mid-gap frequency is 49.95 Hz, as shown in Fig. A.4. The wave length of P waves that can be isolated by the above-mentioned periodic foundation can be obtained, as shown in Eq. (A-4).

$$\text{wave length} = \frac{\text{wave velocity}}{\text{frequency}} = \frac{c_p}{\text{midgap frequency}} = \frac{4500}{49.95} = 90\text{m} \tag{A-4}$$

Comparing the above-obtained wave length to the size of the unit cells, the wave length is 354 times of the unit cell size, as shown in Eq. (A-5).

$$\text{ratio} = \frac{\text{wave length}}{\text{size of unit cell}} = \frac{90\text{m}}{0.254\text{m}} = 354.33 \qquad \text{(A-5)}$$
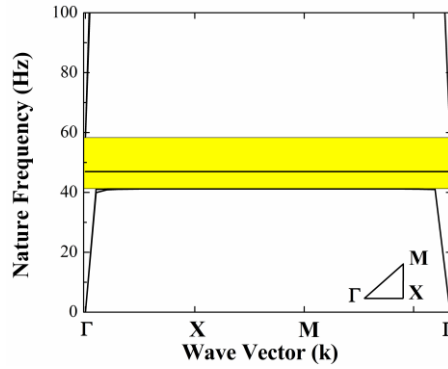

Fig. A.4 Theoretical solution of the first band gap of 2D periodic foundation

The ratio of the wave length to the size of unit cell is 354 for the periodic foundation considered in this case. In the 3D phononic crystal research, Liu et al.,[3] reported that low frequency band gap can be obtained when the wave length of the P wave is 300 times greater than the lattice constant of the crystal in the periodic foundation. In this project, the case with a wave length to unit cell size ratio of 354 is slightly greater than 300 reported in Liu et al.[3]

A.4   References

[1] Cheng, Z., Yan Y., Menq, F., Mo, Y.L., Xiang. H, Shi, Z. & Stokoe, II, K. (2013). 3D Periodic Foundation-based Structural Vibration Isolation. World Congress On Engineering, International Conference Of Mechanical Engineering, London, UK, July 3-5.

[2] Wang, G., Yu, D., Wen, J., Liu, Y., & Wen, X. (2004). One-dimensional phononic crystals with locally resonant structures. *Physics Letters A*, 327(5), 512-521.

[3] Liu, Z., Zhang, X., Mao, Y., Zhu, Y. Y., Yang, Z., Chan, C. T., & Sheng, P. (2000). Locally resonant sonic materials. *Science*, *289*(5485), 1734-1736.